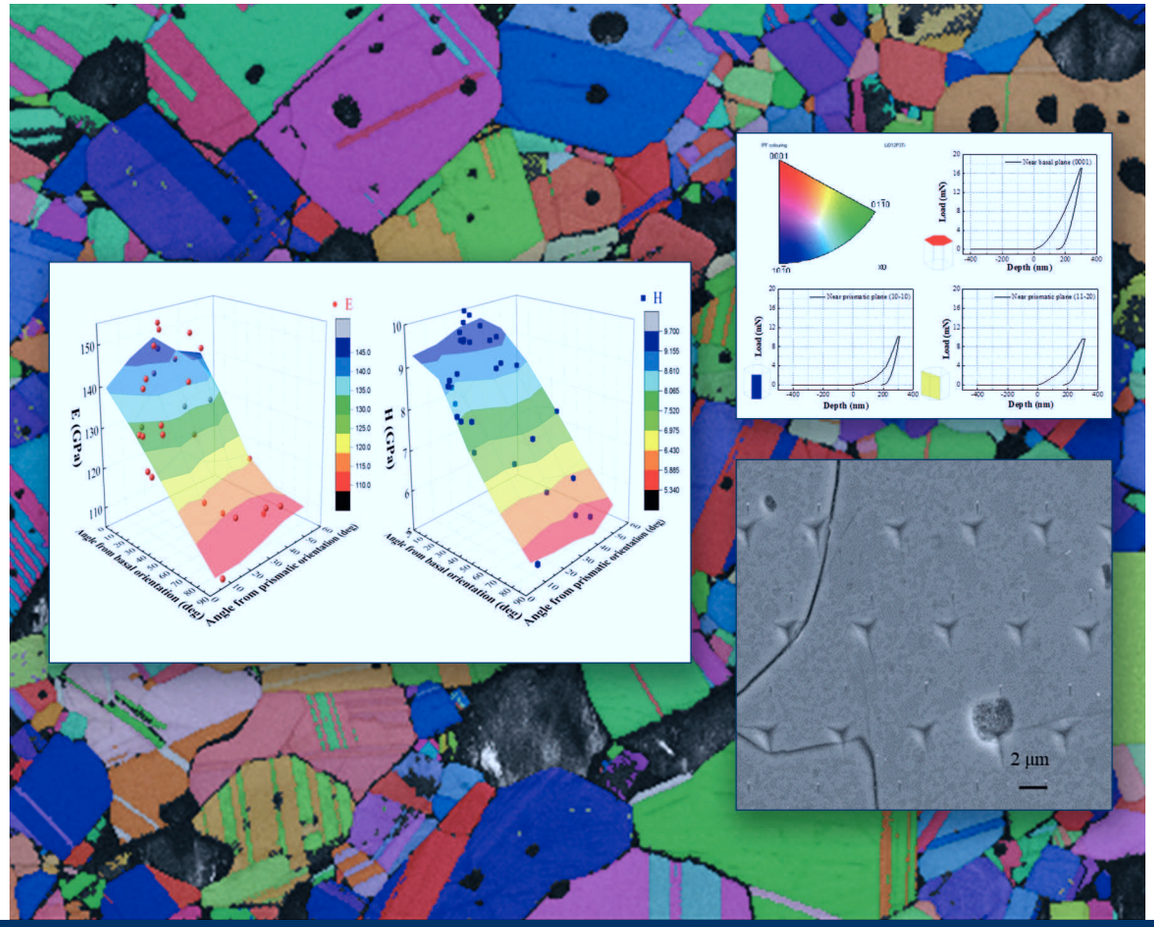

Mechanical Behavior of Solid Electrolyte Materials for Lithium-ion Batteries

Gang Yan

Energie & Umwelt / Energy & Environment
Band / Volume 500
ISBN 978-3-95806-484-3

Mitglied der Helmholtz-Gemeinschaft

JÜLICH
Forschungszentrum

Schriften des Forschungszentrums Jülich
Reihe Energie & Umwelt / Energy & Environment Band / Volume 500

Forschungszentrum Jülich GmbH
Institut für Energie- und Klimaforschung
Werkstoffstruktur und -eigenschaften (IEK-2)

Mechanical Behavior of Solid Electrolyte Materials for Lithium-ion Batteries

Gang Yan

Schriften des Forschungszentrums Jülich
Reihe Energie & Umwelt / Energy & Environment Band / Volume 500

ISSN 1866-1793 ISBN 978-3-95806-484-3

Bibliografische Information der Deutschen Nationalbibliothek.
Die Deutsche Nationalbibliothek verzeichnet diese Publikation in der Deutschen Nationalbibliografie; detaillierte Bibliografische Daten sind im Internet über http://dnb.d-nb.de abrufbar.

Herausgeber und Vertrieb:	Forschungszentrum Jülich GmbH Zentralbibliothek, Verlag 52425 Jülich Tel.: +49 2461 61-5368 Fax: +49 2461 61-6103 zb-publikation@fz-juelich.de www.fz-juelich.de/zb
Umschlaggestaltung:	Grafische Medien, Forschungszentrum Jülich GmbH
Druck:	Grafische Medien, Forschungszentrum Jülich GmbH
Copyright:	Forschungszentrum Jülich 2020

Schriften des Forschungszentrums Jülich
Reihe Energie & Umwelt / Energy & Environment, Band / Volume 500

D 82 (Diss. RWTH Aachen University, 2020)

ISSN 1866-1793
ISBN 978-3-95806-484-3

Vollständig frei verfügbar über das Publikationsportal des Forschungszentrums Jülich (JuSER) unter www.fz-juelich.de/zb/openaccess.

This is an Open Access publication distributed under the terms of the Creative Commons Attribution License 4.0, which permits unrestricted use, distribution, and reproduction in any medium, provided the original work is properly cited.

Contents

List of Figures

List of Tables

List of Symbols and Abbreviations

Symbols

ϑ	Poisson's ratio	-
σ	uniform internal stresses	MPa
ε	strain	-
γ	geometric factor of the crack shape on surface (theoretically 1.12)	-
α	defect size	m
m	Weibull modulus	-
E	elastic modulus of the material	GPa
$\varphi 2$	specific angle to x axis in the basal plane	°
Φ	angle from basal plane to the perpendicular direction	°
λ	X-ray wave length	nm
θ	reflection angle	°
α, β, γ	angles of lattice parameters	°
n	subcritical crack growth exponent	-
l	length of cracks at the corner of Vickers indentation	m
H	hardness	GPa
E_r	reduced elastic modulus	GPa
d	distance between the neighbored atomic layers	nm
D	subcritical crack growth constant	-
C_{ijkm}	elastic constants	GPa
c	$c = a + l$	m
A_r	residual indentation area after the indentation	m^2
a^*, b^*, c^*	lengths of lattice parameters	nm
A	contact area	m^2
a	half of the diagonal of Vickers indentation	m
σ_i	characteristic strength for a time t_i (i = 1, 2)	MPa
σ_0	characteristic fracture strength of a ceramic material	MPa
t_l, t_u	constants relating to the given confidence interval	-
l_l, l_u	constants relating to the given confidence interval	-

P_f	failure probability based on Weibull statistics	-
K_{IC}	fracture toughness	MPa·m$^{1/2}$
G_c	critical energy	J
E_{ROR}	elastic modulus of the material obtained from ROR test	GPa
D_l, D_u	the lower and upper bounds	-
C_l, C_u	the lower and upper bounds	-
σ_f	fracture stress	MPa
(*hkl*)[*uvw*]	miller notion represents grain orientation	-

Abbreviations

LIBs	Lithium Ionic Batteries
ASSLIBs	All Solid-State Lithium-Ion Batteries
NASICON	Sodium (Na) Super Ionic Conductor
LATP	$Li_{1+x}Al_xTi_{2-x}(PO_4)_3$
LLZO	$Li_7La_3Zr_2O_{12}$
LLTO	$Li_{3x}La_{2/3-x}TiO_3$ / $Li_{0.350}La_{0.557}TiO_3$
LATP:Si	$Li_{1.5}Al_{0.5}Ti_{1.5}(PO_4)_3$ mixed with SiO_2
Th. Sp. Capacity	Theoretical Specific Capacity
Th. Sp. En.	Theoretical Specific Energies
Pr. Sp. En.	approximate Practical Specific Energies
OCV	Open Circuit Voltage
SSE	Solid State Electrolyte
LiPON	Lithium Phosphorus Oxinitride
SOC	State Of Charge
VIF	Vickers Indentation Fracture method
SCG	Subcritical Crack Growth
SPT	Stress Probability Time
EIS	Electrochemical Impedance Spectroscopy
ROR	Ring-on-ring bending test
B3B	Ball-on-3-ball bending test

1. Introduction

The substantial utilization of energy being still strongly based on fossil fuels caused increasing concerns associated with global warming, climate change, environmental pollution and future energy shortage p. In order to reduce the dependency on fossil fuels, which would be beneficial for the environment, especially in terms of the reduction of CO_2 emission, a variety of technologies are being developed applying sustainable energy sources [1]. Rechargeable batteries, which can reciprocally transfer energy from external electricity with an internal chemical storage and vice versa, are deemed to be a promising energy buffer due to the technological and economic feasibility [2]. Furthermore, as the demands for batteries in terms of capacity, portability and size miniaturization increase, lithium ionic batteries (LIBs) are getting more and more attention [3].

In LIBs, electrolytes are required to separate the electrodes from short-circuit and permit the ionic transportation. Conventional electrolytes that are used currently in commercial batteries are based on liquid electrolytes consisting of organic solvents, which endure leakage, flammability and potential explosion [4]. All solid-state lithium-ion batteries (ASSLIBs) being based on solid state electrolytes are regarded at present as an alternative to conventional batteries on account of their higher ionic conductivity, energy density as well as higher chemical stability and safety [5]. The potential solid electrolyte classes can be divided into polymers, glass-ceramics, glassy amorphous electrolytes and inorganic solid electrolytes [6]. Among the inorganic solid electrolytes, promising ionic conductive ceramic materials have been developed, e.g., sodium (Na) super ionic conductor (NASICON) materials, perovskite materials and garnet type materials [7].

The commendable electro-chemical performances of solid electrolytes could satisfy the requirements for commercial application, for power source applications ranging from micro-device to spaceships, as has been investigated in a number of studies [8], nevertheless mechanical properties of electrolytes, which are important to warrant the long-term reliability, need to be studied deeper.

1. Introduction

Considering battery applications in micro-devices, where the electrolyte thickness should be thinner than 20 μm, the preferred orientations of the electrolyte ought to be found out and selected to achieve optimized separation and support for the electrodes [9]. Besides, mechanical properties of the electrolytes might change as a result of charging and discharging cycling related to the chemical expansion [10]. In addition, to warrant a long-term reliability of the battery component the assessment of fracture strength and failure probability of the electrolyte is necessary and can be used as criteria for the further design and improvement of the ASSLIBs [11].

Thus, the overall aim of this work is to study the mechanical characteristics of ceramic materials that are considered as candidates for application as solid electrolytes and the relationship of properties to materials' microstructures. For this purpose three types of solid electrolytes, NASICON type $Li_{1+x}Al_xTi_{2-x}(PO_4)_3$ (LATP), garnet type $Li_7La_3Zr_2O_{12}$ (LLZO), perovskite type $Li_{0.350}La_{0.557}TiO_3$ (LLTO), were chosen due to the promising electro-chemical properties. To widen the understanding of the mechanical properties of newly-developed LATP materials compared to LLZO and LLTO materials, the hot-pressed LATP materials sintered at various temperatures in the range of 950 °C to 1100 °C were selected to investigate sintering temperature effects on the mechanical properties. Meanwhile the LATP sintered at 1100 °C, which revealed higher elastic modulus and hardness than the other LATP samples, was selected to study the grain orientation effect related to the rhombohedral crystal structure. Since the fracture strength of pure LATP has been reported by Jackman et al. [12], the tape casting $Li_{1.5}Al_{0.5}Ti_{1.5}(PO_4)_3$ mixed with SiO_2 (LATP:Si) was selected here to investigate the fracture reliability and to assess if the mechanical properties can be improved with the addition of SiO_2 binder during the processing. In addition, the fracture reliability of the alternative material LLZO was studied in this work to permit comparison; elastic modulus, hardness and fracture toughness were not studied here since they have been reported elsewhere [13, 14]. As the electrolytes in all-solid-state lithium batteries are operating under cyclic voltage condition that are associated with chemical expansion effects, exemplified for LLTO, a material being close to application [15-17], voltage effects on mechanical properties were studied. The relation between the mechanical properties and the microstructure of the materials i.e. phase information, grain size, porosity etc. is always discussed.

Overall, the investigation of the sintering temperature effect, charge state effect and grain orientation effect on the mechanical properties of the electrolytes as well as the fracture reliability aid an understanding of the mechanical behavior of the materials and provide a data base for further improvement of design and processing of battery materials and cells.

2. Literature Review

As outlined above, all solid state lithium batteries are a promising alternative for conventional lithium batteries with liquid electrolyte. Apart from the superior electro-chemical properties of the solid electrolyte applied in the ASSLIB, for instance, the favorable ionic conductivity, chemical stability, thermal compatibility, satisfactory mechanical behavior are also highly required and can potentially be met by the ASSLIB materials. This section introduces the basic knowledge on lithium batteries and solid electrolytes as well as the mechanical aspects that are potentially relevant for reliability and failure of such batteries.

2.1 Batteries

Since global societies have developed a crucial dependency on electricity, the evolution of the systems for conserving energy becomes pivotal in the 21st century [18]. As a device transforming and storing the energy generated via the spontaneous chemistry reaction to electrical work, batteries have outstanding properties in this respect: charging and discharging electrical energy, portability and flexibility for short lead period in fabrication [19]. With the separation of electrolytes in between the electrodes, the current carrier from one electrode to the other is realized, while an external intact circuit path is applied to the battery cell [20]. Inside the battery cell, the circuit is closed by the ion transport through the electrolyte. To assess the battery systems' performance several parameters like energy density, power density and energy efficiency are of main concern [21].

The basic electrochemical cell concept is attributed to an experiment by Alessandro Volta that, when separating two unlike metals (copper and zinc) with acidic electrolyte, electricity can be produced [22]. The first primary alkaline battery of zinc-carbon cell was invented by Alessandro Volta in 1800 [23]. Thereafter the rechargeable battery cells using aqueous electrolytes of lead-acid was developed by Gaston Plante in 1859 [24]. Subsequently, the nickel-cadmium cell was proposed by Waldemar Jungner in 1899 and the nickel-iron cell was proposed by Thomas Edison in 1901 [25, 26]. These battery systems based on nickel were predecessors of the nickel-metal hybrid batteries introduced in market in 1989, which is currently still used in Toyota's hybrid-electric vehicles [27].

Due to the oil crisis in mid 1970s, the non-aqueous sodium batteries were prompted, that researchers at Ford Company discovered, revealing that with the usage of solid electrolytes (beta-Al_2O_3) at high temperature high sodium ion conductivity can be achieved [28]. Afterwards, the sodium-based battery systems based on Na-S and Na-MCl_2, operating at 300 – 350 °C, were commercialized [29, 30], as illustrated in Table 2.1.

In Table 2.1 the theoretical (Th.) and approximate practical (Pr.) specific (Sp.) energies of rechargeable batteries are listed, where theoretical values based on masses of active electrode-electrolyte materials only, practical values based on mass of battery cell, and specific capacity of energy based on the values normalized to 1 kg [31]. The open circuit voltage (OCV) means the electrical potential difference between two terminals of a device when disconnected from circuit and the theoretical (Th.) specific (Sp.) capacity means the level of a production that would be attained if all of its equipment and operations performed continuously at their optimum efficiency. For OCV and Th. Sp. capacity indexes the higher value the better for portable electronic application [8]. Although the sodium-based batteries can offer theoretical energy densities of more than 700 Wh/kg, these batteries possess notable problems due to the necessity of additional rigs for heating and cooling the system to control operating and standby temperatures. Thus, the commercially realized working energy density of sodium-based batteries is only 90 - 120 Wh/kg [21]. Besides, safety concerns of sodium-based batteries can’t be ignored, i.e. that, if the membrane of β-Al_2O_3 ruptures, for the Na-S cell, the molten sodium can violently react with the molten sulfur and for the Na-MCl_2 battery, the electrolyte $NaAlCl_4$ can be decomposed to Al metal and NaCl, which both lead to possible sodium burning. Therefore, Na-S and Na-$NiCl_2$ batteries are now primarily used for back-up power storage such as in submarine applications [31].

Following the design of sodium-based battery, high temperature (80-120 °C), rechargeable lithium batteries with polymer electrolyte were projected, see Table 2.1 [32]. The lithium ion battery (Li-ion battery) was termed after the lithium-ions transfer between the electrodes through the electrolyte. However, due to the burning effects that arose from the lithium dendrites that

were growing through the electrolyte, yielding short circuit and continuous heating, the Li-polymer battery dropped out the market [32].

In 1991, Sony Company introduced the high voltage and energy Li_xC_6 - $Li_{1-x}CoO_2$ cell with non-aqueous liquid electrolyte for portable devices, which brought a key improvement of the lithium ion battery technology, as illustrated in Table 2.1 [33]. Here, the lithium coupled with a graphite host was used as anode instead of lithium metal to protect the battery cell from dendrite formation. Other than regarding the anode, of which graphite remained the main candidate material, cathode materials with different composition and structure were developed and even commercialized, for instance, spinel $LiMn_2O_4$, olivine $Li_{1-x}FePO_4$ and the layered $LiCoO_2$ with substitution of Mn and Ni for Co (Table 2.1) [34-36]. During practical application, mixtures of the cathode materials are often adopted to enhance the cell properties and reduce the cost [31].

Table 2.1 The theoretical (Th.) and approximate practical (Pr.) specific (Sp.) energies of rechargeable batteries (theoretical values based on masses of active electrode-electrolyte materials only; practical values based on mass of battery cell) [31].

System	Anode (negative electrode)	Cathode (positive electrode)	Open circuit voltage (V)	Th. Sp. Capacity (Ah kg^{-1})	Th. Sp. En. (Wh kg^{-1})	Pr. Sp. En. (Wh kg^{-1})
Lead-acid [24]	Pd	PdO_2	2.1	83	171	20-40
Ni-Cd [25]	Cd	NiOOH	1.35	162	219	20-40
Ni-MH [26]	MH alloy	NiOOH	1.35	~178	~240	50-70
Na-S (350 °C) [29]	Na	S	2.1-1.78	377	754	~120
Na-MCl_2 (300 °C) [30]	Na	$NiCl_2$	2.58	305	787	~90
Li-polymer (80-120 °C) [32]	Li	LiV_3O_8	3.3-2.0	~340	~884	~150 (weeded out due to fires)
Li-ion [33]	Li_xC_6	$Li_{1-x}CoO_2$	4.2-3.0	158 (x=1.0)	584	100-150

Li-ion [34]	Li_xC_6	$Li_{1-x}Mn_2O_4$	4.2-3.0	104 (x=1.0)	424	80-100
Li-ion [35]	Li_xC_6	$Li_{1-x}FePO_4$	3.4	117 (x=1.0)	398	80-100
Li-ion [36]	Li_xC_6	$Li_{1-x}MO_2$	4.6-3.0	160 (x=1.0)	592	-

However, based on observations made for existing lithium ion batteries, apart from concerns regarding higher energy densities, more attention is directed towards application relevant aspects like capacity loss due to continuous charging and discharging, utilization of devices in grids, and especially concerns regarding liquid electrolyte [37]. The main drawback in conventional Li-ion batteries is the usage of the flammable, toxic liquid electrolyte, which suffers from leakage if the battery cell structure is damaged, and makes the conventional Li-ion battery prone to explode as a result of strong exothermic reactions especially in cases that the liquid electrolyte is unable to prevent the formation of the lithium dendrites during charging/discharging [38, 39].

For the sake of surmounting such problems, recently all-solid-state lithium ion batteries (ASSLIBs) with a solid electrolyte positioned in between the electrodes are being comprehensively investigated [40]. Such Li-ion batteries with solid electrolyte are superior in terms of reduction of weight and volume of the cell and higher energy output, which enables a higher working efficiency [41]. In addition, compared with other common power carriers, the solid state Li-ion batteries also possess advantages regarding lower self-discharge and wear and also a more stable output voltage [42]. The working principle of conventional Li-ion batteries and all solid state Li-ion batteries is basically the same, whereas the realization in a construction can be much different, as illustrated in Figure 2.1 [43].

Compared with the conventional battery possessing a liquid electrolyte, the battery using a solid electrolyte can be implemented into a more compact bipolar structure. Taking the lowest density of solid element lithium metal into consideration, a high theoretical capacity of around 1000 Wh/kg might be achieved [44]. Nevertheless, the solid state batteries, especially the solid electrolyte, also faces challenges such as the apparently high ionic resistance at operation relevant environmental temperature, fabricating cost, and warranting and understanding of mechanical properties for battery design and development [45].

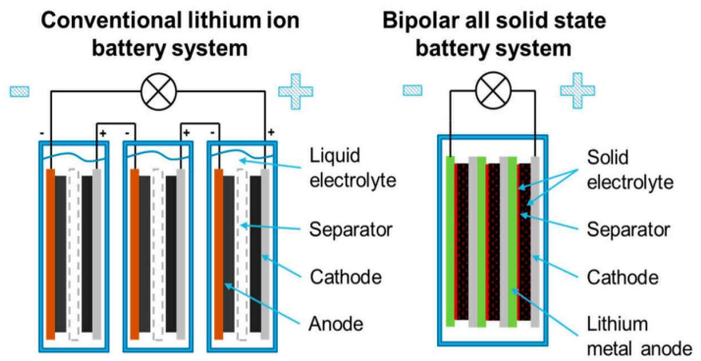

Figure 2.1 Illustration of (a) conventional Li-ion batteries in stack and (b) bipolar all-solid-state Li-ion batteries in stack [43].

Furthermore, since the quantity requirements for portable devices increase rapidly, investigations on the small batteries applied in the micro-electronics like medical devices (hearing aid, in vivo imaging), highly integrated circuits (actuators, sensors), are also growing fast in recent years [46]. Comparing with the size of conventional commercial Li-ion batteries, for instance, the 18650 cylindrical battery cells is in 18.6 mm diameter and 65.2 mm length [47], the planar type micro batteries possess a total unit cell thickness of < 20 μm [9](where the thickness of the electrolyte can be a few microns, as illustrated in Fig. 2.2), which requires both the electrodes and electrolyte materials to perform favorable and reliable regarding electro-chemical properties and mechanical properties in such small size range [9].

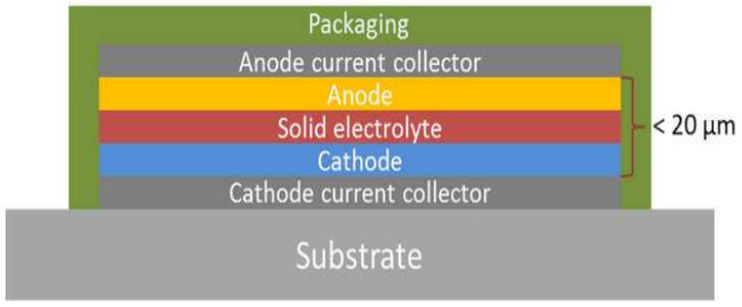

Figure 2.2 Schematic of a planar thin-film micro-battery architecture [9].

2.2 Solid electrolytes

All solid state lithium ion batteries are composed of anode, cathode and the solid state electrolyte (SSE). The solid state electrolyte is not only conducting the lithium ions, it also serves as a separator in equivalence of a liquid electrolyte. It permits a simpler battery cell structure, lowers the risk regarding safety concerns like poisonous leakage, flammability, and potentially achieves higher energy density and lifetime [48]. In this subsection, the state of solid electrolyte materials is reviewed summarizing relevant properties.

2.2.1 State of solid electrolytes for batteries application

For being usable as electrolyte the material should have a sufficient amount of portable ions to ensure an adequate conductivity and low activation energy, and possess a low internal short-circuit probability [49]. At present, solid electrolytes are mainly categorized into two types: organic polymer solid electrolyte materials and inorganic ceramic materials [50]. A typical difference between organic and inorganic electrolyte materials is their mechanical behavior, which results in the different designs of these two materials classes.

2.2.1.1 Organic electrolytes

Organic polymer electrolytes possess advantages regarding easiness to be processed, which leads to lower fabrication costs, and in addition flexibility, safety and ability of preventing the formation of lithium dendrites [51, 52]. In general, mainly two kinds of polymer electrolytes have been developed: one with lithium salts solved in the polymer chain and the other is that forming a polymer gel with additives of solvent [51]. The difference is that the solid polymer electrolytes have better mechanical properties, hence they can be used for free-standing films, whereas polymer gels have overall lower mechanical performances but higher ionic conductivities [50].

The polymer gel electrolyte is formed by introducing a liquid electrolyte into the polymer matrix [53]. The working principle of the polymer gels is quite similar to that of the liquid electrolytes, however, the polymer gels are safer and shape-flexible [51]. The most commonly

used polymer gel electrolyte is the poly-vinylidene fluoride (PVdF) mixed with hexafluoropropylene (HPF). The ionic conductivity of PVdF-HFP has been reported in a number of studies [54-56], and the conductivity can reach up to 4 S/cm [57].

Two methods can be applied to improve the conductivity of the gel electrolytes. One is to increase the amount of pores in the structure to enhance the movement of lithium ions, which can be realized by adding particles or modify the structure [56, 58]. The other is the use of room temperature ionic liquids (RTIL), which is a safer alternative compared to conventional organic solvent-based electrolytes [37, 59]. Another commonly used gel electrolyte is poly-methyl methacrylate (PMMA), which, however, has a lower conductivity, especially at room temperature [60, 61].

The solid polymers possess a higher elastic modulus and hardness than the gel electrolytes, of which the poly-ethylene oxide (PEO) is most commonly one used currently [53]. The PEO material is good at solvating lithium salts to yield improved ion conduction [62, 63]. The ionic conductivity property of PEO material mixed with different lithium salts are in a similar range (10^{-3} - 10^{-6} S/cm at room temperature) [50]. For the sake of decreasing the activation energy for ion-conduction in PEO materials the temperature can be increased, which is related to the glass transition point [64]. In addition to PEO materials, substitutional materials are also developed such as poly-ethylene oxide-methyl ether methacrylate (PEOMA), poly-ethylene glycol methacrylate (PME) or tri-ethylene glycol diacrylate (TEGDA), which possess conductivity properties close to or even higher than PEO [65-67]. Overall, both the gel electrolytes and solid polymer electrolytes can be used in combination with other salts or other electrolytes to improve conductivities [68-71].

2.2.1.2 Inorganic electrolytes

Regarding inorganic ceramic materials, the ionic conductivity induced by point defects requires energy for their creation and motion, which implies that via the use of higher temperatures the conductivity can be increased [72]. In this respect, ceramic electrolyte candidates have advantages for use in such higher temperature applications rather than organic polymer electrolytes. Some compounds that possess high ionic conductivity at rather low

temperature have been studied for applying in the Li-ion batteries [73-76]. In contrast to the polymer materials, ceramic electrolytes completely without any organic solvent possessing higher elastic modulus and hardness are likely to be considered as the candidate materials for micro-batteries [5, 77].

The inorganic ceramic materials can be sorted into two types: crystalline ion conductors and amorphous glass ion conductors [78]. The difference is that different manufacturing processes are applied to produce the non-crystallized sample, like twin roller, high-energy mechanic-chemical milling, and vapor deposition or even explosive glass forming craft [79], whereas for the crystalline materials hot pressing, injunction molding, dry pressing, tape casting, isostatic pressing methods are used [80].

The lithium phosphorus oxinitride (LiPON) material is also considered as solid electrolyte candidate. LiPON with the composition $Li_{2.88}PO_{3.73}N_{0.14}$ was reported to have a high ion conductivity of 3.3×10^{-6} S/cm at room temperature [81]. The sulfide compounds have been used as electrolytes in crystalline, amorphous and mixed forms [50]. As a typical sulfide electrolyte Li_2S-P_2S_5 has been widely investigated as a glass or glass-ceramic compound of which the conductivities varies from 10^{-5} to 10^{-2} S/cm depending on the P_2S_5 content [82, 83]. The conductivity of Li_2S-P_2S_5 in glass-ceramic form is higher than that in glass form, which manifests that the crystalline phase possess better electrochemical property than the amorphous phase [72]. Nevertheless, the crystallization can somehow decrease the total conductivity in some cases like Li_2S–P_2S_5–Li_4SiO_4 [84]. Other sulfide glasses are also developed like Li-Si-P-S, Li-Ga-Ge-S, of which the conductivity is similar to Li_2S-P_2S_5 and can be improved by adding Li_4SiO_4 [41, 50]. In addition, new sulfide crystals, lithium superionic conductors (LISICON) found in the Li-Ge-P-S system, have also been investigated like $Li_{3.25}Ge_{0.25}P_{0.75}S_4$, $Li_{4.2}Ge_{0.8}Ga_{0.2}S_4$ and $Li_{2.2}Zn_{0.1}Zr_{1.9}S_3$ [85-87].

The phosphate compounds $AM_2(PO_4)_3$ (A = Li, Na, K; M = Ge, Ti, Zr) were investigated already in the early 1960s and this structure is named NASICON (sodium (Na) super (S) ionic (I) conductor (CON)); they have a high sodium ion conductivity as firstly indicated by Goodenough et al. [88]. NASICON structures possess a rhombohedral space group, which can also be

computed into a hexagonal space group [75]. For lithium ion conduction the Li ions occupies the A sites and the lithium conductivity of the NASICON materials was related to the channel size and diffusing ions [73].

$LiTi_2(PO_4)_3$ is reported to have a high ion conductivity and with the substitution of M^{3+} (M= Al, Ga, Cr, Fe, In, Y, La) for Ti^{4+} the conductivity can be improved by more than one order of magnitude [89]. Particularly, NASICON with Al substitution, $Li_{1.3}Ti_{1.7}Al_{0.3}(PO_4)_3$, was obtained with the highest conductivity of 7×10^{-4} S/cm at room temperature [89]. In addition, Xu et al. synthesized $Li_{1.4}Ti_{1.6}Al_{0.4}(PO_4)_3$ via a spark plasma method in nano-grained structure with almost 100% density achieving 1.12×10^{-3} S/cm [90].

Among the NASICON structure material the $Li_{1+x}Al_xGe_{2-x}(PO_4)_3$ (LAGP) has also been studied due to its good electrochemical stability, high conductivity and wide operation window [91]. It is reported that a glass-ceramic $Li_{1.5}Al_{0.5}Ge_{1.5}(PO_4)_3$ was sintered in order to promote a conductivity of which 6.2×10^{-4} S/cm [91]. Thus, the NASICON type conductors possess necessary properties to serve as electrolyte in the all solid state lithium ion batteries.

The novel garnet family electrolytes were first discovered by Kasper [92], with the general structure of $A_3B_2C_3O_{12}$ (A = Ca, Mg, La or rare earth; B = Fe, Al, Ga, Ge, Mn, Ni or V; C = Si, Ge, Al). In the lithium garnets the Li shares the corners in the tetragonal structure and octahedral structure, leading to a unit cell containing 5 to 7 Li atoms [92]. These kinds of electrolytes are found to possess a high decomposition voltage (6 V vs. Li) and an ionic conductivity similar as pure lithium, which makes them promising for the usage in the all-solid-state lithium battery. The $Li_5La_3M_2O_{12}$ (M = Nb, Ta) electrolyte yields a conductivity of 10^{-6} S/cm at room temperature and the conductivity can be improved by substituting the La site with Ca, Sr or Ba ions [93]. Another garnet electrolyte is $Li_6ALa_2M_2O_{12}$ (A = Ca, Sr, Ba), which can achieve an ionic conductivity of 4×10^{-5} S/cm [94].

Currently works appears to concentrate more on the $Li_7La_3C_2O_{12}$ (C = Zr, Sn) material [93, 95]. The $Li_7La_3Zr_2O_{12}$ in cubic structure was also investigated, which possesses the highest conductivity of 1.8×10^{-4} S/cm [95]. However, the tetragonal structured $Li_7La_3Zr_2O_{12}$ has a lower

conductivity and higher activation energy [96]. The difference between the tetragonal and cubic structure is that the lithium vacancies are completely ordered in tetrahedral sites, however, the tetrahedral structure transforms into a cubic structure between 100 to 150 °C [14]. In order to stabilize the cubic phase of $Li_7La_3Zr_2O_{12}$ and to enhance the conductivity further Al doping and other metal substitutions for example Zr might be used [97, 98].

Perovskite type ceramic materials, with general structure of ABO_3 (A is alkaline metal ion and B the transition metal ion), are also developed for solid electrolyte application [99]. A perovskite ABO_3 material ideally possesses a cubic symmetry. Due to the composition and sintering process, a tetragonal or orthogonal structure can also be obtained [100]. Regarding perovskite type electrolytes a series of $Li_{3x}La_{2/3-x}TiO_3$ was evaluated, where Li and La take the A sites [99]. The conductivity of this material can exceed 10^{-3} S/cm at room temperature, which attracted strong scientific interests [101]. The occupation of La at A site generates more vacancies, where the lithium ion transport can be improved by a vacancy mechanism [100]. Nevertheless, since the lithium can intercalate into the $Li_{3x}La_{2/3-x}TiO_3$ lattice, leading to a Ti^{3+} transformation, the $Li_{3x}La_{2/3-x}TiO_3$ is not suitable for use as solid electrolyte if in direct contact with lithium [102].

The research field on solid electrolytes is developing gradually and the current attainments manifest that the ASSLIBs are promising for energy storage and future portable devices applications [31]. Further development is still necessary to improve their energy density, electro-chemical stability and production process, while warranting their primary safety. Although laboratory reports on ASSLIBs, especially of the solid electrolytes, exist in a rather large quantity [50], they are still not close to commercial industrial applications, which requires further systematic investigations on various aspects of the materials including mechanical behavior.

2.2.2 $Li_{1.3}Al_{0.3}Ti_{1.7}(PO_4)_3$, $Li_7La_3Zr_2O_{12}$ and $Li_{0.350}La_{0.557}TiO_3$ solid electrolytes

A brief summary of typical advanced inorganic solid electrolytes is listed in Table 2.2. It can be seen that the garnet, NASICON and perovskite type materials have quite comparable ionic conductivities. For the commercial application not only the ionic conductivity of these materials

needs to be improved, but also the mechanical characteristic deserves deep exploration to warrant long-term safety in operation.

Table 2.2 Brief summary of typical inorganic solid electrolytes.

Short name	Type	Representative composition	Ionic conductivity (RT, S/cm)	Reference
LiPON	Amorphous	$Li_{2.88}PO_{3.73}N_{0.14}$	3.3×10^{-6}	[81]
Sulfide glass	Amorphous	$Li_2S–P_2S_5–Li_4SiO_4$	10^{-3}	[84]
LISICON	Crystalline	$Li_{2.2}Zn_{0.1}Zr_{1.9}S_3$	10^{-6}	[85-87]
NASICON	Crystalline	$Li_{1.3}Al_{0.3}Ti_{1.7}(PO_4)_3$	1×10^{-3}	[89-91]
Garnet	Crystalline	$Li_7La_3Zr_3O_{12}$	4×10^{-5}	[14, 93, 95]
Perovskite	Crystalline	$Li_{3x}La_{2/3-x}TiO_3$	10^{-3}	[101, 102]

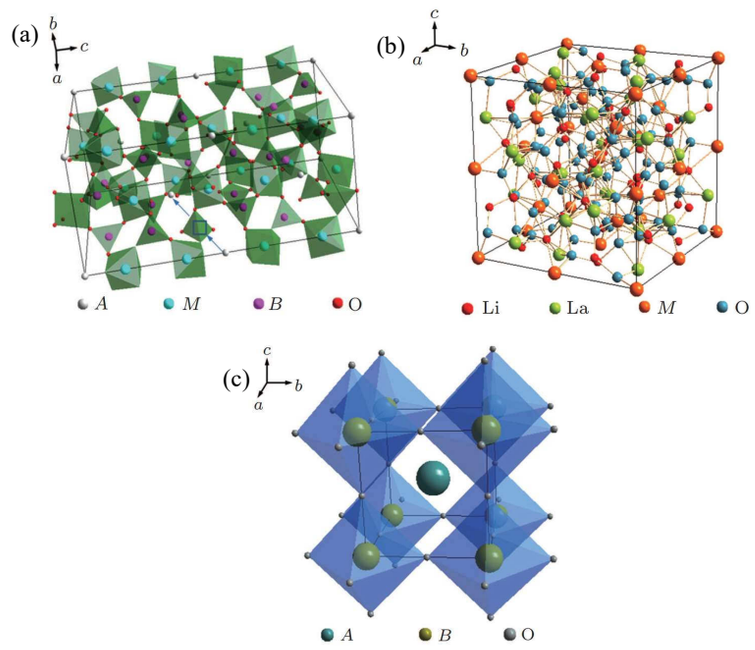

Figure 2.3 Representative atomic structure of (a) NASICON type electrolyte, (b) garnet type electrolyte, (c) perovskite type electrolyte [96].

In this work, three kinds of solid electrolytes, NASICON type material, $Li_{1.3}Al_{0.3}Ti_{1.7}(PO_4)_3$ (LATP), garnet type material $Li_7La_3Zr_2O_{12}$ (LLZO) and the perovskite type material $Li_{0.350}La_{0.557}TiO_3$ (LLTO), are selected and characterized regarding their mechanical properties, due to their stable and promising electro-chemical behavior and ionic conductivities [78]. The representative atomic structures of these three type materials are shown in Fig. 2.3.

2.2.3 Chemical expansion

During cycling in solid-state lithium batteries, the uptake and release of lithium ions in electrodes and electrolyte lead to the volume dilation of the material, which is commonly referred to chemical expansion. The ceramic battery materials with brittle nature experiencing chemical expansion can hence possess a related mechanical instability during operation. In addition, the bond length variation of the lattice related to the chemical expansion influences the electrochemical and mechanical properties [103, 104]. The chemical expansion also plays an important role in interfacial process and stability of the electrodes and electrolyte, thus the chemical expansion give information on the spatially distribution of defects inside the materials and the ion kinetics across the interfaces [105, 106].

Chemical expansion signifies the variation of the material's volume as a change of the material's composition/stoichiometry. As can be seen in Table 2.3, the chemical expansion can be divided into two types [107]. As the fraction of elements dissolved in the host lattice increases the lattice parameter possesses a gradual increase. With further augment of dissolving elements, the host lattice becomes liable for the system to form two different phases but with related crystal structures (i.e., miscibility) and hence the lattice parameter changes. During this process, one phase can be consumed and the other phase grows as dominant resulting in the volume change. Later with so much dissolving material accommodated, a second phase with unlike crystal structure is formed. The continuous change in lattice without any new phase formation is referred to as stoichiometric expansion, whereas the lattice parameter change together with additional phase formation is recognized as phase change expansion.

Table 2.3 Different types of chemical expansion (chemically induced expansion) [107].

Chemical expansion: compositionally driven dilation		
Terminology	Stoichiometric expansion	Phase change expansion
Defining characteristics	Gradual dimensional change with gradual stoichiometry change (no significant crystal structure change)	Dimensional changes associated with a change in crystal structure and/or with a large, discrete change in lattice parameter

Batteries typically display volumetric expansion upon the ion insertion, as summarized by Woodford [108] who reported on the chemical expansion values for both lithium- and sodium-based batteries materials. The chemical expansion assessed upon lithium ion inserting to $Li_xMn_2O_4$ is shown in Fig. 2.4 (a) [109]. It can be found that the volume change of $Li_xMn_2O_4$ experiences three stages. In the first stage of inserting lithium, the lattice parameter shows a small increase in line with phase change expansion of which the material maintains isostructural. At $x > 0.7$, the lattice parameter gradually increases with lithium insertion exhibiting stoichiometric expansion. For $x > 1$, again the phase change expansion appears and is counted as the change from cubic to tetragonal structure. Fig. 2.4 (b) shows the pressure-change comparison for battery cell setups involving a metal anode and zero-strain anode [110]. Due to the lithium removal of $LiCoO_2$ both anodes show an increase trend regarding pressure. Nevertheless, since the volume change of $Li_4Ti_5O_{12}$ is ignorable, the pressure variation is way smaller than using a metal anode in the battery.

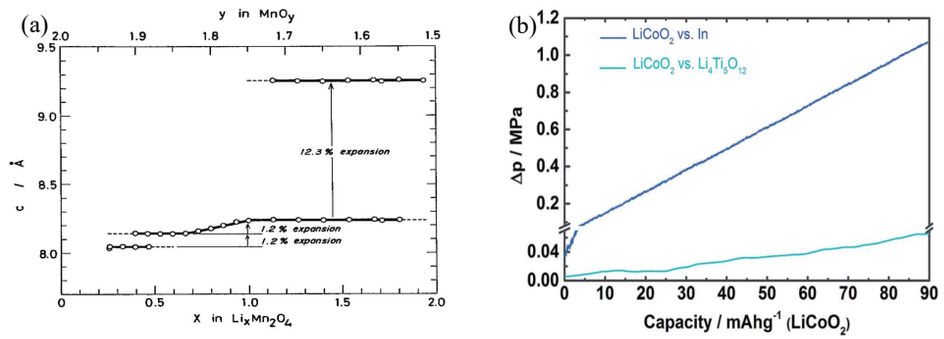

Figure 2.4 (a) Structural changes in tetragonal unit cell dimension of $Li_xMn_2O_4$ showing an initial phase change expansion, then stoichiometric expansion and ultimate phase change expansion [109]. (b) A direct comparison of the pressure-change in SSBs with an indium anode (deep blue) and a $Li_4Ti_5O_{12}$ anode (light blue) [110].

Bucci et al. [111] put forward a coupled electro-chemo-mechanical model to firstly quantified analyze the boundary condition of the battery. It is found that when the expansion of the electrode-particle is smaller than 7.5% and the fracture energy of the electrolyte is higher than 4 Jm^{-2}, the solid electrolyte fracture can be prevented. In the charge process of the model when electrolyte uptakes around 50% of total lithium capacity the compressive stress can be higher than 1 GPa. Contrary to intuition, as shown in Fig. 2.5 compliant solid electrolytes (typically elastic modulus of 15 GPa) are more liable to micro cracking [112]. State of charge (SOC) is the level of charge of an electric battery relative to its capacity, of which the units are percentage points (0% = empty; 100% = full). The chemical expansion can not only affect the material crystal structure, but also correspondingly change the mechanical properties of the material like fracture strength [112].

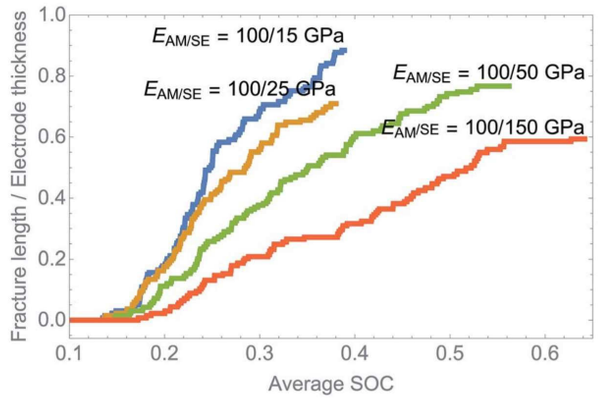

Figure 2.5 The extension of cracks plotted for solid electrolyte materials with different elastic moduli [112].

2.2.4 Dendrites issues

Although the lithium batteries have the promising properties for portable devices, the use under high energy and high power conditions can lead to the safety issues of these batteries, which currently represents a barrier for the development of all solid state lithium ion batteries and needs to be solved [113]. Among the safety issues (mechanical misusage, electrochemical misusage and thermal misusage), the formation of lithium dendrites is one of the most important and common matter resulting in the internal short-circuit of lithium ion batteries [114]. Recently, quite a number of investigations have been devoted to deeply understand lithium dendrites, formation mechanism as well as the factors influencing the dendrites formation [115, 116]. Typical lithium dendrites formed on the anode can be seen in Fig. 2.6. However, the mechanisms still need future studies.

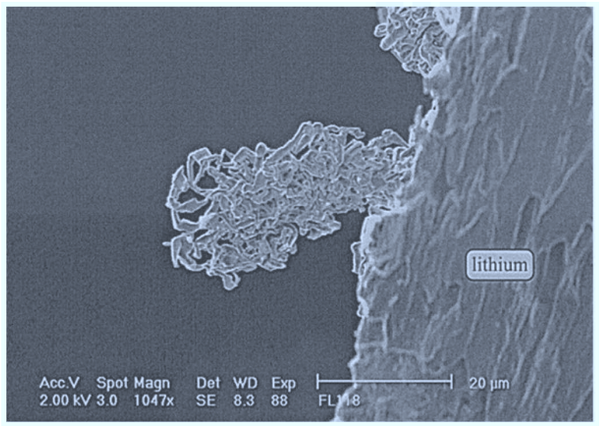

Figure 2.6 Observation of typical lithium dendrites formed on a anode surface [115].

A kinetic model based on the stress and on current density distribution at the interface was proposed to understand the growth of the lithium dendrites [117]. In this model it is proposed that to prevent the lithium penetrating into the electrolyte material the shear modulus of the electrolyte needs to be at least double of shear modulus of lithium (4.25 GPa). This indicates that the electrolyte possessing shear modulus of higher than 8.5 GPa might be used without dendrite vulnerability. However, subsequent tests with materials with adequate shear modulus to check the suppression of the dendrite propagation were not successful [114], indicating that only a higher shear modulus is not sufficient for electrolytes to resist dendrite growth.

An analytical model was proposed based on the assumption that the occurrence of lithium dendrites at the lithium-electrolyte interface is derived by the high resistance of the grain boundaries, which leads to a higher local lithium potential compared to the standard lithium potential [118]. This “excess” electro-chemical-mechanical potential can possibly be reduced by an internal stress induced by dendrites forming in the electrolytes, or by a current concentration at the convex on the lithium surface. In this first case the shift stress resisting the lithium nucleation, which is equivalent of the electrolyte fracture stress, is assumed to be 100 MPa [118].

For a ceramic electrolyte material with defects like pores or voids in the surface can be expected, since the normal traction is compressive at the interface, an equal stretching stress in

the orthogonal direction around the defects is generated, which can then lead to fracture [119]. In the other situation the growth of bulge of lithium metal is considered, that assuming the bulge size to be unity and the current density of 1 mA/cm^2, the growth of a bulge occurs if the charge resistance at interface is higher than 13.7 Ω·cm^2 [118]. It has been reported that as the critical current density is surpassed, any unevenness or inhomogeneous surface area as well as the minimum defect in the surface can influence the penetration process of the lithium dendrites, which leads to a stress and possibly results in crack propagation [120]. The lithium metal can fill in the interfacial flaws in the electrolytes and the crack mode follows the Griffith flaws as illustrated in Fig. 2.7.

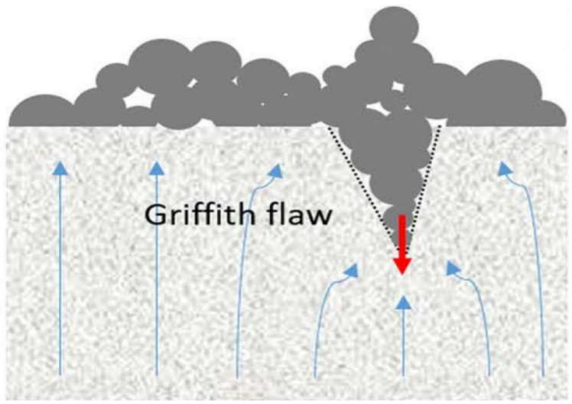

Figure 2.7 Illustration of lithium grows into the electrolyte, the red arrow indicates the dendrite growth and blue arrows represent the electric field [120].

In another model, it was proposed that in order to investigate the relation between the stress gradient and the shear stress, the plain strain is analyzed [121]. In this model the lithium metal is simplified into filaments with the constant thickness according to the experimental observation. The maximum stress on a lithium filament strongly depends on the length, which can be thermodynamically determined by the excess potential. Here the mechanical failure is relating to the electrical actuating force, which differs from the Monroe and Newman' shear modulus theory [114]. Assuming a uniform stress inside the voids, the crack extension in case of linear elastic rupture mechanism follows a Griffith-like criterion [121]:

$$\sigma \geq \frac{K_{IC}}{\gamma \cdot \sqrt{\pi \cdot \alpha}} \tag{2.1}$$

where the K_{IC} is the fracture toughness of the electrolyte material, γ the geometric factor of the crack shape on surface (theoretically 1.12), α the defect size, and σ is the uniform internal stresses equal to the maximum hydrostatic stress. With this equation the correlation between the minimum excess potential and the size of the defect in the electrolyte can be constructed. Even though this model can partially interpret the experimental observations [121], the proposed mechanism of the lithium dendrite propagation still needs to be further improved due to the uncertainty of the measurement on the defect size.

Thus, the lithium dendrites problem has been investigated in a number of studies, yet the method for preventing its growth is still uncertain. To avoid the dendrites formation the grain boundary, microstructure, relative density and the electrolyte/electrode interface need to be considered [114, 122]. Understanding the mechanical characteristics of the electrolyte materials is beneficial in exploring the dendrites issue and thereby aiding further improvement for the battery application.

2.3 Mechanical characteristics

Considering real application conditions, the solid electrolyte materials are exposed to stresses induced by different internal and external operation states, for instance, the chemical expansion, the pressure difference on the two sides contacting with electrodes, incompatibilities of thermal expansion with other components, and so on [123, 124]. For the sake of operating the battery cell securely for a long-period, the risk related to mechanical failure should be assessed. The deformation and fracture behavior of the solid electrolyte material needs to be evaluated for mechanical stability and long-term application; hence, in addition to the elastic modulus that couples strains and stresses, particular fracture reliability is critical for investigation. Within this subsection, the basic concepts and theoretical backgrounds of mechanical characteristics are introduced.

2.3.1 Elastic behavior

The elastic behavior is directly related to the atomic bonding of the material and the elastic deformation under applied stress is experimentally proportional to the stress, which can be expressed by Hooke's law [125]:

$$\sigma = E \cdot \varepsilon \tag{2.2}$$

where E is the Young's or sometimes termed elastic modulus of the material, σ the normal stress and ε the strain. In Hooke's law, the material is assumed as a homogeneous and isotropic solid, however, some materials possess a strong anisotropy [126].

In order to evaluate the elastic modulus, several methods have been implemented like indentation test, bending test, and some other non-destructive methods [127]. With the indentation test method, the elastic modulus of the material can be determined by the load-displacement curve measured during the indentation process [128]. The method is particularly advantageous to assess materials during development when only limited specimens' volumes are available for testing. The indentation with Berkovich or Vickers tips are most commonly used, whereas other tips like Knoop, Rockwell or Shore are also used less frequently [129].

Here, the elastic modulus is obtained from the slope of the unloading curve, which serves as the response of the materials' elasticity [130]. This method is widely used due to the small size requirement on the sample which can save the material as well as the time, however, the sample's preparation needs to be carefully accomplished since roughness and unevenness can influence the results [130]. Based on the slope of the unloading curve, dF/dh, the elastic modulus of the tested sample E_s can be calculated using the following equations [128]:

$$E_r = \frac{1}{2} \cdot \frac{dF}{dh} \cdot \sqrt{\frac{\pi}{A}} \tag{2.3}$$

$$\frac{1}{E_r} = \frac{1-\vartheta_s^2}{E_s} + \frac{1-\vartheta_i^2}{E_i} \tag{2.4}$$

where the E_r is the reduced elastic modulus, A the contact area, ν_s the Poisson's ratio of the sample, E_i and ν_i the elastic modulus and Poisson's ratio of the indenter tip, respectively. In this work, a Poisson's ratio, ν_i = 0.07, and Young's modulus, E_i = 1141 GPa, for the diamond indenter tip were adopted [131].

However, the indentation test is considered to characterize the local elastic modulus of the indented area as a materials property rather than the specimens' global elastic modulus that includes effects of inhomogeneity, pores and defects. Thus, to evaluate the elastic modulus for whole sample of the tested material another method needs to be used. Here, the bending test is a common method for characterizing the material's elastic behavior [132]. For adopting this method, a sample with specific simple shape and size should be fabricated. Similar like for the indentation method, the elastic modulus is determined from the load-displacement curves; however, here typically the loading curve is used, whereas in case of indentation testing the unloading curve is used due to the large plastic deformation occurring during loading in this test that typically is not the case in bending tests. As shown in Fig. 2.8, samples in different shapes like bar shape, plate shape, tube shape, due to the manufacture process or application background, can be tested using corresponding methods [132].

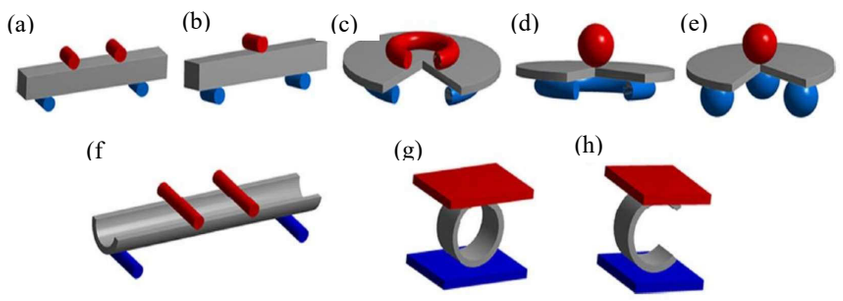

Figure 2.8 Schematic of different bending test methods: (a) (a) four-point bending, (b) three point bending, (c) ring-on-ring, (d) ball-on-ring, (e) ball-on-three balls, (f) four-point bending of semi-cylindrical specimens, (g) O-ring, and (h) C-ring [132].

In addition, the impulse excitation method is also an advanced technology for determination of the material's elastic modulus in a nondestructive way [133]. The application of impulse excitation method can be hindered if the sample has a large damping coefficient or in case of extremely thin shapes, which can lead to inaccurate results [133]. Since the solid electrolyte is always in the form of a thin plate for practical application, the indentation and bending test method are applied in this work.

2.3.2 Plastic behavior

Additionally, the plastic behavior is related to the resistance of the material to non-elastic deformation. The indentation test is a traditional method to evaluate this characteristic of materials yielding the hardness. The hardness of a material is related to the geometry of the indenter, microstructure, phase composition and to some extent, also the elastic modulus [134]. The indentation test equipped with different kinds of tips can be used to obtain hardness result, where the value can be derived from the following equation [135]:

$$H = \frac{P_{max}}{A_r} \tag{2.5}$$

where P_{max} is the maximum indentation load and A_r the residual indentation area after the indentation. In order to obtain an accurate hardness value, the sample's preparation needs to be carefully accomplished, similarly as in case of the elastic modulus determination. Another important point in the indentation test method is that the imprint load can affect the results and therefore a comprehensive range of loads need to be induced. This feature of the indentation test is referred to as indentation size effect [136].

2.3.3 Fracture toughness

Fracture toughness is an important property of a material to describe the ability to resist crack growth [137]. Especially for solid electrolyte materials, the electrolyte suffers from stresses resulting from chemical expansion and/or differences in thermal expansion if co-sintered in particular for thin-film batteries [103, 104].

The crack can be generated three modes I, II and III as shown in Fig. 2.9. Mode I is the opening mode, Mode II the in-plane shearing and Mode III the out-of-plane shearing, respectively [138].

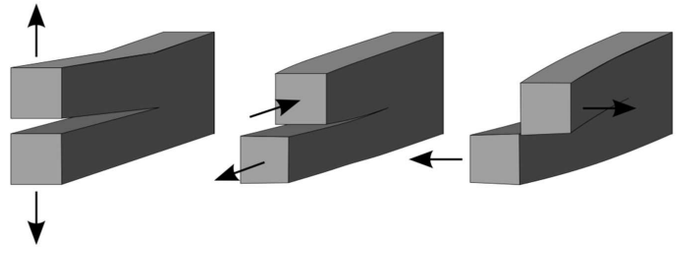

Figure 2.9 Schematic of the fracture modes: Mode I opening mode, Mode II in-plane shearing and Mode III out-of-plane shearing [139].

The occurrence of fracture is considered to result from the decrease of the free energy as expressed by the following Griffith's equation [140]:

$$\sigma_f = \sqrt{\frac{2 \cdot E \cdot G_c}{\pi \cdot \alpha}} \tag{2.6}$$

where σ_f is the fracture stress, α the defect size, E the elastic modulus and G_c the energy release. This approximation can be applied in the ideal fracture case, where only the elastic energy and new surface creation energy are to be considered. Nevertheless, the actual fracture can be more complexed by the energy dissipated in other sinks, like heat, plastic deformation, or acoustic emission. Therefore, another way considering the stress distribution around the crack was proposed, i.e., that the stress intensity factor K for each crack mode can be expressed as [141]:

$$K_i = \sigma \cdot Y \cdot \sqrt{\pi \cdot \alpha} \tag{2.7}$$

where Y is the dimensionless coefficient regarding to the crack mode. In general, ceramic materials fracture in mode I and form Griffith's crack geometries (Median), in this case Y equals

to $\sqrt{\pi}$ [142]. Thereafter, the fracture toughness K_{IC} can be evaluated once the stress reaches the fracture stress σ_f:

$$K_{IC} = \sigma_f \cdot \sqrt{\pi \cdot \alpha} \tag{2.8}$$

Thus, once the fracture toughness has been derived, the critical initial flaw size for the crack can be calculated for a given fracture stress, which is equivalent to the approach that to the tolerable stress can be assessed from fracture toughness and crack size.

Nowadays, basically three types of methods are used to evaluate the fracture toughness, conventional tests (i.e. for example notched bars), Vickers indentation fracture test based (VIF) and micro-pillar or other micro-mechanical test [143] as illustrated in Fig. 2.10. The conventional test methods have been used for a long time and can be adapted to most materials. However, the conventional test requires a number of tested specimens of discrete size, which can hinder, due to materials availability, the application of the methods [137].

The micro-mechanical methods are newly invented approaches to characterize the fracture toughness of materials, which are recognized as a novel way to evaluate the local fracture toughness, especially for those samples available only in small size. Nonetheless, these micro-mechanical tests are rather new and the fabrication of the micro-specimens is rather complicated so that this method is still under development and improvement [13, 143, 144]. Furthermore, in this work in particular regarding sintering temperature effects, the mechanical properties tested with indentation method verified to be adequate to show the trend. Hence, micro-pillar tests are out of the scope of the current work and subject of separated works like [13], in fact it has been verified in a recent work [13] that micro-pillar and indentation testing yield good agreement regarding the fracture toughness of LLZO, thus supporting the use of indentation testing to analyze the fracture toughness of solid state electrolytes, and thus the micro-pillar test method is not discussed in detail in this work.

The VIF method was chosen in this work to conduct the fracture toughness evaluation, since it has been widely used on small samples permitting a wide comparison to literature works based

on easy and straightforward specimens' preparation. For VIF test implementation the sample needs to be prepared with well-polished, low roughness and even surfaces without pre-cracks.

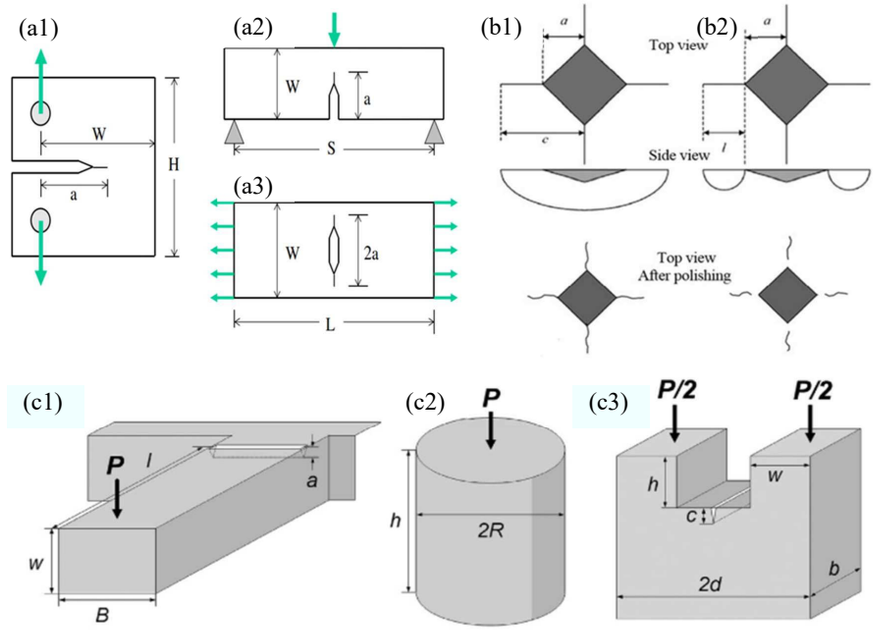

Figure 2.10 Schematic of the fracture tests, conventional methods: (a1) compact tension, (a2) single edge notched bend test (SENB), (a3) middle-cracked tension [137]; Vickers indentation fracture: (b1) radial-median crack, (b2) Palmqvist crack [145]; micro-mechanical method: (c1) single-cantilever beam test, (c2) pillar splitting test, (c3) double-cantilever beam test [143].

The VIF method can induce two crack modes, the median crack mode and the Palmqvist crack mode as shown in Fig. 2.10 (b1) and (b2), respectively. The criterion for determining the median crack mode is that the ratio of the measured length of cracks (l) to half of the diagonal (a) matched with the relation $c/a \geq 2.25$ (as verified by the experimental data, where $c = a + l$), whereas if the ratio meets the relation $0.25 \leq c/a \leq 2.5$ the crack system can typically be termed as Palmqvist mode [119]. In order to describe the relation between the fracture toughness and the indentation, different equations were developed, as listed in Table 2.4, for both Palmqvist and

median crack mode, where P is the load, E the elastic modulus and H hardness of the tested material.

Table 2.4 Equations for calculating the fracture toughness via Vickers indentation.

Crack mode	Equation		Equation No.
Radial-median	$K_{IC} = 0.0726\frac{P}{c^{3/2}}$	[146]	(2.9)
	$K_{IC} = 0.0752\frac{P}{c^{3/2}}$	[147]	(2.10)
	$K_{IC} = 0.129\left(\frac{c}{a}\right)^{-1/2}\left(\frac{H}{3E}\right)^{-2/5}\left(\frac{Ha^{1/2}}{3}\right)$	[148]	(2.11)
	$K_{IC} = 0.014\left(\frac{E}{H}\right)^{1/2}\left(\frac{P}{c^{3/2}}\right)$	[149]	(2.12)
	$K_{IC} = 0.016\left(\frac{E}{H}\right)^{1/2}\left(\frac{P}{c^{3/2}}\right)$	[119]	(2.13)
	$K_{IC} = 0.0725\left(\frac{P}{c^{3/2}}\right)$	[150]	(2.14)
Palmqvist	$K_{IC} = 0.0515\frac{P}{c^{3/2}}$	[146]	(2.15)
	$K_{IC} = 0.079\ \frac{P}{a^{3/2}}\log\left(4.5\ \frac{a}{c}\right)$	[151]	(2.16)
	$K_{IC} = 0.035\left(\frac{l}{a}\right)^{-1/2}\left(\frac{H}{3E}\right)^{2/5}\left(\frac{Ha^{1/2}}{3}\right)$	[152]	(2.17)
	$K_{IC} = 0.048\left(\frac{l}{a}\right)^{-1/2}\left(\frac{H}{3E}\right)^{2/5}\left(\frac{Ha^{0.5}}{3}\right)$	[153]	(2.18)

Since for the Vickers indentation method the precise measurement of the length of the induced crack is critical for determining the fracture toughness, advanced observation methods need to be applied like optical and electronic microscopes. Additionally, the crack mechanism can vary since, especially for higher loads imprinted on the specimen, the stress distribution can lead to complications, resulting in multi-cracks, possible spalling and even the crack extension during unloading, which are not considered by the equations. Combining the simple criterion for the crack mode [139], the transformation of Palmqvist mode to median mode is rational as the loads are increased. Therefore, the fracture toughness as calculated from different equations based on the criterion related to the ratio c/a is used in this work to compare this materials' performances criterion and compare to the values reported in literature.

2.3.4 Fracture reliability and subcritical crack growth

As the existing limitation in terms of sustainable stress is very important for application, fracture strength and failure probability are critical characteristics for ceramics [154]. The fracture stress is the critical stress to generate and propagate cracks, i.e., to create new fracture surfaces [154]. Defects inside the ceramics act as concentrator of the stresses, which leads to the stress limitation of the brittle ceramic materials [139]. Therefore, contrary to metallic materials where the yield strength is highly important, the fracture stress of the ceramics possesses a statistical feature [138]. The ceramic materials' fracture stress is relevant to the probability, i.e., with a given applied stress the capabilities of the flaws in generating facture [138]. Accordingly, it is common that the obtained fracture stresses for ceramic materials are quite scattered. To express the fracture behavior of the ceramics several statistical theories have been developed [139], of which the Weibull statistics is the most popular approach related to the weakest link possibility.

Based on the Weibull statistics, the failure probability P_f of the tested material exposed to a stress σ can be expressed as [155]:

$$P_f = 1 - \exp\left[-\left(\frac{\sigma}{\sigma_0}\right)^m\right] \tag{2.19}$$

where σ_0 is a normalization factor representing the characteristic fracture strength of a ceramic material, which relates to the failure probability of 63.2%; m is the so-called Weibull modulus describing the scatter of the fracture stresses, which is associated with the homogeneity of the specimen (defect distribution) [156]. If the Weibull modulus m is close to 0, the failure probability of the material can be around 1 for any fracture stress, i.e., the material can fracture at any applied stress. In contrast, if m is close to infinity, the material can fracture only at the applied stress equivalent to characteristic fracture strength σ_0. These two parameters are both important in characterizing the ceramic materials' fracture strength diversity.

Furthermore, especially the characteristic fracture strength can be affected by the specimen's volume, geometry, shape porosity, probability of preexisting defects [138], etc., which indicates

that a comparison of the fracture strength needs to be conducted cautiously. Defects which can lead to cracks might be distributed randomly through the specimen volume or are concentrate in the surface or edges of the specimen due to the manufacturing process [157]. Hence, the probability of occurrence of larger or more cracks increases for a bigger volume, which indicates larger samples get weaker. In addition, the shape, geometry, loading approach as well as the defects amount and types can also influence the stress distribution relating to the Weibull statistics [139].

A series of methods have been developed to measure fracture stresses (see also Fig. 2.8). It should be noticed that the compressive strength of ceramic materials is typically higher than the tensile strength [143] and mostly the maximum stress at fracture is considered as the fracture stress. Due to the complicated application conditions, samples need to be modified into specific geometries and shapes to mimic the working environment as illustrated in Fig. 2.8 to provide fracture property information. For solid electrolytes materials typically manufactured as thin pellets for battery cell, the ring-on-ring (ROR) and ball-on-3-ball (B3B) tests, illustrated in Fig. 2.8 (c) and (e), are applied in this work to determine the characteristic strength and Weibull modulus; more details can be found in the section Experimental.

To display the scattering of the results the uncertainty needs to be estimated. Yet the characteristic strength is obtained based on the probability distribution. The uncertainty of the Weibull statistics can be estimated including the probabilities distribution via a certain confidence interval. Normally, the probability failure distribution within a confidence level of 95% is adequate to indicate upper and lower bounds of characteristic strength and Weibull modulus. Thus, the lower and upper bounds for the characteristic fracture strength can be calculated via the following equations from the standard [158]:

$$C_l = \sigma_0 \cdot e^{-\frac{t_l}{m}} \tag{2.20}$$

$$C_u = \sigma_0 \cdot e^{-\frac{t_u}{m}} \tag{2.21}$$

where C_l and C_u are the lower and upper bounds, t_l and t_u the constants relating to the given confidence interval and the amount of tested samples. For the Weibull modulus the lower and upper bounds can also be estimated by the same standard as following [158]:

$$D_l = \frac{\mathrm{m}}{l_l} \tag{2.22}$$

$$D_u = \frac{\mathrm{m}}{l_u} \tag{2.23}$$

where D_l and D_u are the lower and upper bounds, l_l and l_u the constants can be found in the standard. An illustration of the interval for a Weibull statistics of a material can be drawn with the upper and lower bounds of both characteristic fracture strength and Weibull modulus. As an example a schematic can be seen in Fig. 2.11.

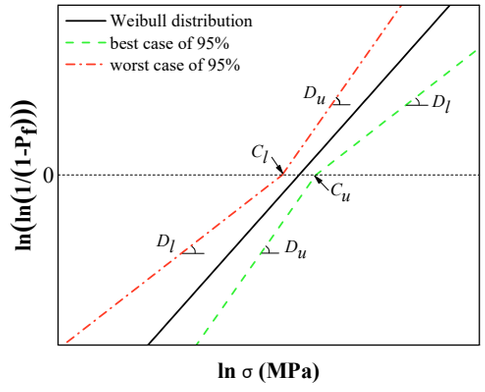

Figure 2.11 Illustration of the confidence interval for an arbitrary Weibull distribution.

Moreover, for ceramic materials, cracks can nucleate and propagate under a stress lower than the fracture stress. Thus, this phenomenon needs to be considered, where the material suffers from crack growth with the assistance of electrochemical reaction [138]. As the crack tip constantly interacts with the environment, the breakage of the atomic bonds can occur which leads to the crack propagation, which is termed subcritical crack growth (SCG) behavior [155]. The direct method to evaluate the SCG sensitivity of a material is to conduct mechanical tests

with distinguished stress rates [155]. Additionally, based on the sensitivity test regarding subcritical crack growth a lifetime assessment of the ceramic material under a given load can be derived [159]. This failure probability combined with stress and time dependence can be depicted in a stress probability time (SPT) diagram [159, 160]; the analysis process is outlined in the section Experimental.

2.3.5 Concerns regarding mechanical behavior of solid electrolytes

Inside all solid state lithium ion batteries, the solid electrolyte is directly in contact with anode and cathode materials to act as separator and lithium ion conductor. Regarding mechanical properties, the elastic modulus of the electrolyte materials in battery application is important, especially for analyzing applied strain – induced stress relationships. Overall, it is preferential that the solid electrolytes deforming elastically to maintain contacting with the electrodes, once the volume changes during charge/discharge [50]. Hence it is suggested that the materials with not too high elastic modulus can be good options for the electrolytes application. Although the solid electrolytes possessed low stiffness are preferred to be used for the bulk type battery design [161], further investigation reports that the solid electrolytes possessing elastic modulus of lower than 15 GPa are more inclined to dendrite related crack initiations [112].

Another essential issue is the mismatch of the expansions and contractions on the electrolyte and electrodes, due to the lithium ion migration during the cycling inducing chemical strain [78]. This phenomenon can result in the formation of micro-cracks and even lithium dendrites. An electro-chemo-mechanical model was proposed assuming an electrolyte with elastic modulus of 15 GPa and fracture energy of higher than 4 J/m^2, in this case the fracture can be avoided if the electrode expansion is lower than 7.5% [112]. Hence, fracture and elastic properties of the material need to be considered simultaneously for the battery application.

Inhomogeneity in the microstructure within the interface of electrolyte and electrodes can lead to the interior tensile and shear strengths in the battery cell [112]. In extreme operating conditions, like external shocks on battery, or even during the sintering process, the solid electrolytes inside battery cell suffer from the external impact and scratch conducted from the

electrodes [42]. Ceramics with higher hardness than that of typical polymer electrolytes are probably capable to support the battery cell avoiding mechanical shock effects [162]. Reliability under such situations requires not only high quality of the components regarding homogeneity, surface flatness, but also the precise assessments of the elastic modulus, hardness and fracture properties of the solid electrolytes for safe design [108].

Furthermore, regarding planar micro-batteries, where the thickness of the electrolyte can be a few microns (with a total unit cell thickness of < 20 μm) [9], the preferred orientations of the electrolyte ought to be selected to achieve better separation and support for the electrodes. Concerning the crystal structure of the materials, it is known that rhombohedral materials (can be expressed in hexagonal notation [163]) like hematite (α-Fe_2O_3) and corundum (α-Al_2O_3) with space group of $R\bar{3}c$ possess a prominent anisotropy in mechanical properties and also other properties like magnetism [126, 164]. Nevertheless, the anisotropic property for rhombohedral or hexagonal structures is not as strong as in case of cubic or tetragonal crystal structure materials [165]. LATP has a rhombohedral crystal structure (space group: $R\bar{3}c$), of which the unit crystal can be expressed in hexagonal notation [163], whereas the LLZO material is in both cubic and tetragonal structure and LLTO material is mainly in cubic crystal structure [166]. Thus, the anisotropy of the mechanical properties of LATP appeared to be most interesting and is selected for investigation to gain a deeper understanding of the material, which is then also beneficial for any potential application in micro-scale devices. Besides, since it was reported that the performance of solid electrolyte sintered with additive of SiO_2 can be enhanced [167, 168], the LATP sintered with SiO_2 as binder was selected to study the fracture reliability to compare with the pure LATP [12]. In addition, as mentioned, during cycling in solid-state lithium batteries, the uptake and release of lithium ions in electrodes and electrolyte leading to the volume dilation referred to chemical expansion can result in mechanical instability during operation [103]. The bond length variation of the lattice related to the chemical expansion influences the electrochemical and mechanical properties [104]. The chemical expansion also plays an important role in interfacial process and stability of the electrodes and electrolyte, hence it needs to be investigated if the mechanical properties of the electrolytes are beneficial for battery cell design [106]. The LLTO electrolyte, a material being close to application, is selected hence to investigate potential voltage state effects on the mechanical performance indicators [15-17].

To evaluate elastic modulus and hardness of the ceramics several aspects need to be considered. The lattice parameter, secondary phase, porosity as well as the grain size synergistically or competitively affects the elastic modulus and hardness of the solid electrolyte and further influence the fracture properties and even the lifetime [169]. It has been reported that, to some degree, the currently considered solid electrolyte also suffers from effects related to the temperature applied during sintering, stoichiometric repeatability, grain boundary blocking effect and also electrochemical uncertainty [170]. In addition, the lithium intercalation during the cycling of voltage state can cause the lattice variations, which will also potentially impacts the mechanical properties [171].

2.4 Mechanical properties of solid electrolytes

Although the electro-chemical behavior of solid electrolytes is the main aspect of materials development, the mechanical properties are also an important factor for their practical application [42]. According to the Monroe's linear elasticity theory the shear modulus of the electrolyte needs to be two times higher than the Li metal, which is related to the elastic modulus [117]. For the ceramic materials used as solid electrolyte, hardness and fracture toughness are also key property for application, as they describe the ability of the material to resist penetration of the lithium dendrites and the fracture [137]. In addition, as the ceramics that are brittle possess an inherent scatter in fracture stresses, the fracture reliability analysis is important for ceramic electrolytes to understand the brittleness property [172]. Thus, the mechanical properties, like elastic modulus, hardness and fracture toughness, of the electrolytes materials are essential to be investigated for further battery cell design. Some investigations on the mechanical properties other than the electro-chemical properties of the electrolytes especially the LATP, LLZO, LLTO materials have been reported, as listed in Table 2.5.

As shown in Table 2.5, a wide range of elastic moduli values for electrolytes exist. Particularly, Sulfide, LISICON and LiPON solid electrolytes tend to be much more compliant than the other oxide electrolytes [161, 173-175]. It can be noticed that the elastic modulus for $Li_{1.3}Al_{0.3}Ti_{1.7}(PO_4)_3$ (LATP) is in the range 81 – 115 GPa, for $Li_7La_3Zr_2O_{12}$ (LLZO) it is 124 –

163 GPa and for $Li_{0.350}La_{0.557}TiO_3$ (LLTO) 143 – 203 GPa [12-15, 17, 176-180]. LLTO material possesses the highest *E* value, whereas the LATP material has the lower values.

Table 2.5 A brief collection of mechanical properties of solid electrolytes.

Electrolyte	Compound	Test method	Elastic modulus (GPa)	Hardness (GPa)	Fracture toughness ($MPa \cdot m^{1/2}$)
Sulfide	$Li_2S–P_2S_5$ [161]	RUS	18 – 25	–	–
	$Li_2S–P_2S_5$ [173]	Indentation	~18	–	0.23 ± 0.04
LISICON	$Li_{10}GeP_2S_{12}$ [174]	Sim	37	–	–
LiPON	$Li_xPO_yN_z$ [175]	Nano	77	3.9	–
NASICON	$Li_{1.3}Al_{0.3}Ti_{1.7}(PO_4)_3$ [12]	Strain-stress	81 – 115	7.1	1.1
	$LiTi_2(PO_4)_3$ [166]	Sim	143.7	–	–
Garnet	$Li_7La_3Zr_2O_{12}$ [14]	Nano	124 – 163	9.0 – 11.8	–
	$Li_7La_3Zr_2O_{12}$ [176]	Indentation	–	6.8 – 9.9	0.60 – 0.82
	$Li_7La_3Zr_2O_{12}$ [13]	Nano	145.6 ± 7.3	8.5 ± 0.4	0.99 ± 0.05
	$Li_{6.24}La_3Zr_2Al_{0.24}O_{11.98}$ [177]	RUS	149.8 ± 0.4	6.3 ± 0.3	–
	$Li_{6.19}Al_{0.27}La_3Zr_2O_{12}$ [181]	Nano	135 – 140	4.3 – 9.1	1 – 1.3
	$Li_{6.24}La_3Zr_2Al_{0.24}O_{11.98}$ [179]	Indentation	–	–	0.86 – 1.63
	$Li_{6.17}Al_{0.28}La_3Zr_2O_3$ [182]	Sim	146 – 163	–	–
Perovskite	$Li_{0.33}La_{0.57}TiO_3$ [15]	RUS	186 – 200	–	0.89 – 1.34
	$Li_{0.33}La_{0.57}TiO_3$ [15]	Indentation	200 ± 3	9.5 ± 0.7	1 ± 0.04
	$Li_{0.33}La_{0.57}TiO_3$ [180]	RUS	223	–	–
	$Li_{0.33}La_{0.57}TiO_3$ [17]	RUS	143 – 203	8.1 – 9.5	1.15 – 1.24
	$Li_{0.5}La_{0.5}TiO_3$ [166]	Sim	233.9 – 262.5	–	–

* RUS: resonant ultrasound spectroscopy, Nano: nano-indentation, Stress-Strain: slope of stress-strain curve, Sim: simulation.

The experimental elastic modulus results can be compared with the simulation results, which predicts the $LiTi_2(PO_4)_3$ of ~143 GPa, $Li_{6.17}Al_{0.28}La_3Zr_2O_3$ of 146 – 163 GPa, and $Li_{0.5}La_{0.5}TiO_3$ of 234 – 263 GPa [166, 182]. Hence, simulation prediction results of LATP, LLZO and LLTO materials are in close agreement with experimental results and also show the same trend.

The hardness results of the solid electrolytes are also listed in Table 2.5. It can be seen that the hardness for $Li_{1.3}Al_{0.3}Ti_{1.7}(PO_4)_3$ (LATP) is ~7.1 GPa, for $Li_7La_3Zr_2O_{12}$ (LLZO) it is in the range 6.8 – 11.8 GPa and for $Li_{0.33}La_{0.57}TiO_3$ (LLTO) it is 8.1 – 9.5 GPa [12-15, 17, 176]. The *H* value of LiPON, $Li_xPO_yN_z$ material (~3.9 GPa) is lower than that of the LATP, LLZO and LLTO materials [175]. The hardness value of LLTO material is higher than that of the LATP material, whereas it's hard to compare the hardness of LLZO with that of other two materials due to the big range of the reported hardness results. Besides, the *H* value of $Li_{6.19}Al_{0.27}La_3Zr_2O_{12}$ material is in the range of 4.1 – 9.1 GPa, which is lower than that of the $Li_7La_3Zr_2O_{12}$ material and effect that can be ascribed to compositional differences [177, 178]. Moreover, the hardness values can also be adopted to assess the nature of atomic bonding, which has been reported by Gilman et al. [183], i.e. that the ratio of the hardness to shear modulus of the crystal material gives information on the bonding type.

As discussed above, fracture toughness is an important property for solid-state electrolytes representing resistance to crack growth that could occur during cell assembly or battery operation. The fracture toughness values are also shown in Table 2.5 and it can be seen that the LATP, LLZO and LLTO materials possess a similar K_{IC} value, being close to ~1 $MPa{\cdot}m^{1/2}$ [12, 13, 15, 17, 176, 178, 179], whereas the Sulfide $Li_2S–P_2S_5$ material reveals an obviously lower K_{IC} value [173]. Generally, ceramic materials exhibit fracture toughness values from ~0.3 to 5 $MPa{\cdot}m^{1/2}$, whereas metals exhibit much higher fracture toughness values in the range of ~20 to 100 $MPa{\cdot}m^{1/2}$ [159, 184]. The K_{IC} value for LATP, LLZO and LLTO materials are quite low for ceramic materials, which suggest these three ceramic electrolyte materials are rather brittle.

Jackman et al. reported on the Weibull statistics parameters of LATP with different grain sizes, where the strength varied from 30 to 130 MPa, and Weibull modulus was in the range of 5 – 12 [12]. The biaxial fracture strength of the LATP material was investigated by Cutler et al. [185], indicating that, with exposure to different solutions, the strength varied from 144 MPa measured in air to 191 MPa measured in mineral oil. The Weibull statistics of LLTO materials were assessed by Schell et al. [17], yielding that the characteristic fracture strength was 146 – 158 MPa and Weibull modulus was 7 – 15.9, where the variation in the properties was explained by different microstructural aspects. Nevertheless, Weibull statistics investigations on LLZO

materials are limited, where it should be considered that they depend on individual production processes due to respective influences on defect distributions.

Although the awareness on the importance of the mechanical characterization and characteristics of the ceramic electrolytes is improving, compared to the electro-chemical characteristics a comprehension of the mechanical properties on these materials is still limited especially being inadequate to warrant long-term reliability. Hence, the aim of the current work is to study mechanical features and microstructure relationships of solid ceramic electrolytes, in particular for the three materials LATP, LLZO and LLTO, which are chosen due to the promising electro-chemical properties, as indicated in Table 2.2. To widen comprehension of the mechanical properties of LATP materials, which is newly-developed compared to the LLZO and LLTO materials, hot-pressed LATP materials sintered at various temperatures in the range of 950 °C to 1100 °C were selected to investigate sintering temperature effects on the mechanical properties. Meanwhile LATP sintered at 1100 °C, which revealed higher elastic modulus and hardness than the other LATP samples, was selected to study the grain orientation effect related to the rhombohedral crystal structure. Since the fracture strength of pure LATP has been reported by Jackman et al. [12] and the performance of solid electrolyte sintered with additive of SiO_2 can be enhanced [167, 168], tape casted $Li_{1.5}Al_{0.5}Ti_{1.5}(PO_4)_3$ mixed with SiO_2 (LATP:Si) was selected here to investigate the fracture reliability and to see if the mechanical properties can be improved with the SiO_2 binder in a tape casting process. In addition, the fracture reliability of the alternative material LLZO was studied in this work to permit comparison, where elastic modulus, hardness and fracture toughness were not studied here since they have been reported elsewhere [13, 14]. As the electrolytes in all-solid-state lithium batteries are operated under cyclic voltage condition that are associated with chemical expansion effects, exemplified for LLTO, a material being close to application [15-17], voltage effects on mechanical properties were studied. The relation between the mechanical properties and microstructure of the materials i.e. phase information, grain size, porosity etc. is always discussed.

3. Experimental

Within the framework of this work, several solid ceramic electrolyte materials were produced and made available by partners. Details on materials production and characterization are given in the following.

3.1 Materials production

$Li_{1+x}Al_xTi_{2-x}(PO_4)_3$ (LATP) samples sintered at different temperatures were produced by IEK-9, Forschungszentrum Jülich. $Li_{1.5}Al_{0.5}Ti_{1.5}(PO_4)_3$ mixed with SiO_2 and $Li_7La_3Zr_2O_{12}$ (LLZO) samples were synthesized in IEK-1, Forschungszentrum Jülich. Details on the processing of these materials are given in the following subsections. $Li_{0.350}La_{0.557}TiO_3$ (LLTO) disks were sintered via a traditional solid reaction method at University of Science and Technology Beijing (USTB), China.

3.1.1 $Li_{1+x}Al_xTi_{2-x}(PO_4)_3$ (LATP)

The production of the material followed the procedures outlined in [186]. Firstly, the LATP powder was prepared by a conventional sol-gel synthesis method. As a typical synthesis, a gelatinous white precipitate was produced by 25 ml of $Ti(OC_3H_8)_4$ mixed with 50 ml NH_4OH (Aldrich, 30% solution). Deionized water was used to wash the precipitate to remove the excess base and then the precipitate was stored in 100 ml of deionized water. 200 ml of 1 M oxalic acid (Aldrich, 99.9%) were added to produce a clear solution of $H_2[TiO(C_2O_4)_2]$. Then stoichiometric $Al(NO_3)_3{\cdot}9H_2O$ (Aldrich, 99.9%), $(NH_4)_2HPO_4$ (Aldrich, 98%) and 5% excess $LiCOOCH_3{\cdot}2H_2O$ (Aldrich, 98%) were mixed into the clear solution under stirring. The mixed solution was heated up to 80 °C on a hot plate to evaporate the water, then a white precipitate of mixed precursors was acquired to be used in the subsequent annealing process. A pre-annealing was conducted for the mixture in air at 850 °C for 5 h. After the pre-annealing, the LATP powders were grinded and put into a cylinder pressing mold with the diameter of 11 mm for uniaxial die, applying a pressing force of 40 kN. Afterwards the obtained cylindrical shaped LATP pellets were pressed isostatically at 1425 kN for 10 s and then sintered at various temperatures in the range of 950 °C

to 1100 °C with 50 K steps. The LATP sintered at different temperatures are named as LATP 950 °C, LATP 1000 °C, LATP 1050 °C and LATP 1100 °C.

3.1.2 $Li_{1.5}Al_{0.5}Ti_{1.5}(PO_4)_3$ mixed with SiO_2 (LATP:Si)

The LATP ($Li_{1.5}Al_{0.5}Ti_{1.5}(PO_4)_3$) powders were prepared by a solution assisted solid state reaction described elsewhere [187]. The LATP powder was calcined at 750 °C. After calcination the powder, it was ball-milled in ethanol with ZrO_2-balls for 24 h, then dried at 80 °C for another 24 h and mortared to yield fine powders. For tape casting method the LATP powder was dispersed in a mixture of ethanol, methylethylketone, polyvinylbutyral (Butvar B-98), Nousperse FX9086 (Elementis Specialties), Polyethylene glycol (PEG400) and Solusolv S-2075 (Solutia Inc.). The SiO_2 (amorphous, nanopowder, ALFA Aesar) was added to the mixture. The homogenized dispersion was then de-aired at 20 kPa for 10 minutes and then cast using a "tape-caster" with a slit height of 150 – 400 µm with a drawing speed of 3 mm/s. The cast film was dried and cut into circular discs that were sintered in air at temperatures of 850 – 1000 °C for 1 h yielding 50 – 150 µm thick sheets.

3.1.3 $Li_7La_3Zr_2O_{12}$ (LLZO)

The lithium lanthanum zirconate $Li_7La_3Zr_2O_{12}$ with 2 mol% Al doping, 40 mol% Ta doping (LLZO) powders was synthesized via a three step solid-state reaction in argon atmosphere. The raw materials were prepared from $LiOH{\cdot}H_2O$ (98%; Merck), La_2O_3 (99.9%, dried at 900 °C, 10 h; Merck), ZrO_2 (99.5%, Treibacher), Al_2O_3 (99.9%, Inframat) and Ta_2O_5 (99.5%, Inframat). Via grinding in a mortar (Retsch RM 200) for 1 h and pressed with a uniaxial press into pellets, the mixtures were homogenized. A subsequent calcination at 1000 °C for 20 h in argon was done. After calcination the pellets were transferred into an argon glove box to avoid the oxidation and ground into fine powders. For final sintering, about 6 g of calcined LLZO powders were selected and uniaxial pressed with 115 MPa in a 13 mm die to a pellet (diameter ca. 12 mm). The pellets were sintered at 1200 °C in air for 8 h. The resulting dense pellets were cut into slices of 1 mm thickness for the subsequent investigations.

3.1.4 $Li_{0.350}La_{0.557}TiO_3$ (LLTO)

$Li_{0.350}La_{0.557}TiO_3$ disks were produced on the basis of synthesizing by traditional solid reaction methods. Reagents of La_2O_3 (99.99%), Li_2CO_3 (99.9%) and TiO_2 (99.9%) were selected as raw materials. The raw materials were mixed with the ratio of molar composition in an agate jar for 6 hours (h) with ethanol as the milling agent, and after drying the mixed powder was calcined at 1100 °C for 8 h in air. The calcined powder was ball-milled again in the agate jar, and then the fine calcined powder was uniaxially pressed into disks (diameter: ~10 mm, thickness: ~1.2 mm) under a pressure of 180 MPa. The disks were sintered at 1200 °C for 10 h in the air with a heating rate of 3 K min^{-1} and a cooling rate of 10 K min^{-1}.

The $Li_{0.350}La_{0.557}TiO_3$ disks were polished and assembled into a half-cell with a Swagelok mould. The $Li_{0.350}La_{0.557}TiO_3$ disk was used as cathode and Li metal was applied as anode in the cell. The electrolyte was 1 M LiPF6 dissolved into a mixture of ethylene carbonate EC/DMC (1:1, v/v). The voltage of the as-prepared disks was 3.2 V, which was named as LLTO-3.2V. Other disks were charged (or discharged) to 4.5 V, 4.0 V and 0.2 V, and correspondingly the disks were named as LLTO-4.5V, LLTO-4.0V, and LLTO-0.2V, respectively. The disks were charged (or discharged) at a constant voltage (LANDCT2001A, Jinnuo Wuhan, Hubei, China) until the current was less than 2 μA. The disks were not re-polished after charging process prior to measurement.

3.2 Materials characterization

3.2.1 X-ray diffraction

X-ray diffraction (XRD) is a widely used non-destructive technology in materials' structural analysis and phase characterization. The basic of the XRD technique is that the atoms in the crystalline sample cause the beam of incident X-rays to diffract into many specific directions. With the detected intensities and angles of those diffracted beams the density of electrons inside the crystal can be determined, from which, the crystal information like mean position of atom, chemical bonds, disorder and other information can be obtained. The working principle of XRD is based on the Bragg's law, which yields the following equation:

$$n \cdot \lambda = 2 \cdot d \cdot \sin\theta \tag{3.1}$$

where the d is the distance between the neighbored atomic layers, θ the reflection angle, n one integer number and λ represents the X-ray wave length. The Bragg's law means that, for a fixed X-ray wave length λ, the reflection angle θ will only occur for a crystal with a specific inter-planar distance d.

The X-ray diffraction (XRD) structural analysis and phase characterization was based in the current work on a Bruker 4 Endeavour spectrometer equipped with a 1D detector LYNXEY and a DIFFRAC^{plus} BASIC package 2009 using Cu-K_α radiation. All samples were characterized at room temperature. For LATP material the rhombohedral structure (PDF#42-7621 $Li_{1.2}Al_{0.2}Ti_{1.8}(PO_4)_3$) was referred and the scanning range was 10° to 130° with the step of $\Delta 2\theta$ = 0.02° and 2 s. All diffraction peaks of the LLTO-3.2V, LLTO-4.0V and LLTO-4.5V samples are indexed to the cubic structure (PDF#46-0465 $Li_{0.35}La_{0.55}TiO_3$), and the scanning range was 10° to 90° with the step of $\Delta 2\theta$ = 0.02° and 2 s. The synthesized LLZO powders were analyzed in a 2θ range of 10° to 100° with a $\Delta 2\theta$ = 0.02° and 2 s per step with a reference of $Li_7La_3Zr_2O_{12}$ (PDF#99-0034). Analysis of the secondary phase of the samples was also based on the XRD tests.

3.2.2 Scanning electron microscopy and electron backscatter diffraction

Scanning electron microscopy (SEM) is an analysis method that derives the sample surface microstructure and topographies by scanning the sample surface with a focused high energy electron beam. The focused electron beam interacts with the atoms inside the sample, which emits several kinds of signals that can be deconvoluted into information of the sample surface's topography, composition and other properties [188]. High vacuum is applied in conventional SEM to keep the electrons path clear and signals detectable. Magnetic lenses are employed to help focus the electron beam exactly on the sample surface. The amplified signal detected from the surface represents one pixel of the produced image and then the beam moves to the next position of the surface until the selected area is imaged. The signals generated by the interaction of the electron beam and the sample include secondary electrons, back-scattered electrons,

characteristic X-rays, Auger electrons and light, as shown in Fig 3.1. In all SEM rigs, the secondary electron imaging can bring the sample surface details less than 1 nm in size, whereas the detectors for other signals depend on the manufacturer of the SEM.

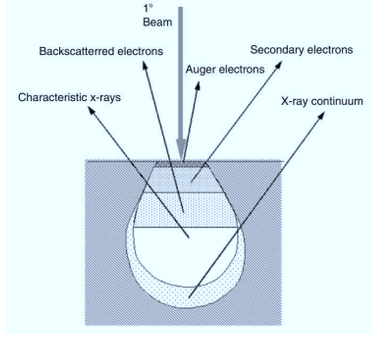

Figure 3.1 Interpretation of the signals produced by the interaction between the electron beam and the sample and the regions from which the signals can be detected [188].

Electron backscatter diffraction (EBSD), when integrated with a SEM as an additional part, permits the characterization of the individual grain orientation, texture, phase identification and distribution on the surface of the polycrystalline sample. The observation of a diffraction pattern in backscattering mode was already reported by Nishikawa and Kikuchi and discussed together with the transmission electron microscopy Kikuchi patterns [189]. After decades of developing on this technique, EBSD has been a mature alternative to the X-ray pole figure measurements in quantitative texture analysis. Nevertheless, limitations for EBSD still exists for instance the sample must be compatible with the requirements of electron microscopy, for example the grain size should be larger than dozens of nanometers.

An automated EBSD rig contains three main parts: SEM, camera and the software. For the sake of the better acquisition of the pattern signal, the sample surface tilts around 70° with respect to the incident beam and the emitted back-scattered electrons project to a phosphor, as shown in Fig 3.2 [190]. In contrast to the schematic in Fig 3.2, where only one Kikuchi band is

illustrated, in real application normally much more of such bands have to be considered. The Bragg's law can be applied again to confirm the crystal plane corresponding to the band related to the specific inter-planar spacing *d*. To fully quantify the mechanisms on formations of the diagnostic diffraction features in EBSD patterns, including the Kikuchi bands and the circular Kikuchi tracks around zone axes, the electron diffraction dynamical theory should be employed [191]. The observed bands can then be sorted with respect to the intensities and widths. Indexing process is based on the comparison of the inter-planar angle and inter-planar spacing (which represent angle between Kikuchi bands and band width, respectively), with theoretical values of the known actual crystal structure. Commonly, for high crystal symmetry case 5 to 10 smallest and most intense bands are passed to the indexing routine and consideration of 3 to 4 {*hkl*} families are sufficient to solve the backscattered Kikuchi pattern, whereas for lower crystal symmetry more bands and more families need to be checked and considered. The reference coordinates of the specimen (normal direction and transverse direction) are finally indexed, and four different ways are used to describe the crystallographic: miller notion: (*hkl*)[*uvw*], rotation matrix: *g*, Euler angle: (φ1, Φ, φ2), and angle and axis pair: θ [*r*1, *r*2, *r*3]. In this work the miller notion and Euler angle are often used. To observe the surface and cross-sectional surface of the sample, indentation and crack propagations, as well as the grain orientation of the LATP sample, a SEM integrated with an EBSD (Zeiss SUPRA 50VP) in IEK-2 was used.

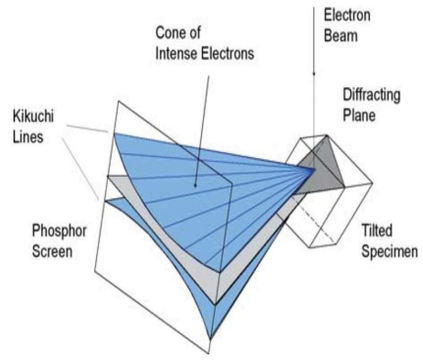

Figure 3.2 Schematic of the intense electrons' cone regarding to the specimen, reflecting plane and phosphor screen [190].

3.2.3 Electrochemical impedance spectroscopy

Being solid electrolytes, measurement of the ionic conductivity of the materials is quite important for the real application. Though the samples were prepared by different institutes, where also the impedance was characterized, the working principle for Electrochemical Impedance Spectroscopy (EIS) is the same. The top and bottom sides of samples needed to be polished with up to 1200 grid sandpaper to flatten surface and remove the potential contamination. Thin Au layers were sputtered on both surfaces as blocking electrodes providing also a good contact to the pellets. The impedance was measured with a potentiostat with built-in frequency response analyzer. As for calculating the ionic conductivity, the following equation was used:

$$\tau_{\text{ionic conductivity}} = \frac{t}{R_b \cdot A} \tag{3.2}$$

where R_b is the bulk electrolyte resistance as determined from the impedance analysis, t the thickness of the electrolyte, and A the contact area of the interfaces between the electrolyte and the blocking electrodes.

For LATP sintered at IEK-9 the impedance was measured with a potentiostat (Bio-Logic, SP-300), of which the measurements were conducted from 7 MHz to 1 Hz with peak–to–peak voltage amplitude of 10 mV. To gain the impedance of LLTO from USTB an impedance analyzer (Agilent 4294A, Agilent Technologies, Santa Clara, CA, USA) was used in the frequency range from 4 to 10^5 Hz with an amplitude of 10 mV. The ionic conductivity of LATP:Si and LLZO from IEK-1 was evaluated by an “Alpha A High Performance Frequency Analyzer” (Novocontrol Technologies) with the range of range of 1 Hz to 20 MHz and an electrical amplitude of 20 mV.

3.2.4 Porosity measurement

For ceramic materials the porosity has a significant influence on the mechanical properties. The conventional Archimedes’ method was applied to assess the relative density of all materials. In order to investigate the porosity effect corresponding to sintering temperature on the

mechanical properties of LATP samples, one geometric method and one image analysis method were employed to verify the Archimedes' method's porosity result.

In case of the Archimedes' principle the immersion of sample into the fluid led to the volume change of the fluid and the lifting force change due to the buoyancy. Take the density of the fluid into consideration the density of the sample could be obtained. Combined with the theoretical density of the material the relative porosity of the sample could be calculated. In this work the Archimedes' density was tested in water.

The second method was based on defining the bulk density from the mass and geometry volume when the sample was manufactured into a regular appearance. Both the mass and the geometric size were evaluated at least 5 times to gain a credible value. Then the relative density was calculated as the ratio of the bulk density divided to the theoretical density of measured samples.

In the third method the relative density was terminated by the porosity volume percent via image analysis with the commercial software of AnalySIS pro (Olympus Soft Imaging Solutions GmbH). The principle of the image analysis for porosity calculation is to set a threshold for a selected SEM image of the sample to distinguish the pores from the material due to high contrast. Then converting the image to a binary pixel image according to the threshold, the porosity could be calculated as the ratio of the area of the district above the threshold to the whole area. Furthermore, the grain size of the samples could also be determined with the software. The mean value of grain size was defined by probing the amount of the intercepts generated by test lines and circles across grain boundary traces in the chosen images [192].

3.3 Mechanical characterization

3.3.1 Indentation test

The indentation test can be used for evaluation of the mechanical properties of elastic modulus, hardness and fracture toughness of a material [193]. The nanoindentation technology was firstly developed in the mid-1970s to measure the hardness of the materials with small

volume [194]. The calculation of elastic modulus (E) and hardness (H) can be based on the well-known Oliver & Pharr procedure [128]. A typical load-displacement curve for an indentation is shown in Fig. 3.3.

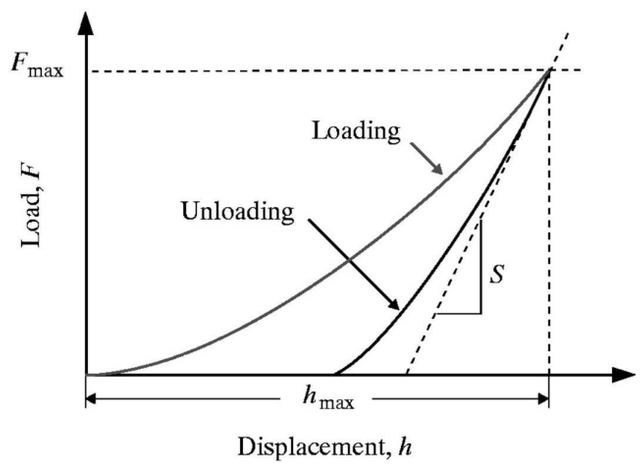

Figure 3.3 Schematic of the load-displacement curve for typical indentation test, in which the S is the contact stiffness.

The slope of curve upon unloading, dF/dh, is indicative of the stiffness S as indicated in Fig. 3.3. The stiffness normally contains the contributions from both the response of the test machine itself and the tested material. With the stiffness and the contact area A the reduced elastic modulus E_r can be calculated based on the following equation [128]:

$$E_r = \frac{1}{2} \cdot \frac{dF}{dh} \cdot \sqrt{\frac{\pi}{A}} \tag{3.3}$$

As the stiffness contains the contribution from the test rig, which means the elastic deformation of the indenter is also included, the specimen's elastic modulus can be calculated using the relation:

$$\frac{1}{E_r} = \frac{1-\vartheta_s^2}{E_s} + \frac{1-\vartheta_i^2}{E_i} \tag{3.4}$$

where E_i and ν_i are the elastic modulus and Poisson's ratio of the indenter tip, respectively, ν_s the Poisson's ratio of the sample. In this work, the Poisson's ratio, $\nu_i = 0.07$, and Young's modulus, $E_i = 1141$ GPa, of the diamond indenter tip were adopted [131].

The indentation hardness of the sample can be calculated, as expressed by the following equation, as the ratio of the maximum load to the residual indentation area A_r, which is related to the diagonal of the imprint after indentation [135]. For each load 20 indentations were employed.

$$H = \frac{P_{max}}{A_r} \tag{3.5}$$

Fracture toughness (K_{IC}) is a property describing the resistance of the material to fracture. A conventional Vickers indentation method [152] was applied here to assess the local fracture performance of the sample. In Fig. 3.4 the crack modes induced by the indentation are illustrated, in which the left one is the median crack mode and the right one is the Palmqvist crack mode. AnalySIS pro software was used to measure the diagonal of the imprints and the length of the induced cracks .

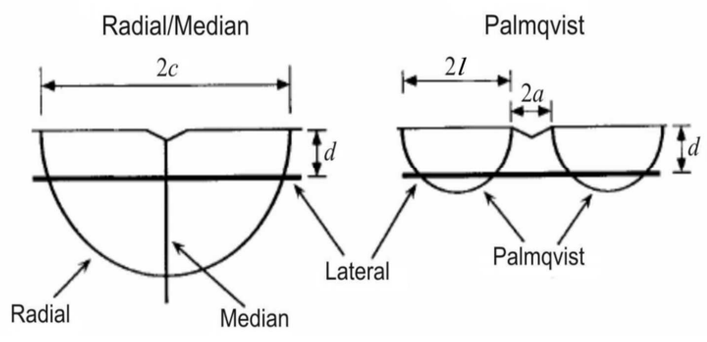

Figure 3.4 Principle scheme of the indentation crack modes [195].

The criterion for determining the median crack mode is that the ratio of ratio of the measured length of cracks (l) to half of the diagonal (a) matched with the relation $c/a \geq 2.25$ (as verified by

the experimental data, where $c = a + l$) [119]. The fracture toughness of the material under median crack mode can be derived from the empirical equation [137]:

$$K_{IC} = 0.016\left(\frac{E}{H}\right)^{1/2} \cdot \frac{P}{(c)^{3/2}} \tag{3.6}$$

where the E and H are the elastic modulus and hardness of the material, respectively, P is the indentation load and c the crack length.

Before the indentation test, all the samples were embedded in water free resin and again polished to remove the potentially contaminated as-sintered surface and make the surface smooth. Specimens were polished with sandpaper from 400 to 5000 grit and using polishing suspensions of water-free Polyethylene Glycol (PEG) mixed with 0.2 μm SiO_2. Using a polishing system without water permitted to protect the samples from proton/lithium transaction as a result of absorbed water, hence the mechanical properties were not affected by moisture.

Two nanoindentation machines were applied to gain the elastic modulus and hardness of the materials in different load ranges. To ensure the data validity standard materials (fused silica and BK-7 glass) were used to calibrate tip and machine compliance [196, 197]. A Fischerscope H100C (Helmut Fischer KG, Sindelfingen) with a Vickers tip was adopted in this work to carry out the indentations at room temperature on all samples. Various loads (30, 50, 100, 300, 500 mN) were applied to obtain the E and H. At each load 20 indentations were performed to get a representative average and standard deviation. Hold period and acquisition rate during the tests were 1 s and 10 Hz, respectively.

To investigate the orientation effect on the mechanical properties a NanoTest Xtreme test setup from Micro Materials® with a diamond Berkovich tip was utilized in the work and the derived data were then combined with the EBSD results. A depth control mode was chosen instead of a load control mode to avoid localized large damage of the specimen due to large imprints, since imprints on the pores can be very large and interacted with neighboring indentations. The holding time at maximum load of 300 nm and rate of acquisition during the indentations were 10 s and 20 Hz, respectively. The indentation tests were carried out on a

surface area which was first characterized by EBSD. Due to the test limitation of the machine (maximum 400 impressions per test set), two individual areas were chosen to conduct the indentation mapping. The distance between the imprints was fixed to 5 μm in order to avoid interaction of the stress field of neighboring impressions. When establishing the dependence of indentation results on grain orientation, only indents which were inside the gains were taken into consideration. Indentations which were close to a grain boundary or located within a distance of 5 μm to pores were ignored to rule out associated effects that might lead to additional complexities in the correlation of mechanical data.

The fracture toughness assessment was conducted on an indentation rig (Micromet, Buehler LTD.) equipped with a diamond Vickers indenter. Loads of 0.5 N, 1 N, 3 N, 5 N and 10 N were applied to induce the cracks on the samples surface with sufficient crack length for the calculation. For each load 10 indentations were employed.

3.3.2 Bending tests

For brittle materials biaxial strength testing methods have been used for many years. Compared to the uniaxial testing, the biaxial testing has advantages like easy preparation of sample, typical availability of thin sheet material and testing the sample surface without the effect from edge defects [198]. The biaxial bending test is also an often used experiment to determine the global elastic modulus, fracture strength, reliability of the investigated materials. Moreover, combined with the stress rate, i.e., the loading rate of the test rig, the sensitivity to the subcritical crack growth can be investigated. A series of biaxial test methods have been developed [199]. Due to the boundary condition related to the sample size, the ball-on-three-ball (B3B) test and the ring-on-ring (ROR) test were employed in this work to test LATP:Si and LLZO material, respectively.

As the fracture reliability of the pure LATP material has been reported in the literature [12], and the B3B test is preferred for thin samples, the biaxial bending strength of LATP:Si pellets was investigated via the B3B test. In the B3B measurement, a rectangular plate (or a disc) is symmetrically supported by three balls at one plane and loaded by a fourth ball in the center of the opposite plane. The schematic experimental setup is illustrated in Fig 3.5 (a) and the details

of the relative position of the balls and the exampled disc sample can be seen in Fig 3.5 (b) [200]. The loading ball is in the same size of the supporting ball; where the supporting balls beneath the sample touch each other with a circle of radius R_a. Taking the thickness of the sample (t) into consideration, the radius of the circle (R_a) and sample (R) should be satisfied with the following relation: R_a/R in the range of 0.55 – 0.9 and t/R in the range of 0.05 – 0.6 [201], conditions that are satisfied in the current work.

More details about the test can be found elsewhere [200, 201]. In present case all four balls had a diameter of 5 mm and 13 specimens were cut into rectangular plate with size of 6.6 × 7.1 × 0.2 mm^3 for the test. A pre-load of 1 N was applied to hold the specimen between the four balls. Then the tests were conducted under displacement control at a rate of 0.01 mm/min and at room temperature, using a universal testing machine (Zwick Z010, Zwick/Roell, Ulm, Germany) with a load cell of 200 N. The load was increased until fracture occurred and the fracture load was used to calculate the maximum tensile biaxial stress in the specimen at the moment of fracture, see [200, 201].

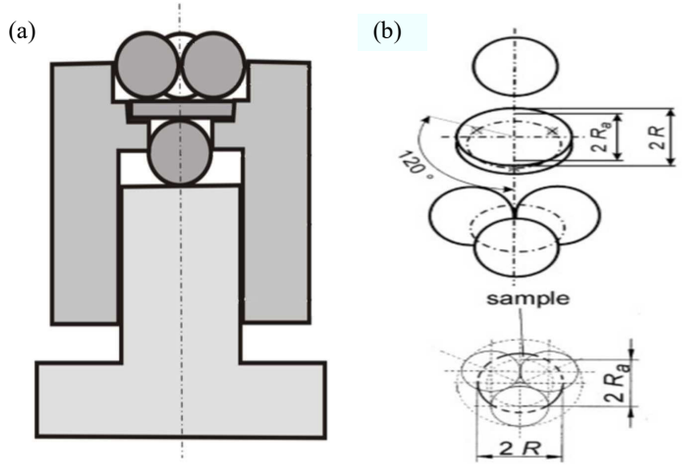

Figure 3.5 In (a): the experimental setup for ball-on-three-ball test, (b): isometric view of the relative positions of the sample to the balls [200].

According to the B3B test method [202], the maximum stress in the sample can be defined as the following equation:

$$\sigma_f = f\left(\frac{R_a}{R}, \frac{t}{R}, \vartheta\right) \cdot \frac{F}{t^2} \tag{3.7}$$

where F is the force, t the thickness of the sample and ϑ is the sample's Poisson's ratio. The dimensionless function f is approximated by:

$$f\left(\frac{R_a}{R}, \frac{t}{R}, \vartheta\right) = c_0 + \frac{c_1 + c_2\frac{t}{R} + c_3\left(\frac{t}{R}\right)^2 + c_4\left(\frac{t}{R}\right)^3}{1 + c_5\frac{t}{R}} \cdot \left(1 + c_6\frac{R_a}{R}\right) \tag{3.8}$$

where the parameters c_0 to c_6 are related to the Poisson's ratio as seen in Table 3.1.

Table 3.1 Dimensionless coefficient c_i used in Equation 3.8 at varied Poisson's ratios [202].

	ϑ = 0.2	ϑ = 0.25	ϑ = 0.3	ϑ = 0.35
c_0	-12.354	-14.671	-17.346	-20.859
c_1	15.549	17.988	20.774	24.403
c_2	489.2	567.22	622.62	716.41
c_3	-78.707	-80.945	-76.879	-76.16
c_4	52.216	53.486	50.383	49.615
c_5	36.554	36.01	33.736	32.555
c_6	0.082	0.0709	0.0613	0.0523

The global elastic modulus, fracture strength and reliability of LLZO material was evaluated by a ROR testing method. The experiments were performed using an electromechanical machine (INSTRON 1362) with a ±1000 N load cell (Lebow) and the displacement during the test was measured with the aid of a ceramic extension rod joined to a linear variable differential transformer (Solartron Metrology). The elastic modulus and maximum stress were be obtained as outlined in ASTM C1239-07 [203]. Schematic of the experimental setup and the working principle is shown in Fig. 3.6.

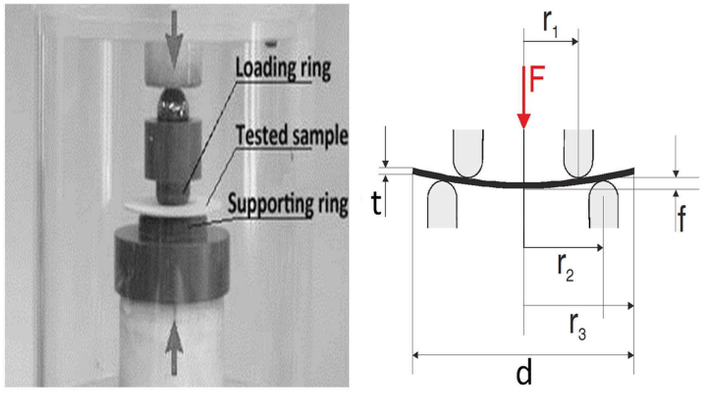

Figure 3.6 The ring-on-ring bending test set-up in IEK-2.

Table 3.2 Details of the ROR test on LLZO samples.

Sample	Loading Rate (N/min)	Number of Samples
LLZO	1	10
	10	11
	100	8

Tests were conducted at room temperature; the diameter of loading ring and supporting ring were 6.998 mm and 14.925 mm, respectively. More detailed descriptions of the procedures can be found in [204]. The number of samples and test conditions are given in Table 3.1. Following to the standard [205], the global elastic modulus is derived from the linear part of the load displacement curve (since unevenness of the specimen can result in a non-linearity at low loads):

$$E_{ROR} = \frac{3(1-v^2)\cdot r_1^2\cdot \Delta F}{2\pi\cdot \Delta f\cdot t^3}\cdot\left[\left(\frac{r_2}{r_1}\right)^2 - 1 - \ln\left(\frac{r_2}{r_1}\right) + \frac{1}{2}\left(\frac{1-\nu}{1+\nu}\right)\cdot\left(\frac{r_2^2-r_1^2}{r_3^2}\right)\cdot\left(\frac{r_2}{r_1}\right)^2\right] \quad (3.9)$$

where ΔF is the force difference and Δf the corresponding displacement change of the linear part, v the LLZO's Poisson's ratio, t the specimens' thickness, r_1, r_2 and r_3 are the radii of loading ring, supporting ring and specimen, respectively.

The maximum stress is constant within the tensile loaded surface inscribed by the loading ring, i.e.:

$$\sigma_f = \frac{3(1+\nu)F_f}{2\pi \cdot t^2} \cdot \left[\ln\left(\frac{r_2}{r_1}\right) + \left(\frac{1-\nu}{1+\nu}\right) \cdot \left(\frac{r_2^2 - r_1^2}{2r_3^2}\right)\right] \tag{3.10}$$

F_f is the fracture load.

Furthermore, in order to observe the fracture surfaces of the LATP:Si and LLZO samples a SEM or a confocal laser scanning microscope (CSLM: Keyence, VHX-5000) was used.

To characterize the reliability of the ceramic materials, the probability of failure P_f of the ceramic materials is analyzed using a two parameter Weibull statistics [155]:

$$P_f = 1 - \exp\left[-\left(\frac{\sigma}{\sigma_0}\right)^m\right] \tag{3.11}$$

In the equations, σ_0 is the characteristic strength, i.e. the stress for which the survival probability is 0.37; m is the Weibull modulus, which tells how rapidly the stress changes with probability, i.e. the variability of the fracture stresses.

3.3.3 Subcritical crack growth and lifetime prediction

As indicated in section 3.3.2, the subcritical crack growth of a material can be detected by correlating fracture stress to stress rate. The sensitivity regarding subcritical crack growth (SCG) was assessed in the current work using individual fracture stress data. The following equation was used to describe the correlation of fracture stresses and stress rate [155]:

$$\log \sigma_0 = \frac{1}{n+1} \log \dot{\sigma} + \log D \tag{3.12}$$

where D is a constant and n the SCG exponent. Since the slope deviation can't be related directly to the uncertainty of n, linear regression was performed for the logarithm of the fracture stress as

a function of the stress rate, and the highest and lowest n for SCG (best and worst case) were calculated via slope deviation together with slope uncertain (lower boundary and upper boundary), respectively [155].

An investigation of the subcritical crack growth sensitivity can be used to estimate the lifetime of brittle materials. Hence, failure probability along with time dependence and stress can be used to obtain a stress-probability-time (SPT) diagram [159]. Therefore, lifetime of the material under a static load can be forecasted, after the fracture stress generated via a dynamic load is transferred to the equivalent stress that causes breakage under static loading conditions. The equivalent stress under which failure will occur in 1 s (probability of ~ 63%, can be obtained from the characteristic strength using the equation [159, 160]:

$$\sigma_{1s} = \sigma_0 \left(\frac{\sigma_0}{\dot{\sigma}(n+1)}\right)^{1/n} \tag{3.13}$$

where σ_0 is the characteristic strength for a specific stress rate $\dot{\sigma}$. To obtain the characteristic strength for different times, the following equation can be used:

$$\frac{t_2}{t_1} = \left(\frac{\sigma_1}{\sigma_2}\right)^{1/n} \tag{3.14}$$

here σ_i is the characteristic strength for a time t_i (i = 1, 2).

To analyze the uncertainty of the lifetime prediction the errors in every procedure need to be considered. In this case, for straightforward lifetime prediction, the fracture stress from Weibull distribution with 95% confidence interval is introduced into the equation for SCG exponent, considering the best and worst case scenarios. The lifetime prediction was only done for the LLZO but not for LATP materials due to the material availability, i.e. the SCG and SPT analysis require a large amount of specimens.

3.3.4 Theoretical prediction of *E* and *H* (Vlassak-Nix model and Easy-slip model)

In order to investigate non-experimentally potential anisotropies in the mechanical properties of LATP, two theoretical models are adopted as a basis for later comparison with experimental results. These models permit prediction of modulus and hardness, respectively. The Vlassak-Nix model [164, 206] is used here to calculate the anisotropic elastic modulus related to the elastic constants of LATP single crystal, since this model has been successfully applied in predicting the elastic modulus of sapphire material, especially for the basal plane as well as in other two planes. Results matched with those reported in [207]. The 'easy-slip' model [208] is adopted to simulate the anisotropic hardness variation of LATP material related to the slip system. It was first introduced by the Csanadi et al. to calculate the hardness - orientation dependency of WC material and the analytical calculated results fitted very well with experimental results in [209].

The Vlassak-Nix model assumes that a rigid tip penetrates into an anisotropic elastic plane of a solid [164, 206]. In this model the Green's function for calculating the vertical displacement of the surface at a point load is adopted. A Rayleigh-Ritz approximation is applied to establish a force function which can form an elliptical contact area based on Green's function, with the assumption that the Laplacian operator in two-dimension of the surface is positive for the maximum displacement in the contact area and negative for the max displacement in the unloaded area. Another assumption is that a conical rigid indenter was introduced to maintain the same orientation and eccentricity of the contact zone for varied displacement. In order to simplify the model further, the contact area is set into a circular area, which leads to the calculation of the indentation modulus M as shown in equation (3.15). The h_0 here is the first item in the Fourier series representation of function $h(\theta)$ related to θ, which is demonstrated in equation (3.16). Here θ is the angle represented direction variation of point load in a specific surface ranged in $[0, \pi]$. The α_i is the direction cosines of the angle between the load direction and the crystal coordinate system axes. Equation (3.17) and equation (3.18) are the expansion form of Barnett function B_{km}^{-1} in equation (3.16) and that of $(\mathrm{ab})_{jk}$ in equation (3.17), respectively. In equation (3.17) one right-hand Cartesian coordinate ($\vec{m}$, $\vec{n}$, $\vec{t}$) is built where the $\vec{t}$ axis was vertical to the load direction, in which φ is the angle between the vector $\vec{m}$ and one

fixed vector in the ($\vec{m}$, $\vec{n}$) plane. The C_{ijkm} in equation (3.18) contains the elastic parameters of the anisotropic material based on the elastic constants of the material. The transition of the parameter C_{ijkm} from the elastic constants C_{pq} follows the regulation: the tensors ij (or km) reflected to the tensor p (or q) with the relation of 11 → 1, 22 → 2, 33 → 3, 23 and 32 → 4, 13 and 31 → 5, 21 and 12 → 6.

$$M = \frac{1}{\pi h_0} \tag{3.15}$$

$$h(\theta) = \frac{1}{8\pi^2}(\alpha_k B_{km}^{-1} \alpha_m) \tag{3.16}$$

$$B_{js}(\mathbf{t}) = B_{sj}(\boldsymbol{t}) = \frac{1}{8\pi^2}\int_0^{2\pi}\{(\mathbf{mm})_{js} - (\mathbf{mn})_{jk}(\mathbf{nn})_{kr}{}^{-1}(\mathbf{nm})_{rs}\}\, d\varphi \tag{3.17}$$

$$(\mathbf{ab})_{jk} = a_i C_{ijkm} b_m \tag{3.18}$$

$$C_{pq} = \begin{pmatrix} 226.0 & 86.7 & 43.9 & 7.9 & 0.0 & 0.0 \\ 86.7 & 226.0 & 43.9 & -7.9 & 0.0 & 0.0 \\ 43.9 & 43.9 & 116.3 & 0.0 & 0.0 & 0.0 \\ 7.9 & -7.9 & 0.0 & 48.6 & 0.0 & 0.0 \\ 0.0 & 0.0 & 0.0 & 0.0 & 48.6 & 7.9 \\ 0.0 & 0.0 & 0.0 & 0.0 & 7.9 & 49.6 \end{pmatrix} \tag{3.19}$$

By now, there's no elastic constants results reported for the $Li_{1+x}Al_xTi_{2-x}(PO_4)_3$ material. Since the structure of $Li_{1+x}Al_xTi_{2-x}(PO_4)_3$ material is the same as that of $LiTi_2(PO_4)_3$ and the substitution of Al^{3+} into the lattice structure yields no obvious contribution to the lattice parameter compared with that of $a^*=b^*=0.8535$ nm, $c^*=2.0883$ nm as reported in [210]. The elastic constants of $LiTi_2(PO_4)_3$ with the unit GPa as given in Equation (3.19), which were calculated via ab initio method by Deng et al. [166], are employed in the Vlassak-Nix model. Taking the symmetry of hexagonal structure into consideration, as illustrated in Fig. 1 in the Vlassak-Nix model, the angle Φ from basal plane to the perpendicular direction with 1° per step, and some specific angles of $\varphi 2$ in the basal plane are adopted to calculate the orientation dependency of the indentation modulus.

The "easy-slip" model, on the other side, which is adopted here to predict the hardness variation related to the orientation of the anisotropic material, is based on one principal hypothesis that the stress distribution is confined in the indentation area which is uniformed, i.e., the stress component surrounding the indenter is compressive and vertical to the indenter profile

[208, 209]. This model contains several assumptions and a schematic is shown in Fig. 3.7 (a) as expressed in equation (3.20). First is that the conical rigid indenter with a semi-angle γ of 65° is introduced into the model to simplify the calculation and also reaches a consensus with the Vlassak-Nix model. Additionally, friction during indentation is not considered. The second assumption is that just one dislocation slip is considered as the plastic deformation fraction is small. The slip can only occur when the shear stress reaches a critical value for a specific direction, which results in the name of "easy-slip". Here the Schmidt factor for calculating the normal stress, as illustrated in Fig. 3.7 (b), is introduced in equation (3.21), assuming that the critical resolved shear stress is a constant, and the calculation of normal stress follows equation (3.22).

The third assumption is about the slip systems of the LATP material, which is different in this work compared to that of WC reported in the Csanadi et al.'s work [208]. To the best of our knowledge, no investigations have been reported on the slip systems of the LATP or LTP materials. For the materials with $R\bar{3}c$ crystal system like LATP, two kinds of crystal deformations can come up simultaneously, which are slipping and twinning [211, 212]. It has been confirmed that for the rhombohedral crystal structure with computed hexagonal lattice parameter ratio of $c^*/a^* > 1.633$, the slide systems are $\{0001\}\langle 11\bar{2}0\rangle$ in basal plane and $\{11\bar{2}0\}\langle 1\bar{1}00\rangle$ in prismatic planes, whereas the slip in pyramidal plane is out of consideration since this type of slip can be unidirectional [213, 214].

Thus, in total 6 slip systems are considered in the easy slip model with $\overrightarrow{n_i}$ as the normal vector for the slip plane and $\overrightarrow{v_{ij}}$ as the slip direction vector as illustrated in Fig. 3.7 (c): $\overrightarrow{n_0}$ = (0001): $\overrightarrow{v_{01}}$ = $[11\bar{2}0]$, $\overrightarrow{v_{02}}$ = $[2\bar{1}\bar{1}0]$, $\overrightarrow{v_{03}}$ = $[\bar{1}2\bar{1}0]$, $\overrightarrow{n_1}$== $(11\bar{2}0)$: $\overrightarrow{v_{11}}$ = $[1\bar{1}00]$, $\overrightarrow{n_2}$ = $(\bar{1}2\bar{1}0)$: $\overrightarrow{v_{21}}$ = $[10\bar{1}0]$, $\overrightarrow{n_3}$ = $(2\bar{1}\bar{1}0)$: $\overrightarrow{v_{31}}$ = $[01\bar{1}0]$. The vectors $\overrightarrow{n_i}$ and $\overrightarrow{v_{ij}}$ should be normalized during calculation. An improvement of the original model is made according to [209], i.e. that the average of the maximum Schmid factor by the surrounding of indenter at the specific rotation angle Φ is considered rather than the maximum Schmid factor directly as shown in equation (3.23). With these entire mentioned hypotheses, the relation between hardness and the orientation of the LATP material can be expressed as a ratio of hardness at specific plane to hardness at prismatic

plane as demonstrated in equation (3.24), which is equal to the inverse ratio of the corresponding average maximum Schmid factor.

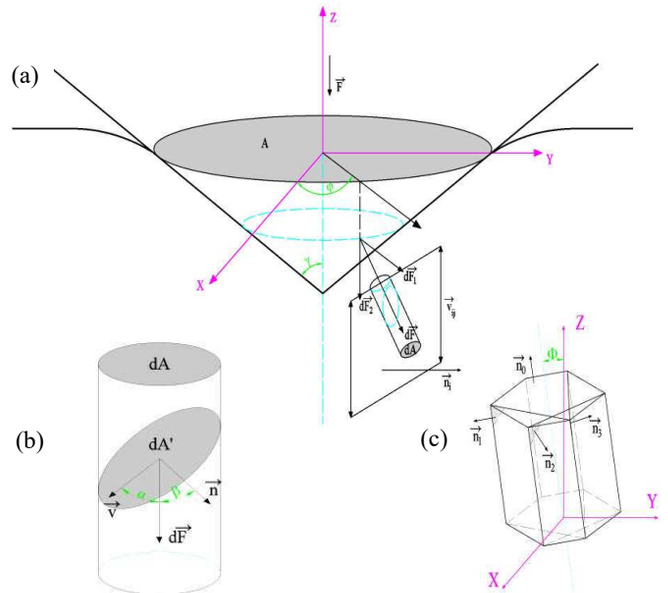

Figure 3.7 A schematic of the resolved point load in (a), Schmid factor derivation for a single slip system in (b) and the rotated slip systems in (c).

$$m(\varphi)_{avg.max,\varphi}(\Phi) = \frac{1}{2\pi}\int_0^{2\pi} max_{i,j}\left(m_{i,j}(\Phi,\varphi)\right)d\varphi \tag{3.20}$$

$$\frac{H(\Phi)}{H_{prismatic}} = \frac{H(\Phi)}{H(\Phi=90°)} = \frac{m_{avg.max,\varphi}(\Phi=90°,\varphi)}{m_{avg.max,\varphi}(\Phi,\varphi)} \tag{3.21}$$

$$\sigma = \left(\frac{\tau}{m(\varphi)}\right)_{min} = \frac{\tau_{CRSS}}{(m(\varphi))_{avg.max,\,\varphi}} \tag{3.22}$$

$$m(\varphi)_{avg.max,\varphi}(\Phi) = \frac{1}{2\pi}\int_0^{2\pi} max_{i,j}\left(m_{i,j}(\Phi,\varphi)\right)d\varphi \tag{3.23}$$

$$\frac{H(\Phi)}{H_{prismatic}} = \frac{H(\Phi)}{H(\Phi=90°)} = \frac{m_{avg.max,\varphi}(\Phi=90°,\varphi)}{m_{avg.max,\varphi}(\Phi,\varphi)} \tag{3.24}$$

4. Results and Discussion

In this part, the results on the mechanical properties of solid electrolytes are presented and discussed in four separated sections. The first section focuses on $Li_{1.3}Al_{0.3}Ti_{1.7}(PO_4)_3$ (LATP) sintered at different temperatures. The influence of sintering temperature on the LATPs' purity, porosity, lattice parameter, and electrical properties is investigated and related to the mechanical properties in particular elastic modulus, hardness and fracture toughness.

In the second section, optimized LATP samples sintered at 1100 °C, which possessed high elastic modulus, hardness and ionic conductivity, are selected to investigate orientational effects on elastic modulus and hardness via nanoindentation method combined with EBSD analysis. Here, the effect of rotational angle Φ from basal plane to prismatic plane and angle $\varphi 2$ between two prismatic $(10\bar{1}0)$ type planes is investigated. Calculations based on the Vlassak-Nix and the easy-slip models are adopted to verify the anisotropic mechanical properties.

The third section concentrates on fracture reliability results of two kinds of electrolytes. Aim is here to assess the fracture reliability of $Li_{1.5}Al_{0.5}Ti_{1.5}(PO_4)_3$ mixed with SiO_2 (LATP:Si)and $Li_7La_3Zr_2O_{12}$ (LLZO), which is a composition selected regarding design and promotion towards practical application, in particular the optimized tape casting manufacturing [215]. As the fracture strength results of pure LATP have been reported by Jackman et al. [12], only the tape casted LATP:Si was tested to investigate to assess if the mechanical properties are affected by the SiO_2 binder and doping. In addition, the fracture reliability of the alternative material LLZO was studied in this work, elastic modulus, hardness and fracture toughness were not studied here since they have been reported [13, 14]. Complementarily, room-temperature subcritical crack growth effects were evaluated on the basis of loading rate-dependency of derived fracture stresses in order to assess potential subcritical crack propagation issues of LLZO components.

Since the electrolytes in all-solid-state lithium batteries are operating under cyclic voltage condition that are associated with chemical expansion effects, it is crucial to understand the mechanical stability of electrolytes under such conditions. Hence, in the fourth section,

exemplified for $Li_{0.350}La_{0.557}TiO_3$ (LLTO), a material being close to application [15-17], voltage effects on mechanical properties were studied.

Hence, overall, the goals are mechanical property characterization of the electrolytes, which includes effects of sintering temperature, crystal orientation, as well as the fracture reliability and charge state effect considering practical application relevant conditions. The interpretation of the derived data can aid materials' optimization and understanding of degradation and operational related effects.

4.1 $Li_{1.3}Al_{0.3}Ti_{1.7}(PO_4)_3$: Effect of sintering temperature[1]

This section presents the investigation on the LATP sintered at different temperatures (950, 1000, 1050, 1100 °C). Impedance tests were carried out and as main focus of the work elastic modulus, hardness and fracture toughness of LATP samples were determined.

4.1.1 Composition, microstructure and conductivity

First, LATP samples after sintering were tested via XRD to analyze the phase structure, the individual specimens' name includes the maximum sintering temperature, further details on specimens' production and sintering conditions can be found in section 3.1.1. Via Rietveld refinement of the XRD data, the lattice parameters of the samples were obtained and are presented in Table 4.1. It can be seen that the LATP samples sintered at different temperatures are composed of the main phase LATP in rhombohedral structure and only some minor amount of secondary phase. With increase of the sintering temperature, the amount of the secondary phase also increased. The secondary phase was probably a result of Li^+ evaporation from LATP during high temperature sintering, since as Li^+ evaporated the dopant of Al^+ might exceed the solubility limit then the precipitate formatted [216, 217]. From the lattice parameter it can be seen that the a^* and b^* are similar for the four samples, whereas the c^* parameter revealed a trend towards decreasing values as the sintering temperature increased. Overall, the lattice parameter results are consistent with those reported by Swati et al. [218], where $a^* = b^* = 0.8512$ nm, $c^* = 2.0878$ nm.

[1] Section content published: G. Yan et al.: Ceramics International (2019), 45, 14697-14703.

Table 4.1 Lattice parameter of as-sintered LATP pellets from Rietveld refinement.

Samples	**Lattice parameters**							
	Space group	*a** (nm)	*b** (nm)	*c** (nm)	*α*	*β*	*γ*	Secondary phase
LATP 950 °C	R-3c (167)	0.85503	0.85503	2.09859	90°	90°	120°	~ 3.8 wt%
LATP 1000 °C		0.85526	0.85526	2.09702	90°	90°	120°	~ 7.5 wt%
LATP 1050 °C		0.85504	0.85504	2.09777	90°	90°	120°	~ 8.9 wt%
LATP 1100 °C		0.85523	0.85523	2.09652	90°	90°	120°	~ 13.3 wt%

The microstructures of the materials sintered at different temperatures are illustrated in Fig. 4.1. The EDS result of LATP sintered at 1100 °C is also shown in Fig. 4.1 to reveal the distribution of secondary phase $AlPO_4$. All LATP samples possess a porous structure. The grain size of the LATP were 9.5 ± 5.2, 9.7 ± 5.1, 10.5 ± 6.0 and 12.1 ± 5.9 μm for the sintering temperatures of 950, 1000, 1050 and 1100 °C, respectively. Hence, the average grain size of the samples increased slightly with rising sintering temperature, being in good agreement with results reported by Duluard et al. [219]. The pores were spherical inside the grains and irregular at the grain boundaries. In addition, the amount of the pores inside the grains decreased as the sintering temperature was increased. As exemplified for the specimen sintered at 1100 °C in Fig. 4.1(e), the elements O and P were distributed uniformly in the sample, whereas the Al-rich regions (no titanium) can be assigned to the $AlPO_4$ phase, which agglomerated. The $AlPO_4$ phase was present in both grain boundaries and inside grains, which is in good accordance with results reported by Yu et al. [186].

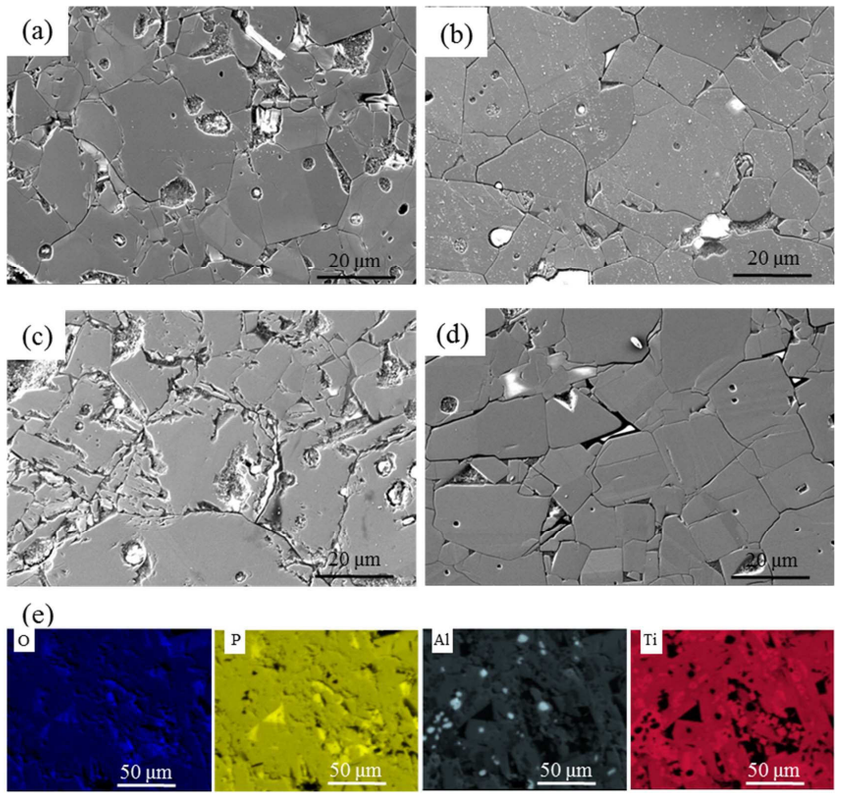

Figure 4.1 SEM and EDX results of LATP. SEM images of LATP samples sintered at different temperatures: (a) 950 °C, (b) 1000 °C, (c) 1050 °C and (d) 1100 °C. (e) element mapping of LATP sintered at 1100 °C.

Three different methods for porosity measuring were adopted and compared to acquire the relative density of the LATP samples, since the porosity can affect the mechanical properties of the materials like the elastic modulus, hardness and fracture toughness [220, 221]. Porosities of LATP based on Archimedes' principle were measured in water (the data referred to [186]). The geometric (physical) measurement results are representative of the bulk density of the materials. Besides, the densities from the image analysis were obtained from the Fig. 4.1, which were rather dense areas of the samples. The Archimedes' porosity is much lower than that from other methods since the open porosity could be fully filled in the water, while the relative density of

image analysis is a little bit higher than that of physical measurement, which might be attributed to the chosen rather dense area. It's not the scope to analyze a lot of microstructure pictures, for example a detailed analysis of pore effects is presented in the work of Ying et al. [222]. According to the results in Table 4.2 it can be concluded that as the sintering temperature increased, the porosity of the samples decreased. The lower porosity of the samples at higher sintering temperatures was expected due to the extrusion of bubbles [223].

Table 4.2 Comparison of the relative density of LATP samples for the three methods.

Sample	Archimedes' method	Physical measurement	Image analysis
LATP 950 °C	94.52%	85.7 ± 1.7 %	86.6 ± 0.5 %
LATP 1000 °C	95.48%	87.2 ± 0.9 %	87.3 ± 0.3 %
LATP 1050 °C	96.10%	87.4 ± 0.9 %	90.9 ± 0.7 %
LATP 1100 °C	96.72%	87.9 ± 1.3 %	92.8 ± 0.6 %

Regarding conductivity, since the layer thickness and the contact between the LATP and gold layer can influence the concentration gradients during ion transport, it was more precise to compare the overall conductivity of LATP samples based on a specific geometry. The ionic conductivity results based on an equivalent circuit obtained at 25 °C are shown in Fig. 4.2, where the impedance spectroscopy curves are given as inserted. As shown in the figure, the sintering temperature increase led to a conductivity increase from 8.69×10^{-5} to 1.83×10^{-4} S/cm, i.e. the specimen sintered at 1100 °C had the highest conductivity. Hence, it can be recognized that the sintering temperature indeed affects the conductivity, an effect that might be associated with the difference in porosity, morphology of grains, grain size and secondary phase content. As reported by Key et al. [216], higher density and larger grain size can decrease the grain boundary impedance, while a secondary phase ($AlPO_4$) at the grain boundary can limit the total conductivity.

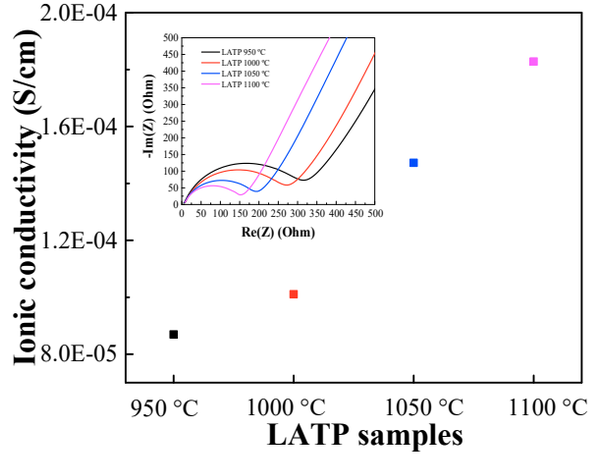

Figure 4.2 Impedance spectroscopy of LATP sintered at different temperatures.

4.1.2 Mechanical properties

The elastic moduli of the LATP samples sintered at different temperatures as a function of load are shown in Fig. 4.3. It can be seen that for all samples the elastic modulus decreases with increasing indentation load. An exponential curve was used in the current work as guide to the eye to emphasis that the elastic modulus decreases steadily and rather strongly in the lower load range and then stabilizes at higher loads. Note that, the curves are only for a guide for the eye and do not imply a fitting with a physical meaning.

The decrease of *E* with load (corresponding to depth and hence increased deformed volume) can be related to a porosity effect, i.e. as the load increases the effectively deformed zone of the indentation enlarges leading then to a response of dense material and pores. At load of 30 mN, the elastic modulus of LATP samples sintered at different temperature was 118 ± 5, 120 ± 6, 121 ±7 and 127 ± 10 GPa, respectively, being basically representative of the property of the dense material.

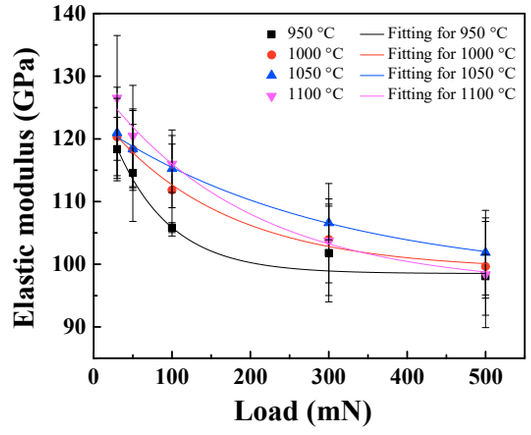

Figure 4.3 Elastic modulus of LATP samples as a function of load.

According to the graphical representation of the data, the elastic modulus of LATP sintered at 950 °C was lower than all others' and overall, the elastic modulus slightly increased as the sintering temperature rose. This can be ascribed to the lower porosity at higher sintering temperature, since the pores can decrease the elastic modulus of a material [224]. In addition, the smaller lattice parameter c^* can also be a factor for the higher E values for higher sintering temperatures. It was already shown for other materials that, when the grain size was in a specific submicron range, the mean elastic modulus increased with a decrease of the lattice parameter [225, 226]. As the grain size was in the same range for all materials tested in the current work, a pronounced grain size is unlikely as cause of variation in elastic modulus of the LATP.

For comparison, the elastic modulus of $AlPO_4$ was around 77 GPa [227, 228], which due to its existence as second phase might influence the elastic modulus of LATP, especially leading to differences when sintered at high temperatures. However, considering the potential influence of the lattice parameter and secondary phase $AlPO_4$, the experimental results indicated that the lattice parameter dominates leading to an increase of elastic modulus over any potential decrease of elastic modulus due to the secondary phase as the sintering temperature was increased (see also Table 4.1).

The hardness of the LATP sintered at different temperatures was also tested at different loads via the indentation method. The results are shown in Fig. 4.4. At a low load of 30 mN, the hardness of LATP sintered at different temperatures is 9.3 ± 0.3, 9.6 ± 0.7, 9.6 ± 0.4 and 9.8 ± 0.8 GPa, respectively. As can be seen in Fig. 4, the hardness of LATP sintered at 950 °C is the lowest, whereas those of the other three samples were similar. As a guide for the eye the exponential curves were used to indicate that the hardness decreased continuously in the lower load range and then stabilized. Again these curves here are only guidance guide to the eye and they don't imply any physical meaning of the fitting.

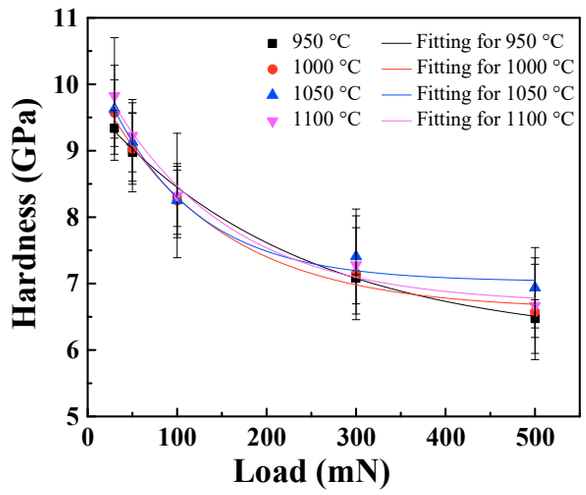

Figure 4.4 Hardness of LATP samples as a function of load.

The decrease of this property with increasing load can also be associated with the porosity effect, since also the plastic zone increases at higher the loads. Overall, the hardness of materials is mainly controlled by four features. The first is the porosity of the material. The pores acted as stress concentrator and reduced the material's strength by contracting the cross-section where the load was applied [229]. The porosity of the LATP samples decreases with increasing sintering temperature, which indicates that the hardness of the LATP should be higher at higher sintering temperatures, however, similar as in case of elastic modulus this should be mainly an effect at

higher loads. Second is the lattice parameter of the material. It was reported that the hardness of material can be correlated to the material's shear and bulk modulus [230, 231]. The shear modulus and bulk modulus are also key parameters related to the yield strength which increases as the lattice parameter decreases. Thus, the smaller lattice parameter c^* can be a factor for the higher H values for LATP sintered in higher temperature, especially at lower loads where a pronounced effect of the pores cannot be expected. Thirdly, the grain size of the samples, i.e. it has been reported that as the grain size increases the hardness decreased [224, 232]. In the current work, the grain size of the four samples was in a similar range. The fourth is the difference in the type and amount of second phase. The amount of the second phase of LATP increased as the sintering temperature rose. The secondary phase $AlPO_4$ was partially distributed inside the grain. As reported the Mohs hardness of $AlPO_4$ was around 6.5 [233] and the microhardness was 3.5 - 5.5 GPa [234], the LATP sintered in high temperature with higher amount of secondary phases should yield hence a lower hardness at high load due to the large effective zone. Although the secondary phase $AlPO_4$ can lower the hardness, the decreasing of porosity and lattice parameter had contrary effects on LATP's hardness, which resulted that at low load the hardness of LATP sintered at 1100 °C was the highest. Thus, increasing the density of the LATP during sintering can enhance the hardness, which might be a benefit for the application.

In order to characterize the type of bonding, the ratio of the hardness to the shear modulus, G ($G = E/2(1 + \nu)$), was used as a parameter. Apparently the ratio H/G of 0.1, H/G of 0.01 and H/G of 0.001 represent the covalent, ionic and metallic bonding, respectively [183, 235]. The Poisson's ratio of 0.25 of LATP is adopted in this work [166], so the elastic modulus and hardness can be used for determining the dominant bonding type of LATP materials. The H/G value was calculated for LATP sintered at different temperatures as being 0.1. This suggested that the LATP samples are mainly governed by a covalent bonding type, which is in good agreement with that reported for LATP (~0.16) [236] and other perovskite and garnet materials [236], where the H/G for LLZO was ~0.11 and the H/G for LLTO was ~0.12.

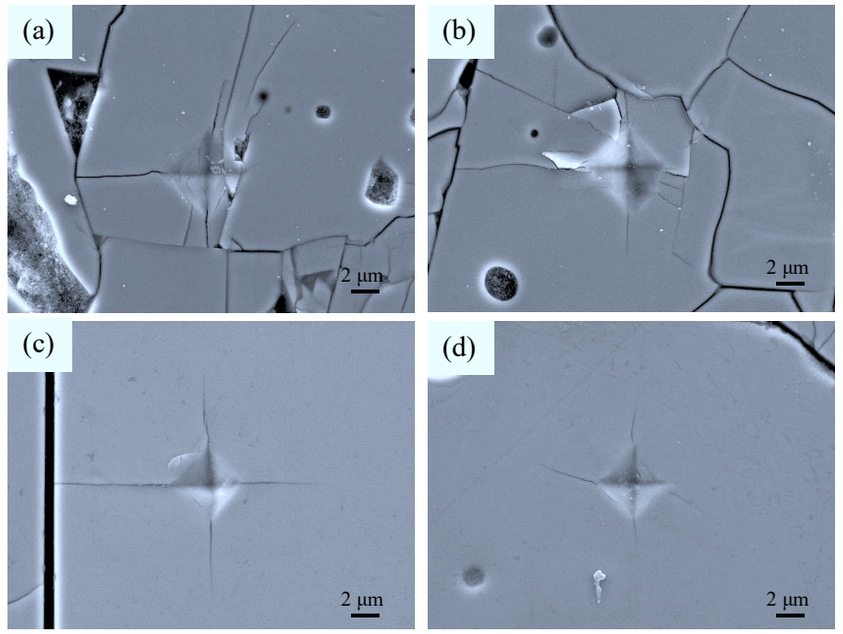

Figure 4.5 Typical SEM images of indents on LATP samples, (a), (b), (c) and (d) represent LATP sintered in 950, 1000, 1050 and 1100 °C, respectively.

Fracture toughness was derived in the current work from the length of cracks after indentation. As examples Fig. 4.5 shows typical Vickers imprints after loading with 0.5 N for the LATP samples sintered at different temperatures. For all specimens the indentations at even higher load led to crushed material and no crack propagation effects could be observed. Thus the imprints for a load with 0.5 N were only considered in the current work. For the LATP sintered at 950 and 1000 °C, the cracks emanated from the corners of the indentations and got stopped at grain boundaries and the material was partially squeezed out in the indentation area. The indentations on LATP sintered at 1050 and 1100 °C left material with remaining global structure integrity and also some well-defined long straight cracks starting from the corners could be used for fracture toughness determination. Note, only regular straight cracks were considered in the determination of the fracture toughness, cracks that showed interaction with grain boundaries or that extended not in a straight line from the indentation diagonal were not considered.

As mentioned in the experimental part, for calculating the fracture toughness the elastic modulus, hardness and the diagonal length of the indentation imprint as well as the crack length have to be characterized. With the load of 0.5 N the indentations on the LATP 950 °C and 1000 °C were slightly crushed, see Fig 4.5 (a) and Fig 4.5 (b). Therefore, it was not possible to provide fracture toughness values for the samples sintered at 950 °C and 1000 °C. Furthermore, as mentioned before, for the material sintered at higher temperature cracks intersecting with a grain boundary, see Fig. 4.5 (c), were not considered, to rule out the effect of grain boundaries.

The fracture toughness values of the LATP sintered at different temperatures are given in Table 4.3. As mentioned, since the crack lengths of LATP sintered at lower temperatures were difficult to assess due to multiple secondary cracks and crack-grain boundary interactions, the fracture toughness was not calculated. The derived K_{IC} values of LATP sintered at 1050 °C and 1100 °C were 1.4 ± 0.2 and 1.6 ± 0.2 MPa·m$^{1/2}$, respectively. The ratio of crack length to diagonal length of the indentation (l/a) was in the range of ((3.1 - 4.4)/(2.4 - 2.8)) and ((4.1 - 5.8)/(2.5 - 2.8)) for LATP sintered at 1050 °C and 1100 °C, respectively, verifying the validity of the used relationship to derive the data.

Table 4.3 Fracture toughness of LATP samples sintered at different temperatures.

Sintering temperature	950 °C	1000 °C	1050 °C	1100 °C
Fracture toughness (MPa·m$^{1/2}$)	-	-	1.4 ± 0.2	1.6 ± 0.2

In order to check the effect of crack model, the equation for Palmqvist cracks [151] was also used, although not justified by the crack length ratio, yielding for example for the K_{IC} of LATP 1100 °C at 0.5 N 1.75 ± 0.3 MPa·m$^{1/2}$ which is close to the 1.6 ± 0.2 MPa·m$^{1/2}$ for the radial mode, hence verifying that the result is rather insensitive of the used crack mode model, and is as expected that in good agreement with the LATP's and other electrolytes' K_{IC} results (1.1 to 1.24 MPa·m$^{1/2}$) published [12, 17, 177].

Obviously, the results verify also that the LATP materials are brittle. With application of the external load, brittle materials can show catastrophic failure owing to the low intrinsic fracture toughness (typically in cases of up to 3 MPa·m$^{1/2}$) [237].

It can be seen that the fracture toughness of LATP sintered at 1100 °C is slightly higher than that of the one sintered at 1050 °C. Since the indentations and cracks for LATP sintered at 1050 °C and 1100 °C are mainly located inside one grain (at least for the visible surface), the fracture toughness is probably not affected much by the grain size or the grain boundary. Nevertheless, a possible factor of the microstructure influencing the K_{IC} could be the porosity, since pores are typically located inside grains. Generally, materials have a higher fracture toughness for lower porosities [238]. As seen from Fig. 4.1, the amount of pores inside the grains of LATP sintered 1100 °C appears to be less than that in case of the materials sintered at 1050 °C. However, since pore – crack interactions were not visible after the indentation impression and porosity was rather low, main reason for the difference can also be related to differences in fracture energy that is on one side directly linked to the fracture toughness and on the other side directly linked to the bonding strength and hence, similar as the elastic modulus, to the lattice parameter.

Elastic modulus, hardness and fracture toughness of LATP obtained in the current work can be compared also with data reported elsewhere and also those of some other solid electrolytes. It has been reported that the elastic properties of $LiTi_2(PO_4)_3$ type electrolytes calculated from first principle is 139.0 – 152.5 GPa [166], which is in good agreement with the data reported here, but higher than that reported by Jackman et al. that the elastic modulus of LATP is in the range of 81 – 115 GPa [12].

Compared with the work of Jackman et al.[12], the hardness derived here is higher than that of LATP (7.1 ± 0.4 GPa) reported in this work. The elastic modulus and hardness difference this work and the work of Jackman et al.[12] can be attributed to the test method, since in Jackman et al.'s work the biaxial and flexural tests were adopted which means the effectively deformed zone was way larger than the indentation test adopted here. As shown in the above results the higher effectively deformed zone the lower E and H values.

The fracture toughness values derived here are in good agreement with the reported value of 1.1 ± 0.3 MPa·m$^{1/2}$, considering experimental uncertainties. For the garnet-type electrolyte $Li_{6.19}Al_{0.27}La_3Zr_2O_{12}$ with 97% density, 5 µm grain size, an elastic modulus of 150 ± 0.4 GPa has been reported [177]. For perovskite-type electrode $Li_{0.33}La_{0.57}TiO_{12}$ with 99% density, 1.5-13 µm grain size, the reported elastic moduli were in the range of 143 to 203 GPa [17]. Hence, the currently tested LATP materials have a lower elastic modulus than $Li_{6.19}Al_{0.27}La_3Zr_2O_{12}$ and $Li_{0.33}La_{0.57}TiO_{12}$. Compared with literature, the current LATP materials possess a similar hardness as garnet-type electrolyte $Li_{6.19}Al_{0.27}La_3Zr_2O_{12}$ with 97% density, 5 µm grain size [177] (9.1 ± 0.5 GPa) and perovskite-type electrode $Li_{0.33}La_{0.57}TiO_{12}$ with 99% density, 1.5 - 13 µm grain size [17] (8.1 to 8.4 GPa). In current literature [17, 177], the K_{IC} of garnet-type electrolyte $Li_{6.19}Al_{0.27}La_3Zr_2O_{12}$ is reported to be 1.25 ± 0.32 MPa·m$^{1/2}$ and the K_{IC} of perovskite-type electrode $Li_{0.33}La_{0.57}TiO_{12}$ as 1.15 to 1.24 MPa·m$^{1/2}$ [17, 177]. This indicates that the fracture toughness of LATP sintered at 1100 °C is higher than that of $Li_{6.19}Al_{0.27}La_3Zr_2O_{12}$ and $Li_{0.33}La_{0.57}TiO_{12}$.

In the present work it is shown that the conductivity at 25 °C and the mechanical properties, i.e. elastic modulus, hardness and fracture toughness, of LATP sintered at 1100 °C are higher than that for the material sintered at lower temperatures. This appears to be promising for the application of LATP materials since good ion-conductivity behavior and mechanical properties can be obtained simultaneously. Yu et al. [186] found that, to reduce the resistance of LATP material, the secondary phase ($AlPO_4$) content and microstructure needed to be adjusted: less secondary phase, larger grain size and denser microstructure. Since the elastic modulus and hardness of $AlPO_4$ are both lower than that of LATP materials, it might be speculated that lowering the content of $AlPO_4$ can further improve the mechanical properties of LATP. In addition, porosity also influences the mechanical properties significantly, especially when considering the macroscopic elastic modulus and the fracture stress as global property.

4.1.3 Summary

The mechanical properties and ionic conductivity at room temperature of LATP sintered at different temperatures (950, 1000, 1050, 1100 °C) were characterized in this work. The grain sizes of the four samples were similar, whereas the amount of secondary phase and density

increased as sintering temperature rose. LATP sintered at 1100 °C showed the highest conductivity, 1.83×10^{-4} S/cm, compared to the others.

The elastic moduli of the LATP samples were 118 ± 5, 120 ± 6, 121 ±7 and 127 ± 10 GPa, respectively, in dependence on increasing sintering temperatures. The hardness values of LATP sintered at different temperatures were 9.3 ± 0.3, 9.6 ± 0.7, 9.6 ± 0.4 and 9.8 ± 0.8 GPa, respectively. The higher elastic modulus at low load of LATP sintered at higher temperature was related to the increase of lattice parameter c*. The decreasing of the elastic modulus and hardness with the increasing of load was related mainly to an increasing porosity effect. The fracture toughness, K_{IC}, of LATP sintered at 1050 and 1100 °C were characterized to be 1.4 ± 0.2 and 1.6 ± 0.2 MPa·$m^{1/2}$, respectively. The value for the LATP sintered at a higher temperature was slightly higher probably again due to the lattice parameter. Obviously to confirm the effect of the porosity on the mechanical measurements assessment of the global properties via use of higher indentation loads or optional impulse excitation or bending tests would be an asset. However, main aim should be to obtain materials in the densest possible state, rendering values obtained at low loads rather important. This part of the work provides a basis for further optimization of LATP materials to gain both good mechanical properties and conductivity by lowering the secondary phase content and densifying the microstructure of the material.

4.2 $Li_{1.3}Al_{0.3}Ti_{1.7}(PO_4)_3$: Orientation effect [2]

The micro-battery, one application of the solid state batteries, requires a solid electrolyte of small size, which feasibly leads to an anisotropy effect of the material. The LATP sintered at 1100 °C (in this section LATP 1100 °C is shorted as LATP) as discussed in section 4.1 is selected to investigate potentially anisotropic mechanical properties. The commonly used nanoindentation test is combined with EBSD technique to investigate the elastic modulus and hardness of the LATP material correlated to the crystal orientation. Vlassak-Nix model and the easy-slip model are adopted to theoretically predict the anisotropic mechanical properties.

[2] Section content published: G Yan et al. J. Power Sources (2019), 437, 226940.

4.2.1 Composition, microstructure and conductivity

The composition, microstructure and conductivity of the LATP characterized in the current section are the same as that of the LATP 1100 °C reported in section 4.1.1. In order to aid discussion and interpretation, the composition, microstructure and conductivity results of the LATP (LATP 1100 °C) are verified again along with the crystal structure information aiding analyses of the orientation effect on the mechanical properties of LATP.

Microstructural images of the LATP sample at different magnifications are displayed in Fig. 4.6, further details on specimen production and sintering conditions can be found in section 3.1.1. It be seen from Fig. 4.6 (a) that the LATP has some pores, which are homogeneously distributed. The microstructure at a higher magnification is shown in Fig. 4.6 (b), from which the grain size of LATP has been derived via the software "AnalySIS pro" as 12.1 ± 5.9 μm. The pores are located both in grain boundaries and inside grains, where the former are irregular and the latter are rather round. The spherical pores inside the grains can be ascribed to the hydrostatic pressure of air, which was preserved in the grown grains during pre-annealing [239].

The Archimedes' method was used here to characterize the porosity of the LATP, hence open pores did not enter the porosity calculation. The relative density of the LATP sample calculated by the ratio of bulk density to theoretical density of 2.947 g/cm^3 [12] is 96.7%. It is well known that the porosity can decrease the mechanical properties of a material like elastic modulus and hardness [220, 221], also already stated before. However, in this part of the work the indentation test was conducted in a small local region of single grains so that effects of pores on the obtained properties can be ignored. Furthermore, the grain boundaries, as shown in Fig. 4.6 (b), are very distinct, which was helpful in localizing the corresponding indentations in the EBSD mapping and eliminating respective data.

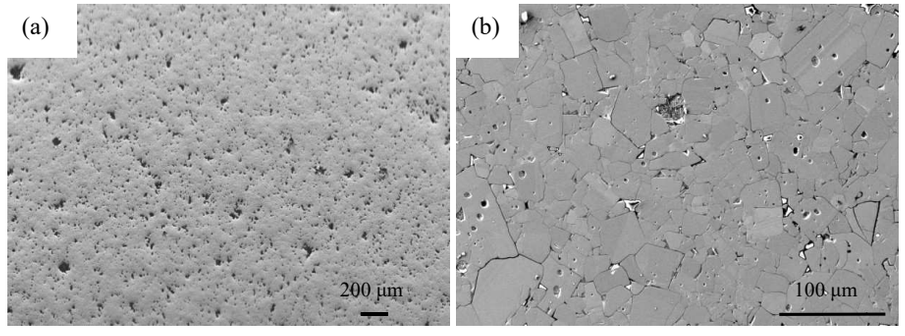

Figure 4.6 Typical SEM image of LATP sample in different magnification.

For confirmation, again one as-sintered LATP sample was characterized with XRD to analyze the phase structure. The resulting XRD pattern in Fig. 4.7 reveals that the peaks can be fitted well with the reference pattern $Li_{1.2}Al_{0.2}Ti_{1.8}(PO_4)_3$ (rhombohedral crystal structure, $R\bar{3}c$). A small amount of secondary phase of $AlPO_4$ (Orthorhombic crystal structure, $C222_1$) can be observed in the material, hence being in agreement with observations reported in section 4.1.1.

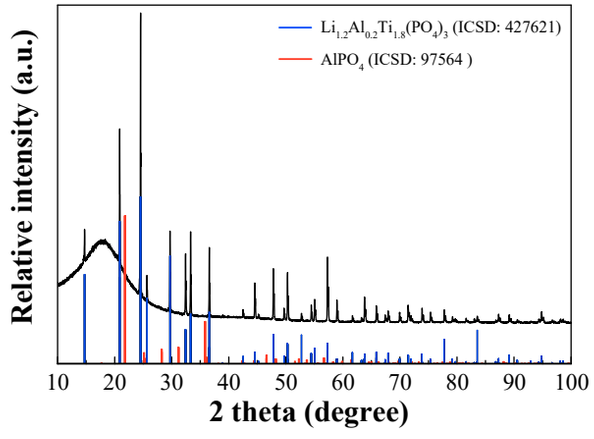

Figure 4.7 XRD pattern of as-sintered LATP sample.

Elastic modulus and hardness of $AlPO_4$ are around 77 GPa [227, 228] and 3.5 - 5.5 GPa [234], respectively, which means that they are significantly lower than the mechanical

parameters of the LATP characterized here, hence any effect of localized testing of this phase would have been obvious. Hence, overall, the effect of the secondary phase on the experimental results can be neglected since the amount of $AlPO_4$ is low and $AlPO_4$ is located in the grain boundaries, and during the analysis within a grain only the indentations which yielded similar load-displacement curves were chosen to do the mechanical properties evaluation corresponding to the specific grain orientation.

The lattice parameters of LATP calculated from the Rietveld refinement, as shown in Table 4.4, are the same as in section 4.1.1 and are in good agreement with that of $a^*=b^*$=0.84941 - 0.85068 nm, c^*=2.08586 - 2.09085 nm as reported in [240]. Since the LATP crystal structure is the same as that of $LiTi_2(PO_4)_3$, and even with Al^{3+} doping the lattice parameter is similar as that of $LiTi_2(PO_4)_3$ ($a^*=b^*$=0.8535 nm, c^*=2.0883 nm) [210], the elastic constants of $LiTi_2(PO_4)_3$ and the lattice parameters given in Table 4.4 are used for the Vlassak-Nix model below, since lattice constants for LATP were not available.

Being a solid electrolyte material, as a basic characteristic of LATP, the electro-chemical behavior has to be investigated. The ionic conductivity of a LAPT pellet was measured with a potentiostat at room temperature (~ 25 °C). In Fig. 4.8 the Nyquist plots of the imaginary against real impedance of the LATP sample (0.3 mm thickness) is shown, of which the intercept at high frequency was used as representative for the conductivity of the sample. The derived conductivity of LATP in this work is 0.18 mS/cm, which agrees well with the results of 0.2 mS/cm reported in [12, 241].

Table 4.4 Rietveld refined lattice parameters of as-sintered LATP.

	Lattice parameters						
	Space group	a^* (nm)	b^* (nm)	c^* (nm)	α	β	γ
LATP	R-3c h (167)	0.85523	0.85523	2.09652	90°	90°	120°

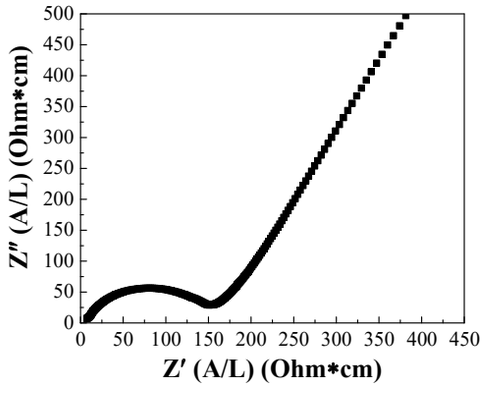

Figure 4.8 Nyquist plot of the LATP material at 25 °C.

The chosen areas for indentation are shown in Fig. 4.9 (a). The red and blue frames with the corresponding EBSD results in all three axes are displayed in Fig. 4.9 (b). Only imprints were considered in the analysis of the data that possessed a regular shape and were located not too close to pores and grain boundaries. The indentations were grouped by the grains with different orientations and then elastic modulus and hardness were analyzed. For analyzation certain grains with at least 3 indents were then considered.

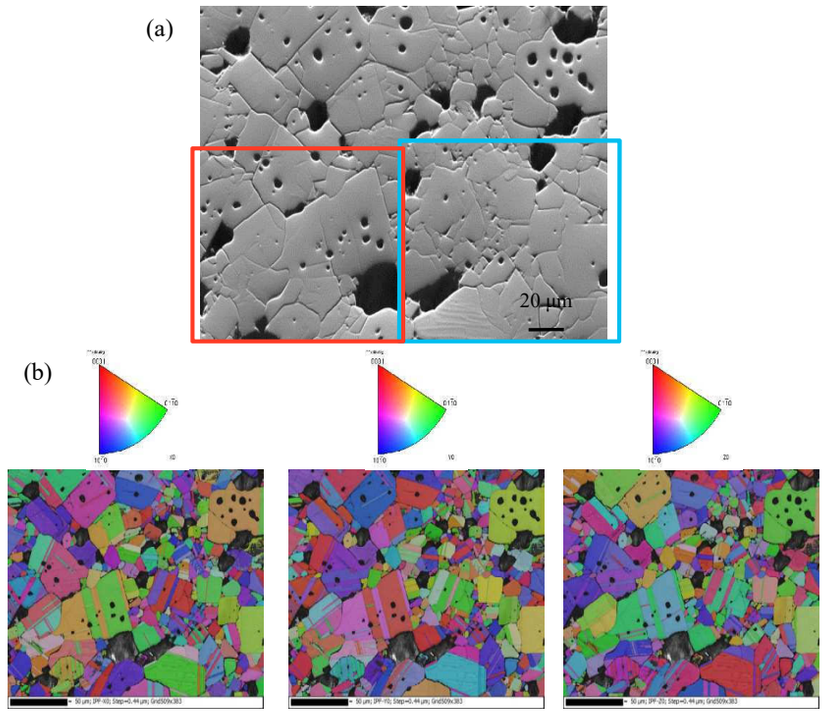

Figure 4.9 The microstructure of LATP material in (a), of which the red and blue marked areas are chosen for indentation test , and (b) the corresponding EBSD result in three axes.

Fig. 4.9 (b) shows that the EBSD images for the well-polished LATP are quite clear, which verifies that any potentially affected layer on the surface was removed, since it was reported that the EBSD pattern quality correlated adversely with the defect density [242]. Thus the mechanical properties of LATP can be analyzed without consideration of potential residual stress effects. Furthermore, the EBSD results indicate that the LATP grains are orientated highly randomly, which permits an appropriate investigation of the anisotropic mechanical properties.

4.2.2 Mechanical properties

Typical indentation load-depth curves for three specific planes are shown in Fig. 4.10, in which (a) shows the curve for an imprint on the basal plane; (b) and (c) show curves for the prismatic type $(10\bar{1}0)$ and $(11\bar{2}0)$ planes. The specific plane was determined based on the Euler

angle Φ, i.e. the angle between the selected plane and the basal plane or prismatic plane, which was supposed to be less than 10°. Since the indentation test was carried out in a depth control mode, all three curves reached a depth of 300 nm, however, since the holding time at maximum load was 10 s (to avoid reversible plasticity) the maximum depth before unloading was slightly larger than 300 nm.

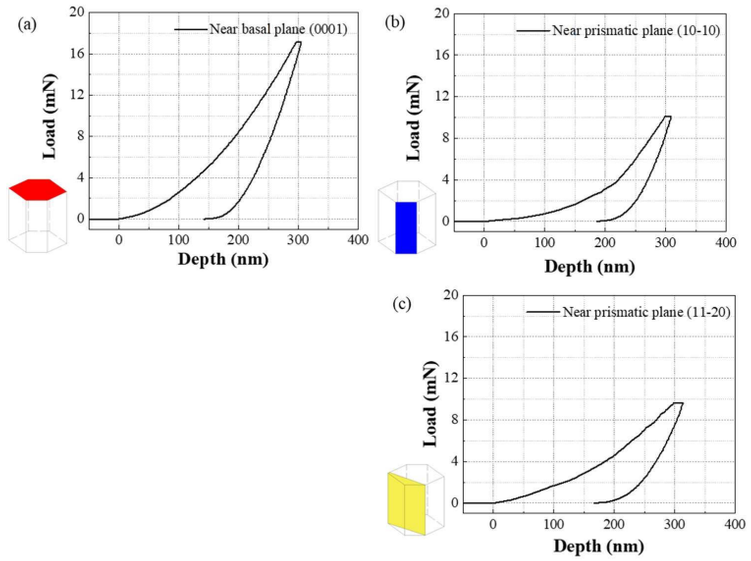

Figure 4.10 Typical load-displacement curves for indentation test in specific orientation: (a) on the plane close to basal plane, (b) and (c) on the prismatic type planes.

The curve shapes, which are the basis for obtaining the experimental elastic modulus and hardness, for all three planes are different, which verified that the LATP material's mechanical properties are anisotropic. Obviously the maximum loads for the two prismatic planes are very similar, whereas the maximum load for the basal plane was much higher. As illustrated in Fig. 4.9, some of the indentations were out of the area characterized by the EBSD pattern and some are close to the defects like pores, which needed to be eliminated from the analysis. Thus, the amount of the valid data that could be associated with different grains was limited.

Elastic modulus and hardness of the LATP sample are presented in three dimensional charts with the two axes representing the angle from the basal orientation (Φ) and the angle from prismatic orientation ($\varphi 2$), as can be seen in Fig. 4.11. The data was expanded via the software "Origin" converting the worksheet to matrix to make the 3D colorful surface map. Here the surface mapping has no physical meaning and is only used as a guide for eyes to observe clearly the dependency of mechanical properties on rotation angles. To permit a clearer understanding of the graphs the deviations of E and H are shown and discussed in more detail below.

It can be seen in Fig. 4.11 that elastic modulus and hardness of LATP reveal a similar trend with variation of the angles (Φ, $\varphi 2$). It is notable that, with the increasing of Φ, i.e., angle of the indented plane rotating from the basal plane towards the prismatic plane, E and H decrease significantly. Yet the $\varphi 2$, i.e., angle of the indented plane rotated from prismatic $(10\bar{1}0)$ type plane to another $(10\bar{1}0)$ plane through the prismatic $(11\bar{2}0)$ type plane, has no obvious effect on the mechanical properties. This manifests that the rotation angle Φ is the dominant factor influencing the anisotropic behavior of the LATP material, which agrees well with the hexagonal material β-Si_3N_4, as reported in [209].

The elastic modulus decreases from 150 ± 3 GPa for the basal plane to 107 ± 4 GPa for the prismatic plane, whereas the hardness decreases from 10.0 ± 0.2 GPa for the basal plane to 5.5 ± 0.3 GPa for the prismatic plane, each being the individual maximum and minimum experimental data points regarding to the individual grains.

As demonstrated in section 4,1,2, the elastic modulus and hardness of LATP at load of 30 mN is 127 ± 10 GPa and 9.8 ± 0.9 GPa, respectively. Contrary to the loading control mode, under the depth control mode of 300 nm it can be found that the load is in the range of 10 – 16 mN. Moreover, based on the nanoindentation mapping test the average elastic modulus and hardness is calculated as 131 ± 4 GPa and 8.3 ± 0.3 GPa, respectively. This implies the mechanical properties at 30 mN is close to these average properties, which manifests that it is reasonable that the elastic modulus and hardness of LATP at 30 mN is in between the values of elastic modulus and hardness of LATP basal plane and prismatic plane.

It was reported by Jackman et al. that *E* of LATP ranged from 81 to 115 GPa and *H* was 7.1 ± 0.4 GPa [12], and Deng et al. reported that *E* of the $LiTi_2(PO_4)_3$ type material ranged from 139.0 to 152.5 GPa as derived via first principle calculation [166]. Taking orientation effects into consideration, elastic modulus and hardness obtained here are in good agreement with these data.

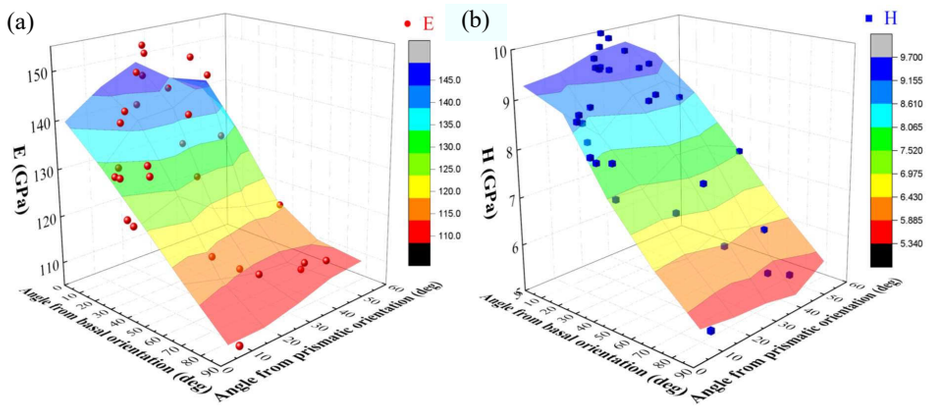

Figure 4.11 Experimentally derived mechanical properties of the LATP as a function of the corresponding angle: (a) elastic modulus and (b) hardness, here the colorful surface map is the guide for the eye to see the dependency of mechanical properties on rotation angle.

Typical morphologies of imprints in different magnifications can be seen in Fig. 4.12 (a) and (b). It can be found that the indentations are homogeneously distributed over the sample surface in Fig. 4.12 (a). The distance between the indents was 5 μm and no interaction between the imprints inside the grain is visible in Fig. 4.12 (b), which manifests that the indentation results represent the local property within each selected grain. With the aid of the green triangle it can be seen that the models assuming sink-in behavior is adequate. In addition, around the indentations no clear slip lines can be observed.

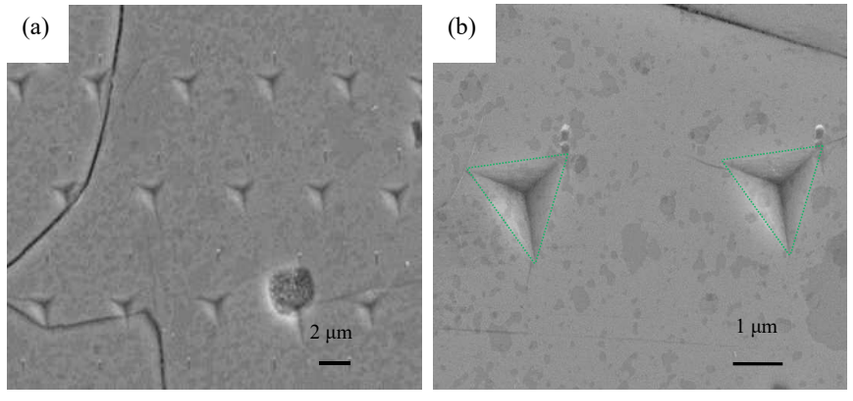

Figure 4.12 SEM images of the typical imprint morphologies in (a) and (b).

As outlined above, the Vlassak-Nix and easy-slip models are adopted here to calculate indentation elastic modulus and hardness ratio, respectively, corresponding to the rotation angle of the crystal structure, as shown in Fig. 4.13. The indentation modulus and hardness are derived as a function of Φ from 0° to 180° with 1° per step to show a detailed symmetric variation. In order to see any effects in the mechanical properties with respect to angle $\varphi 2$, i.e., the initio angle for calculation between the normal of the indented surface and the *X*-*Z* plane of the crystal coordinate system at *X*-*Y* plane, three typical plots, at $\varphi 2$ = -30°, 0° and 30°, are selected for both indentation modulus and hardness ratio.

It can be seen that in the interval of Φ from 0° to 90°, i.e. the indented plane being rotated from the basal plane to the prismatic plane, the indentation modulus decreases continuously with a maximum value of 177 GPa at 0° and a minimum value of 118 GPa at 90°. With respect to the hardness ratio, results for the hardness at 90° are used as a reference value; the ratio is highest of 2.0 at 0° and then decreases to 0.96 at 70°, afterwards the value rises to 1 at 90° in a semi-period.

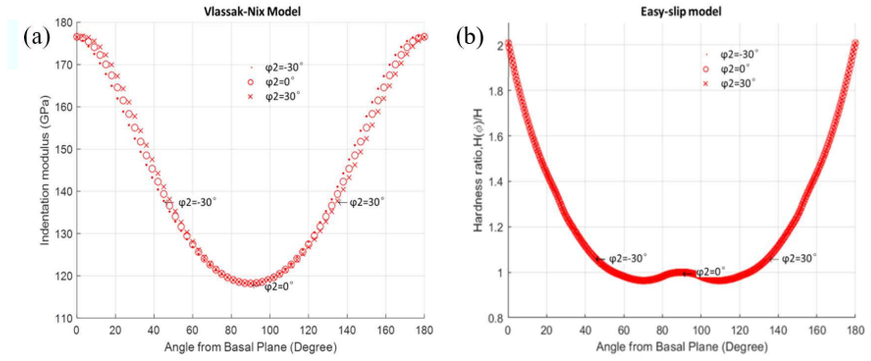

Figure 4.13 Indentation elastic modulus and hardness ratio as a function of angle Φ in (a) and (b), respectively. Representative angles φ2 of -30°, 0° and 30° are selected to see the limited effect of this angle on the mechanical properties.

The angle $\varphi 2$ has only a small effect on the indentation modulus, i.e. with increase of $\varphi 2$ the indentation modulus and hardness plots shift right with the same maximum and minimum value, whereas the $\varphi 2$ angle has no observable influence on the hardness ratio. Thus it can be confirmed that the angle Φ is the dominant factor in affecting the anisotropic mechanical properties of rhombohedral LATP material, and, therefore, the comparison of the experimental results and calculated results is discussed only in terms of the Φ angle.

In order to compare both the experimental and the Vlassak-Nix model's indentation modulus, the value based on the equation $M = \frac{E}{1-\vartheta_s{}^2}$ was used. So to permit a comparison of the experimental results and the two model's predictions, the experimental and model's results of elastic modulus and hardness are plotted as a function of angle Φ in Fig. 4.14, where the experimental hardness is normalized (using the value at $\Phi = 90°$ as reference data).

It can be seen from Fig. 4.14 (a) that the experimental normalized E possesses the same trend as the one predicted by the Vlassak-Nix model. Nevertheless, the indentation modulus values, especially at low Φ angles, are slightly lower than the data derived from the theoretical model. In the current work the calculated experimental indentation modulus decreases from 160 ± 4 GPa for the basal plane to 114 ± 4 GPa for the prismatic plane. It can be observed that the extreme

value of the experimentally obtained indentation modulus is slightly lower than the one predicted from the Vlassak-Nix model, i.e. the difference is 10%. The normalized hardness shows a decreasing trend with increasing angle, similar to that of the data derived from the easy-slip model, as shown in Fig. 4.14 (b). The ratio of the maximum of the experimental data is around 1.8, being lower than that of 2.0 from the easy-slip model. The experimental normalized H for Φ values in the range of 20° - 70° is higher than the predicted data as well as the reference data point, while the easy-slip model yields a minimum value at Φ of 70°. No difference can be obtained for the experimentally derived and predicted hardness value, since due to the limitation of the easy-slip model no absolute value of hardness can be calculated and only the variation trend can be anticipated.

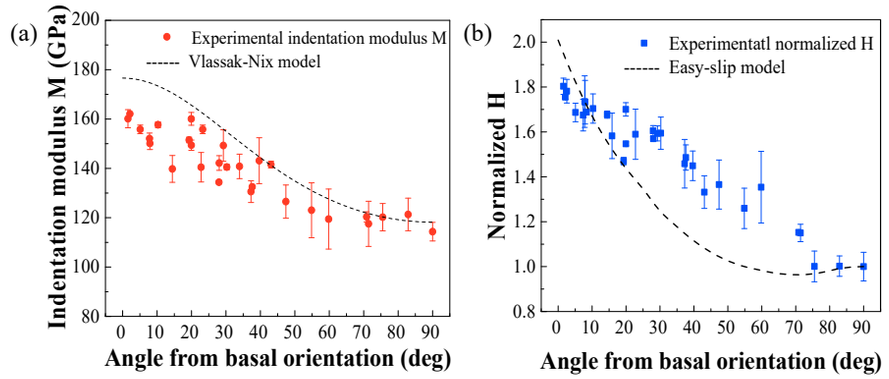

Figure 4.14 A comparison of the experimental anisotropic indentation modulus and the calculated one according to the Vlassak-Nix model in (a), and the normalized experimental anisotropic hardness and the hardness ratio from easy-slip model in (b).

The differences between the experimental and theoretical outcomes can be a result of many factors. Due to the randomness of the grain orientation, some experimental points especially the data at Φ of 0° were missing. In addition, the usage of the elastic constants based on $LiTi_2(PO_4)_3$ material and the 6 slip systems simplified via ruling out the unidirectional slip lowered down the accuracy of the prediction of the two models. Even so, the Vlassak-Nix model and easy-slip model still permit a close estimate of the elastic modulus and hardness of the LATP material

although further improvement appears to be possible in future works concentrating on these predictive approaches.

In consideration of the mechanical behavior in analytical and simulation approaches of solid-state lithium batteries with thick electrolyte obviously usage of the average mechanical properties of the electrolyte is sufficient as long as only the macroscopic behavior is considered, however, once approaches go down to the behavior on the level of individual grains, in particular when the growth of dendrites is an aspect of concern, local properties and their differences become interesting. Similar for the micro-batteries the thickness of the electrolyte goes down to the grain size, the mechanical properties of individual grains like elastic modulus and hardness become prominent effects and need to be taken into account of battery design and analysis of aspects related to strains and stresses.

4.2.3 Summary

The anisotropy of the mechanical properties of the solid electrolyte material LATP was investigated in this work via indentation mapping test with depth control mode at room temperature and associate EBSD characterization. The LATP ceramic electrolyte with a rhombohedral crystal structure was studied and the imprints after indentation were analyzed. The experimental elastic modulus and hardness as a function of rotation angle from basal plane to prismatic plane were assessed and compared with those predicted by the Vlassak-Nix and easy-slip model, respectively, which were used to calculate a theoretical modulus and hardness ratio, respectively.

Noticeable anisotropic mechanical properties of LATP material were observed. The experimental elastic modulus and hardness of LATP showed a similar trend, i.e. that the rotation angle $\varphi 2$ between two prismatic $(10\bar{1}0)$ type planes had no detectable influence, whereas when the rotation angle Φ from basal plane to prismatic plane increased, E and H value decrease conspicuously. The Vlassak-Nix and easy-slip model demonstrated that the angle $\varphi 2$ has a negligible effect and the difference between the results of the two models' results was that, as the angle Φ increased, the indentation modulus from the Vlassak-Nix model decreased continuously while the hardness ratio derived by the easy-slip model decreased to the minimum value at 70°

and then increased slightly. The comparison of experimental results and theoretical calculation was discussed only in terms of the rotation angle Φ, since the angle Φ appears to be the dominant factor on the mechanical properties of LATP.

The experimental elastic modulus is in the range of 150 ± 3 GPa to 107 ± 4 GPa and the hardness is in the range of 10.0 ± 0.2 GPa to 5.5 ± 0.3 GPa, whereas the average elastic modulus and hardness for all data is calculated as 131 ± 4 GPa and 8.3 ± 0.3 GPa, respectively. As demonstrated in section 4,1,2, the elastic modulus and hardness of LATP at load of 30 mN is 127 ± 10 GPa and 9.8 ± 0.9 GPa. This implies the mechanical properties at 30 mN are close to the average properties as reported in section 4.1.2.

The experimental indentation modulus fitted well with the prediction of the Vlassak-Nix model, yet the model showed an around 10% higher extremum (118 - 177 GPa) than the experimental results (114 - 160 GPa). The experimental hardness was normalized to compare with the hardness ratio from the easy-slip model and the trend of two results was comparable. The difference between the experimental results and the models' results can be ascribed to simplification for calculation such as that the Vlassak-Nix model adopted the $LiTi_2(PO_4)_3$ material's elastic constants, the easy-slip model took the simplified 6 slip systems into account. Besides, more experimental data points could be gained in future work, especially the result around $\Phi = 0°$. This work presents data supporting an understanding of the anisotropic mechanical properties of the rhombohedral crystalline LATP material and provides a basis for further improvement of the Vlassak-Nix and easy-slip model.

4.3 $Li_{1.5}Al_{0.5}Ti_{1.5}P_3O_{12}$:$SiO_2$ and $Li_7La_3Zr_2O_{12}$: Fracture reliability

For brittle materials that possess an inherent scatter in fracture stresses, a fracture-based reliability analysis is of paramount importance, since here safety factors are the most uncertain aspect of a design. In real application, the electrolyte experiences stress and the contact to other materials. The probability distribution of structural strength and lifetime are known to follow a Weibull distribution, determining the time or load related to a tolerable failure probability [203]. The Weibull statistics of $Li_{1.3}Al_{0.3}Ti_{1.7}(PO_4)_3$ has been reported by Jackman et al. that the

Weibull modulus and characteristic of $Li_{1.3}Al_{0.3}Ti_{1.7}(PO_4)_3$ with fine grain and low porosity is 12 and 130 MPa, respectively. Yet the Weibull statistics of $Li_7La_3Zr_2O_{12}$ still needs to be investigated. Since porosity has a significant impact on the mechanical behavior of the material [243], and the densification of LATP can be enhanced by adding SiO_2 powders [244], the mechanical properties of the $Li_{1.5}Al_{0.5}Ti_{1.5}P_3O_{12}$:$SiO_2$ (LATP:Si) and dense $Li_7La_3Zr_2O_{12}$ (LLZO) are chosen in this work for the mechanical assessment via indentation tests and bending tests.

4.3.1 $Li_{1.5}Al_{0.5}Ti_{1.5}P_3O_{12}$:$SiO_2$: Fracture reliability[3]

4.3.1.1 Composition, microstructure and conductivity

After sintering, the XRD patterns were recorded to detect secondary phases, which are common for LATP-type ceramics (see also Fig. 4.15, see also section 3.1.2). The LATP:Si sample shows a rhombohedral structure (space group $R\bar{3}c$) with LATP as main phase. It can be found that the LATP:Si contains negligible amount of secondary phase ($AlPO_4$) compared to that of LATP samples discussed in section 4.1 and section 4.2. Since the added SiO_2 binder was only ~ 1.5wt%, no signal related to it could be detected in XRD spectra. Via Archimedes' method the relative density of LATP:Si was assessed of which the relative density is 99.8%, which is higher than that of LATP samples, section 4.1 and 4.2, making the modified material promising for practical application. The fracture surface observation of the as-sintered LATP:Si sample is shown in Fig. 4.16. The small size grains inside the sample can lead to the densification of the sample.

[3] Section content published: E., Dashjav, M., Gellert, G. Yan et al. Journal of the European Ceramic Society (2020), 40, 1975-1982.

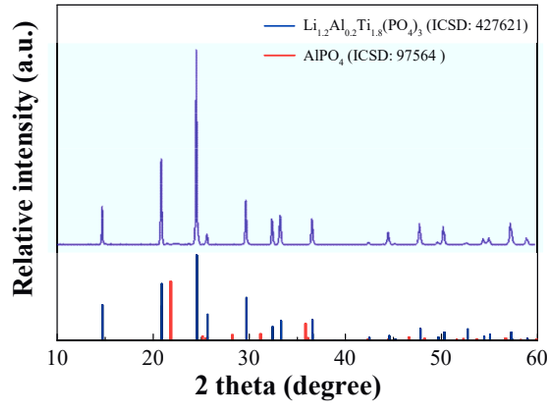

Figure 4.15 XRD pattern of sintered LATP:Si tape.

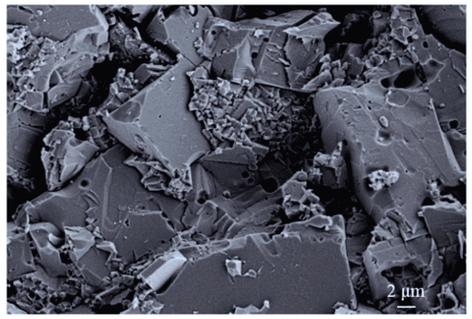

Figure 4.16 SEM micrograph of fracture surface of LATP:Si.

The typical Nyquist plot showing the complex impedance of LATP:Si is given in Fig. 4.17 (a). Generally, the Nyquist diagrams consist of three different parts: two semicircles representing the grain and grain boundary conduction processes, followed by a capacitive process associated with the electrode polarization. The grain boundary and bulk processes can be clearly separated, but only up to temperatures of -100 °C, whereas at higher temperatures the grain boundary process cannot be separated from the bulk resistance. So only the total conductivity can be extracted. Thereafter the Arrhenius plot of the bulk and total conductivity, here equivalent to the grain boundary conductivity, is shown in Fig. 4.17 (b). The total resistance of the material is dominanted by the grain boundary, which are two times as resistive as the bulk, resulting the

total ionic conductivity of 0.2 mS/cm at 20 °C. The conductivity of the current LATP:Si is similar to that of LATP sintered at 1000 °C (0.18 mS/cm at 20 °C), as demonstrated in section 4.1 and 4.2, which implies the tape casted LATP mixed with SiO_2 is a competitive electrolyte. As a comparative, the bulk conductivity was extrapolated as 1.2 mS/cm at 20 °C which agrees well with the results for singe crystals [245].

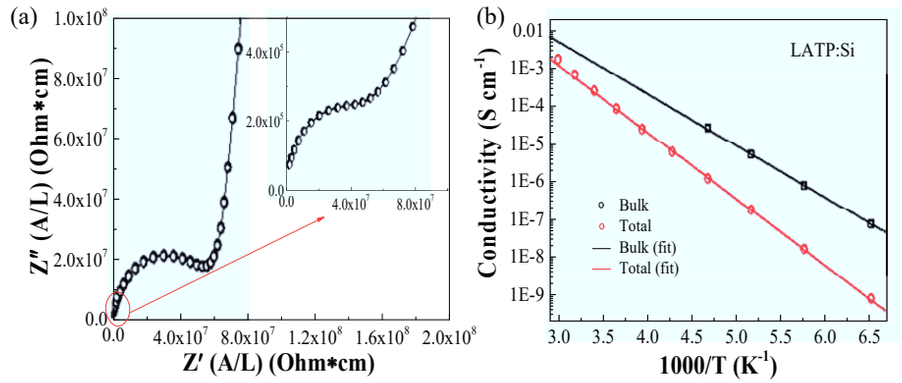

Figure 4.17 Nyquist diagram of LATP:Si in (a), Arrhenius plot of the bulk and total conductivity of LATP:Si in (b).

4.3.1.2 Fracture reliability

Regarding hardness, elastic modulus and fracture toughness, the LATP:Si was tested by the commonly used indentation method, where the maximum applied load was 500 mN (penetration depth ~ 3 μm). Elastic modulus and hardness of LATP:Si as a function of load are presented in Fig. 4.18. It can be seen that both, *E* and *H*, decrease with increasing load, similar as observed for the material without Si in section 4.1. Comparing to the elastic modulus and hardness of LATP as displayed in Fig. 4.3 and 4.4, the decrease here is similar. The impact of the grain boundaries on the mechanical properties increases due to the wider load-carrying zone, which appears to decrease the apparent properties of the material [229]. In addition, the bimodal grain size can also enhance the load dependence of mechanical properties as small grains induce more grain boundaries.

By the virtue of the low porosity, effects of voids appear to be negligible. The *E* and *H* at low load represent the intrinsic property of the LATP:Si, whereas the values at higher load indicate the polycrystalline property.

Average elastic modulus and hardness at the low load of 30 mN are 109 ± 5 GPa and 8.7 ± 0.4 GPa, respectively. As discussed in section 4.1, the elastic modulus and hardness of the hot pressed LATP materials sintered at 950 °C at 30 mN are 118 ± 5 GPa and 9.3 ± 0.3 GPa, respectively, which indicates that the *E* and *H* of LATP:Si sintered at 920 °C are similar.

Literature values of the elastic modulus of LATP are in range 81 to 115 GPa [12, 246], for the hardness 7.1 ± 0.4 GPa [12]. The elastic modulus and hardness of LATP:Si appear to be slightly higher than reported in [12]. The sample here has a density of 99.8% with small grains filled in the interstitial space of large grains as seen in Fig. 4.16, whereas the density of LATP was 97.0% [12] with grain sizes of around 30 μm. Besides, in Jackman and Cutler's work [12], the elastic modulus was measured via ring-on-ring test machine, where the effectively deformed zone and hence apparent porosity and grain boundaries was way larger than the indentation test adopted here. As shown in the above results, the higher load-carrying zone the lower *E* and *H* values.

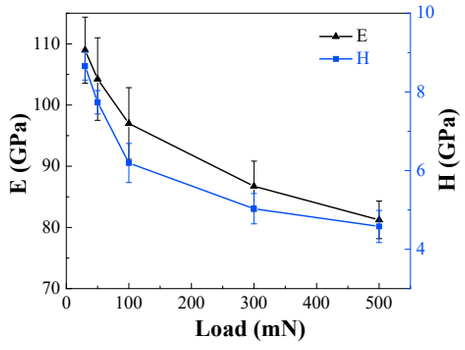

Figure 4.18 Elastic modulus and hardness of LATP:Si as a function of indentation load.

Vickers indentations were utilized to determine the fracture toughness of LATP:Si at different loads. It was found that below 1 N no obvious cracks could be generated and above 10 N the sample surface was crushed. Hence, the fracture toughness of LATP:Si was tested at 3 N and 5 N. Since the ratio of the crack length (l) to half-diagonal (a) of the cracks met with the condition ($l/a \geq 1.25$) of median (half-penny) cracks, and the Equation 2.13 was adopted [247]. The derived fracture toughness values of LATP:Si for loads of 3 N and 5 N are 1.1 ± 0.3 and 1.2 ± 0.3 MPa·m$^{1/2}$, respectively, hence, being independent of the applied load.

As described in section 4.1, the derived K_{IC} values of LATP sintered at 1050 °C and 1100 °C with load of 0.5 N were 1.4 ± 0.2 and 1.6 ± 0.2 MPa·m$^{1/2}$, whereas no valid fracture toughness of LATP 950 °C and LATP 1000 °C could be calculated. The K_{IC} value of LATP:Si sintered at 920 °C is lower than that of LATP 1050 °C and 1100 °C, which can be ascribed to a sintering temperature effect, see also section 4.1, which corresponds to the higher amounts of pores inside the grains of samples sintered at lower temperature.

Jackman and Cutler [12] reported that the fracture toughness of LATP material determined by the single edge notch bending method was 1.1 ± 0.3 MPa·m$^{1/2}$, which is in very good agreement with that of LATP:Si characterized here. Furthermore, for comparison, the fracture toughness of garnet-type electrolyte $Li_7La_3Zr_2O_{12}$ is in the range 0.9 to 1.25 MPa·m$^{1/2}$ [13] and for the perovskite-type electrolyte $Li_{0.33}La_{0.57}TiO_3$ it is 1.15 to 1.24 MPa·m$^{1/2}$ [17], which reveals that LATP:Si has a similar fracture toughness like other potential solid electrolytes .

In order to gain insight into fracture stresses and reliability of the samples, ball-on-three-ball bending tests were carried out at room temperature [201]. The derived fracture stress data were described by a 2-parameter Weibull statistics yielding the characteristic strength and Weibull modulus [155]. A minimum number of 30 specimens is suggested in the industrial standards as a basis for a Weibull statistical analysis [203]. However, limited materials availability (13 samples) did not permit to test such a large number of specimens and hence, although the data were analyzed using Weibull statistics, the result should only be considered as a tentative indication of the materials behavior.

As illustrated in Fig. 4.19, the Weibull parameters were calculated by linear fitting with 90% confidence intervals as σ_0 = 168 [160.7 – 175.3] MPa and m = 12.8 [7.8 – 16.8]. The effective volume of LATP:Si can be calculated via online web-tool (http://www.isfk.at/de/960/) [199] as 0.265 mm^3. The mechanical properties of LATP:Si, summarized in Table 4.5, are slightly better than that of LATP reported by Jackman and Cutler [12], where for high purity fine grained (HPFG) LATP the characteristic strength is 130 MPa and Weibull modulus is 8. The effective volume of HPFG LATP was calculated to be 26 mm^3.

According to the Weibull' theory [203], the fracture strength is related to the sample volume of which the referred fracture strength σ_{ref} at unit volume can be expressed as:

$$\sigma_{ref} = \left(\frac{V_{effective}}{V_{ref}}\right)^{\frac{1}{m}} \cdot \sigma_0 \tag{4.1}$$

where $V_{effective}$ is the effective volume of the tested sample and V_{ref} the referred volume which is assumed to 1 mm^3 here. It can be calculated that the referred fracture strengths at unit volume of 1 mm^3 of LATP:Si here and LATP in the literature [12] are 151 [135 – 162] MPa and 195 MPa, respectively. The respective fracture strength of LATP:Si is lower than that of the material reported in the literature probably due to the tape casting process an associated defects [248].

It can be seen that the Weibull modulus of LATP:Si is in the similar range as for other ceramic materials, i.e. 5 to 20 [249]. Compared with the ceramic materials $LiNbO_3$ and $LiTaO_3$ that were tested with the same B3B test method as reported by Gruber [154], the Weibull modulus of LATP:Si is higher than that of $LiNbO_3$ (3.8 - 6.9) and $LiTaO_3$ (3.4 - 6.3), although the limited number of specimens and the confidence interval require further tests for final conclusion. However, the characteristic strength is lower than for example that of the cathode materials $LiNbO_3$ (638 – 2036 MPa) and $LiTaO_3$ (669 – 1802 MPa). It can be assumed that the fracture reliability of the solid electrolyte LATP:Si (size of $6.6 \times 7.1 \times 0.2$ mm^3) is superior to that of the cathode materials $LiNbO_3$ and $LiTaO_3$ according to the higher Weibull modulus. The Weibull statistics of LATP:Si here can be used as a reference for further LATP materials design and as a comparison in probabilistic maximum stress calculations for simulations of components.

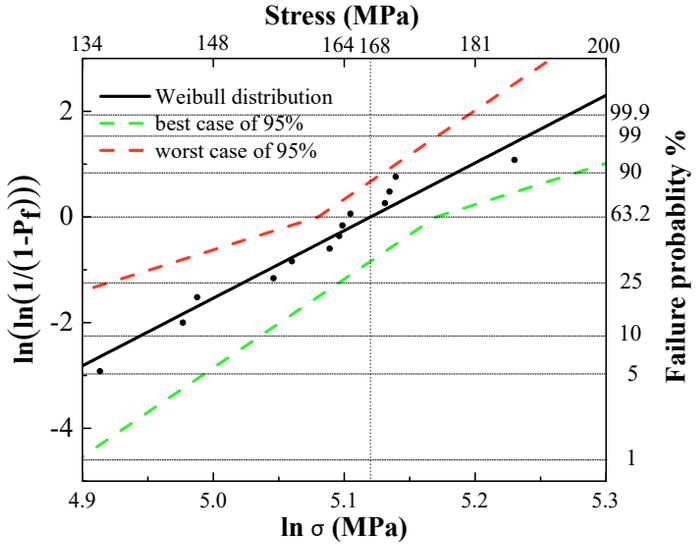

Figure 4.19 Fracture stress distribution and Weibull parameters of LATP:Si tapes.

Table 4.5 Mechanical properties of the LATP:Si material.

E (GPa) at 30 mN	H (GPa) at 30 mN	K_{IC} (MPa·m$^{1/2}$) at 3 N	m	σ_0 (MPa)
109 ± 5	8.7 ± 0.4	1.1 ± 0.3	12.8 [7.8 – 16.8]	168 [160.7 – 175.3]

In order to derive the fracture origin, the fracture surfaces of various specimens and individual pieces were analyzed in more detail. Typical fracture surfaces of LATP:Si at different magnifications are shown in Fig. 4.20. As examples, Fig. 4.20 (a) and (b) show the lateral view of the two sides of one individual fracture surface. It might be interpreted that large grains were removed during fracture or large individual pores are the crack origin. The critical flaw size can be estimated by the equation [141]:

$$\alpha = \frac{1}{\pi}\left(\frac{K_{IC}}{\sigma_0}\right)^2 \tag{4.2}$$

where K_{IC} is the fracture toughness and σ_0 is the fracture stress. Based on the individual fracture stress of the specimens and the fracture toughness, an α of ~ 30 µm is calculated, which is in good agreement with the identified failure origin, which according to Fig. 4.20 (b) has a size of ~ 30 µm. As shown in Fig. 4.20 (c), the crack goes through the internal pores of the grain. Overall, the cracks propagate both intergranularly and transgranularly. This suggests that the pores weaken the large grains leading to lower strength of large grains than that along grain boundaries. Therefore, improving the density of the LATP:Si and the LATP microstructure can enhance the material's strength in real application.

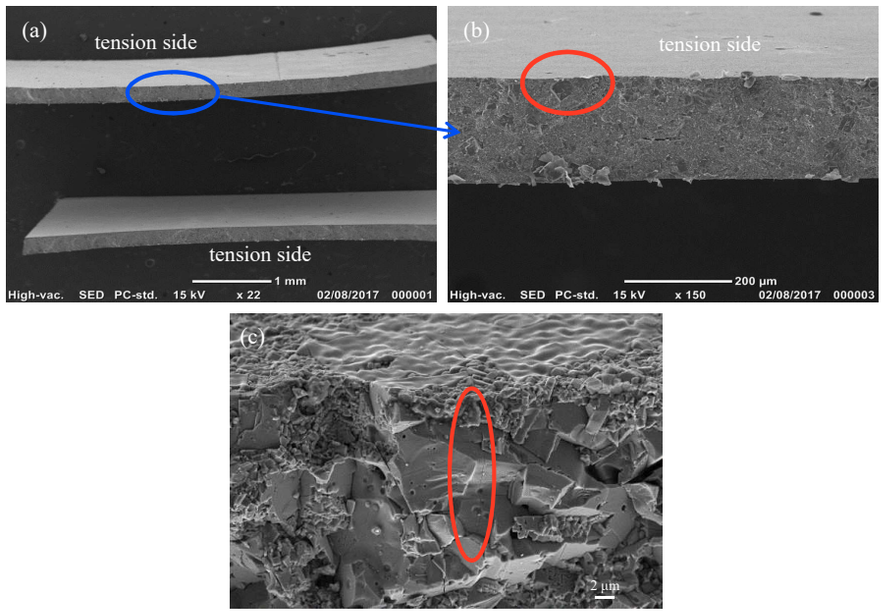

Figure 4.20 Typical crack surface of the LATP:Si samples. (a), (b) and (c) show the same sample in different magnifications. The blue circle in (a) is enlarged as shown in (b) where the red circle show the potential fracture origin. (c) shows the higher magnifications of the fracture surface, and the red circle indicates the transgranular crack growth.

4.3.1.3 Summary

The LATP:Si material shows similar elastic modulus and hardness like LATP 950 °C in section 4.1, being however higher than that the values reported for other LATP materials [12, 246]. The fracture strength as well as Weibull modulus of LATP:Si reported here might be used as indicators for the design of electrolyte-based batteries in term of safety issues. The observation of the fracture surfaces of LATP:Si reveals that the pores inside large grains or the large grains themselves reduce fracture stresses. One way to strengthen the LATP:Si material is to densify the sample further during the sintering process and reduce the grain size. The $Li_{1.5}Al_{0.5}Ti_{1.5}P_3O_{12}$ mixed with SiO_2 was sintered achieving a high density, which allowed reliable investigating of the mechanical properties. The fracture strength，168 MPa, and Weibull modulus, 13, of LATP:Si have been investigated, which can provide the basis for future macroscopic modeling of LATP components in solid state batteries. The mechanical measurements of LATP:Si demonstrate that an improvement of the mechanical properties can be achieved by densifying the structure and reducing the grain size.

4.3.2 $Li_7La_3Zr_2O_{12}$: Fracture reliability and lifetime prediction [4]

4.3.2.1 Composition, microstructure and conductivity

A fracture surface of a LLZO pellet is shown in Fig. 4.21 to reveal details on the microstructure. Via Archimedes method the relative density of 93% for as-sintered samples was obtained and the grain size of LLZO was evaluated as 13.5 ± 7.2 µm. It can be seen, the material is rather dense and pores appear to be randomly distributed, in addition, the grain size distribution appears to be bimodal.

[4] Section content published: G. Yan et al. Journal of Materials Science (2019), 54(7), 5671-5681.

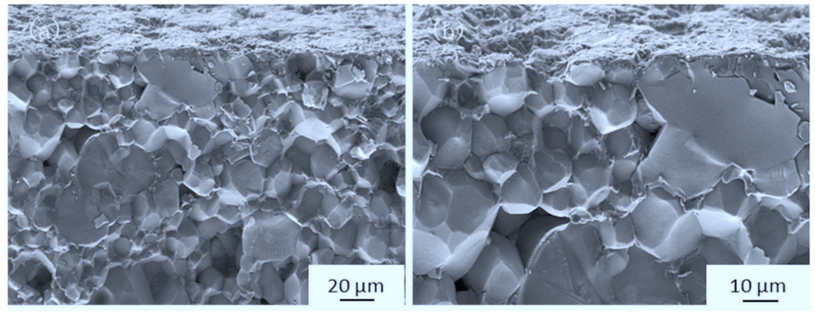

Figure 4.21 SEM fracture cross-section of LLZO.

X-Ray diffraction was used to characterize the phases after calcination. The result in Fig. 4.22 verifies that the material is in pure garnet phase state (cubic ICSD: 131842, tetragonal ICSD: 131954) with lattice parameter of 1.2970 nm in cubic crystal structure, lattice parameter of 1.3093 nm and 1.2716 nm in tetragonal crystal structure, which is in good agreement with that reported in [13, 14]. The Nyquist plot for LLZO at room temperature is shown in Fig. 4.23, where the inset shows the detailed curve at low frequencies. Unfortunately, the bulk and grain-boundary conductivity cannot be differentiated with the equipment and thus only the total ionic conductivity was calculated. The conductivity of the pellet is around 8.0×10^{-4} S/cm at RT, which indicates that the conductivity of the LLZO investigated in this work is higher compared to that of $\sim3.0\times10^{-4}$ S/cm at RT reported by Tsai et al. [250]. The LATP and LATP:Si samples in the previous sections revealed for comparison conductivities of ~ 0.2 mS/cm, hence, the LLZO materials' ionic conductivity is slightly lower.

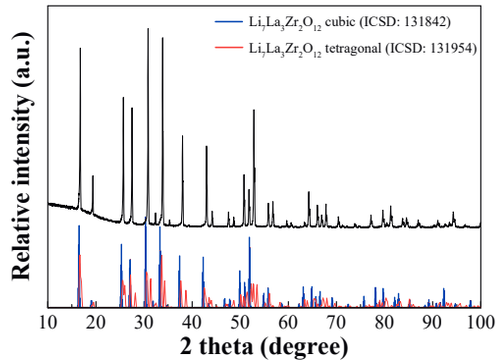

Figure 4.22 XRD patterns for LLZO sintered at 1200 °C in air for 8 h.

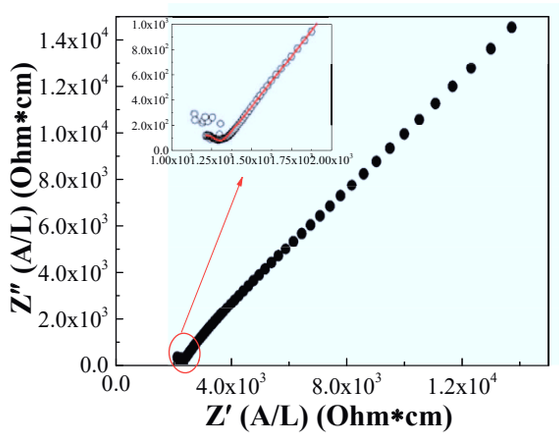

Figure 4.23 Nyquist plot for LLZO at room temperature.

4.3.2.2 Fracture reliability and lifetime prediction

Elastic modulus and hardness were obtained from nano-indentation data. A typical indentation mark (loading 100 mN) is shown in Fig. 4.24.

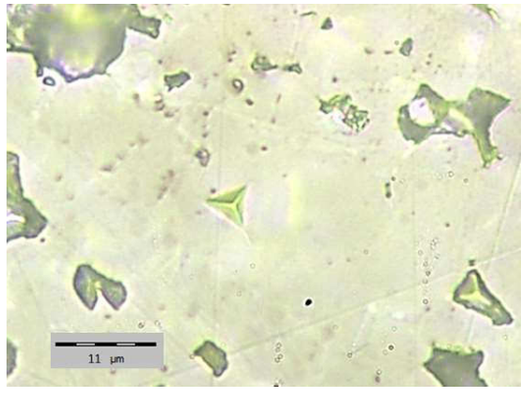

Figure 4.24 Nano-indentation impression in LLZO, load of 100 mN.

Elastic modulus and hardness as function of load are presented in Fig. 4.25. Both, *E* and *H* first increased and then gradually decreased as the depth increases. The elastic modulus and hardness at low load are 117 ± 4 GPa and 9.4 ± 0.5 GPa, respectively, which are considered to be representative for the material in its dense state. As the load was increased gradually to 500 mN, the elastic and plastic zone increased (note, the former is around ten times larger than the plastic zone). As the load-carrying zone increases, the effect of grain boundaries and especially also voids on the measured properties increases, decreasing apparent properties. This indicates that as the indentation depth increases, the determined *E* and *H* get closer to the properties being representative of the bulk, i.e. global behavior, of the sample, which is the property assessed via the ring-on-ring test below [251].

As reported by Nonemacher et al. [14], the elastic modulus and hardness are in the range of 124 – 163 GPa and 9.0 – 11.8 GPa, respectively. The slight difference might be attributed to the continuous multi-cycle mode, whereas in this work the load control mode was adopted, which effectively means that the literature results were obtained at lower load leading hence to higher values. Taking the experimental method into consideration it can be concluded that the *E* and *H* of LLZO here agree well with those literature results [14].

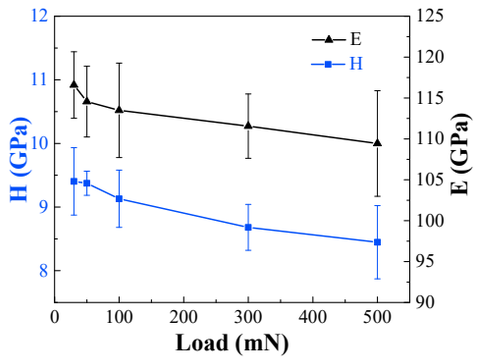

Figure 4.25 Elastic modulus and hardness of LLZO as a function of indentation load.

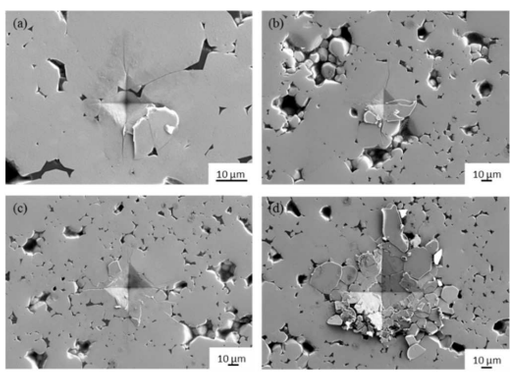

Figure 4.26 Indentation imprints for K_{IC} calculation, (a), (b), (c) and (d) represents imprints for 1 N, 3 N, 5 N and 10 N, respectively.

Typical indentation imprints in LLZO that were used for K_{IC} calculation are shown in Fig. 4.26, for loads of 1, 3, 5 and 10 N, respectively. Below 1 N, the crack length was insufficient for toughness evaluation [119, 146, 147]. From Fig. 4.26 it can be seen that the cracks exhibited asymmetrical lengths and spallation between some cracks for all loads. Even for 1 N, it was still difficult to determine the crack length due to chipping effects. Especially at 10 N the material crushed, hence, for this load it was not possible to evaluate any toughness. For 1, 3 and 5 N the ratio of the crack length to imprint half–diagonal varied, meeting conditions for both Palmqvist and median cracks. For K_{IC} calculation four equations [119, 146, 147] were used as shown in

Table 2.4, two assuming a Palmqvist and two assuming a median crack, and the results are presented in Fig. 4.27. The fracture toughness values are rather independent of the load in each model, hence, neither crack shape nor load dependency permitted a selection of the most suitable analysis procedure. The derived indentation fracture toughness of LLZO material was in a limited range from 0.74 - 1.13 MPa·m$^{1/2}$, being in the range typically exhibited by polycrystalline ceramics (1-5 MPa·m$^{1/2}$ [159, 252]). In addition, in Wang et al.'s work [13] the fracture toughness of LLZO material has been reported as obtained via two different methods: Vickers indentation method and micro-pillar splitting method, yielding in both cases values around 1 MPa·m$^{1/2}$. Hence, overall, the average fracture toughness of LLZO appears to be ~ 1 MPa·m$^{1/2}$ and all measured properties are summarized in Table 4.6.

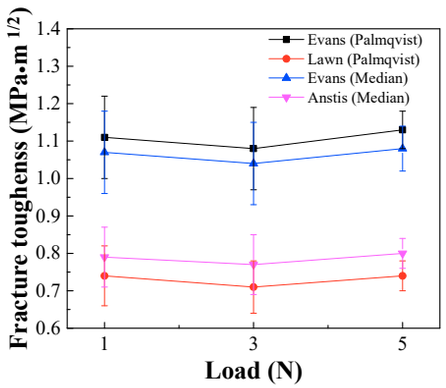

Figure 4.27 K_{IC} calculated as function of load calculated using different equations.

Table 4.6 Mechanical properties of LLZO determined via indentation test.

	E_{IT} (GPa)	H_{IT} (GPa)	K_{IC} (MPa·m$^{1/2}$)
LLZO	117 ± 4	9.4 ± 0.5	~1

Fracture stress and materials' reliability were evaluated based on ROR test at three different loading rates at RT, which permits a consideration of subcritical crack growth effects. A minimum number of 30 specimens is suggested in industrial standards for a Weibull statistical analysis [203, 253], however, limited materials availability did not allow to test such a large

number and hence, although data were analyzed using this statics, results should only be used as indication of the behavior. An initial analysis revealed that characteristic strength values (51, 60 and 53 MPa for 1, 10 and 100 N/min, respectively) as well as Weibull modulus (6, 7 and 8 for 1, 10 and 100 N/min, respectively) were similar for all loading rates. Hence, in order to satisfy the requirements of the industrial standard and to permit an improved derivation, all data were joined for a single Weibull statistic. Fig. 4.28 illustrates the Weibull distribution of the LLZO samples for all loading rates. The data are well described by Weibull statics. Along with characteristic strengths and average fracture stresses also the average elastic modulus of LLZO is listed in Table 4.7.

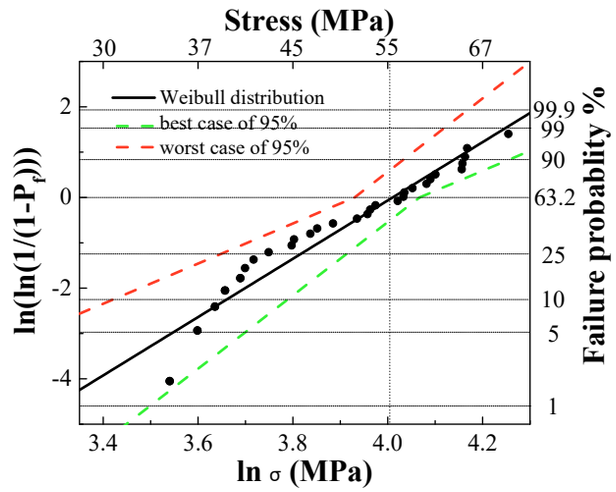

Figure 4.28 Weibull distribution for LLZO.

Table 4.7 Ring-on-ring test results.

	E_{ROR} (GPa)	σ_f (MPa)	σ_0 (MPa)	m
LLZO	67 ± 9	51 ± 11	55 [51 – 58]	6.4 [4.4 – 8.9]

Regarding the elastic modulus, even the highest value obtained from the ROR data is significantly lower than the one obtained via indentation, indicating a strong effect of pores and pores distribution in case of ROR testing. As a result, the properties are considered to be

macroscopic in contrast to indentation test that indicates the local properties and limits the effect of porosity and other flaws. The *m* of 6 is similar to that reported for other ceramics [249]; it was stated that the *m* for ceramics is often in the range of 5-20.

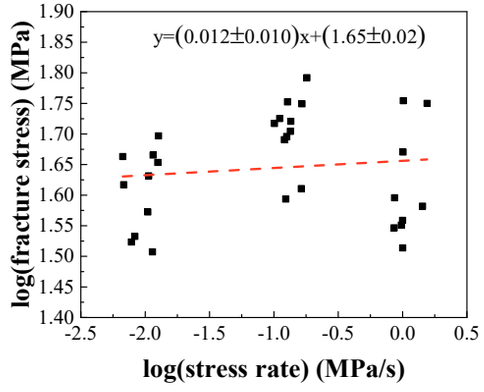

Figure 4.29 Individual fracture stresses of LLZO as a function of loading rates.

Subcritical crack growth sensitivity of LLZO was assessed from ring-on-ring testing with different loading rates. As shown in Fig. 4.29, a line could be fitted to the individual fracture stresses as a function of loading rates. Using the slope, the SCG parameter was calculated. The SCG parameters with the associated uncertainties are summarized in Table 4.8. It has been stated that materials that are sensitive to SCG, such as glasses, have $n < 18$ [155]. Based on Table 4, it can be concluded that LLZO is not very sensitive to subcritical crack growth.

Table 4.8 SCG parameters for LLZO material.

material	*n* parameter	*D* parameter
LLZO	110^{+35}_{-21}	$53.2^{+0.3}_{-0.3}$

Since the SCG sensitivity of LLZO was evaluated, a stress-probability-time diagram could be obtained. Based on the data σ_{1s} = 53 MPa was calculated. Combining σ_{1s} and Eq. (5) and using m = 6, some selected forecast lines are presented in Fig. 4.30. Using this graph, the stress for a

tolerable failure probability can be predicted, yielding for example that the stress should not be higher than 21 MPa for 3 years' lifetime warranting a failure probability of 1%.

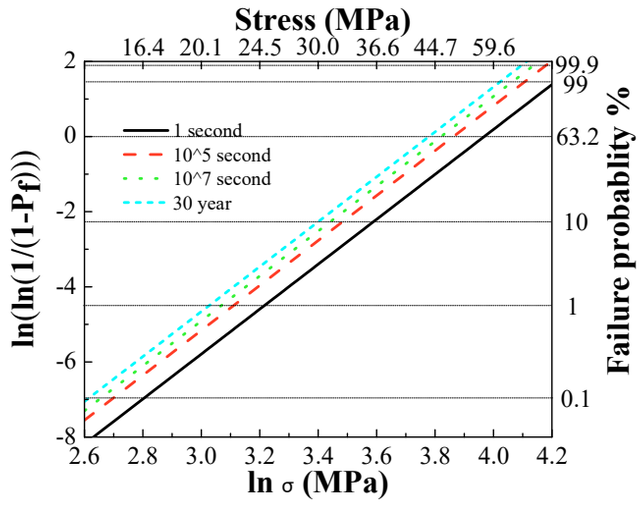

Figure 4.30 Strength-probability-time plots for LLZO.

The fracture surfaces of specimens after bending tests were checked via confocal scanning laser microscopy. As Fig. 4.31 (a) illustrates, LLZO pieces after test were reassembled and then fracture surfaces of individual pieces were analyzed in detail to derive fracture origins. For example, the fracture surface of part 4 and corresponding 3D morphology are shown in Fig. 4.31 (b), where the potential failure origin is indicated. In agreement with occurrence of the highest stress in the bending tests at the surface, the reason of fracture appeared to be pores near the surface. The critical flow size can be calculated according to the Equation 4.2. Based on the fracture stress and fracture toughness an a_c of ~ 180 μm is calculated, being in agreement with the identified fracture origin, which according to Fig. 4.31 (b) has a size of ~ 200 μm.

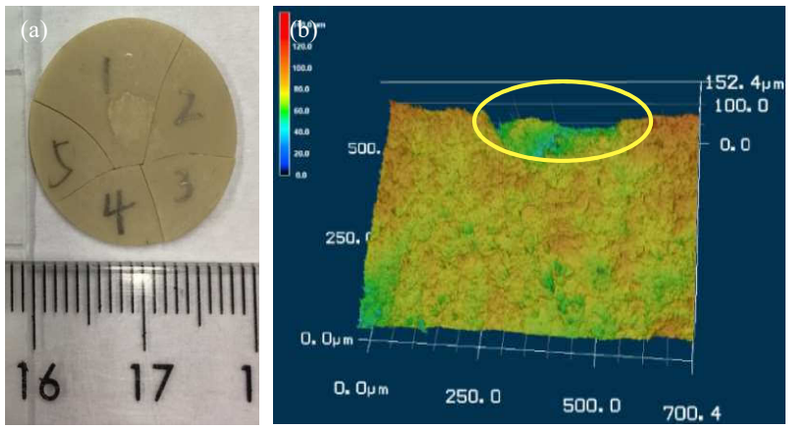

Figure 4.31 Crack surface observation of LLZO. The pieces of the sample after ROR test were reassembled as shown in (a). 3D morphology as well as the fracture surface of part 4 is shown in (b).

Images of a typical fracture surface are displayed in Fig. 4.21 using larger magnifications. The grain sizes distribution is again bimodal, with grain sizes larger than 50 μm and other groups smaller than 10 μm. From Fig. 4.21(a) it can be observed that cracks propagated both intergranular and transgranular, where the transgranular propagation of cracks occurred mostly in big grains. Since the grain boundary strength is relatively high, the crack propagates via the cleavage of the grains. Fig. 4.21(b), being in higher magnification, permits the clearer observation of the crack propagation.

4.3.2.3 Summary

In this part a LLZO (2 mol% Al doping and 40 mol% Ta) possessing pure cubic phase was investigated by indentation and ROR tests regarding its mechanical properties. The subcritical crack growth sensitivity at room temperature was assessed using ROR tests for different loading rates. As might be expected, the local indentation obtained elastic modulus is higher than the global one from ROR test, which can be attributed to a stronger effect of pores and pores distribution. The crack propagation path was both intergranular and transgranular. Fracture stresses show a large scatter reflected in a Weibull modulus of 6, however, the material was not

susceptive to SCG effects. An estimate of a critical defect size based on fracture toughness and strength yields a value of ~ 180 μm being in agreement with the fractographic observation. The stress for a tolerable failure probability is derived; yielding for example that the stress should not exceed 21 MPa for 3 years' lifetime to guarantee a failure probability of 1%. This work provides a basis for further simulation and optimization of batteries applied in demanding working conditions.

4.4 $Li_{0.350}La_{0.557}TiO_3$: Voltage effect on mechanical properties [5]

Electrolytes in all-solid-state lithium batteries are operated under a voltage gradient that potentially induces materials transition, and thus the electrochemical and mechanical stability of electrolyte in operation are vital for such all-solid-state lithium batteries. To simulate the properties of electrolytes under such conditions, as an example material, $Li_{0.350}La_{0.557}TiO_3$ (LLTO) samples were tested at different voltage (usually measured against Li metal (0 V vs. Li/Li^+)). In terms of mechanical behavior, elastic modulus (E), hardness (H) and fracture toughness (K_{IC}) of the as-sintered LLTO, which was 3.2 V and LLTO charged to (and discharged from) 0.2V, 4.0V, and 4.5V, were assessed using indentation methods.

4.4.1 Composition, microstructure and conductivity

The microstructures of LLTO for different charge/discharge state are shown in Fig. 4.32. The SEM image quality is limited since they were obtained under low voltage to avoid acute fluctuation of the samples' potential. It can be seen that the materials are rather dense and the microstructures of the four samples appear to be the same. The grain size of the samples is around 1-2 μm. XRD patterns of the samples are presented in Fig. 4.33. All diffraction peaks of the LLTO-3.2V, LLTO-4.0V and LLTO-4.5V samples are indexed to the cubic structure (PDF#46-0465 $Li_{0.35}La_{0.55}TiO_3$), and no impurity can be observed. The main peaks of the LLTO-0.2V sample are same as for the other samples; however, apparent impurity peaks are indexed to be $LiTiO_2$. The lattice parameters are summarized in Table 4.9. LLTO-3.2V has the largest lattice constant a*, and the lattice constant decreases with increasing voltage, overall, the lattice constant of LLTO-0.2V is smaller than that of LLTO-3.2V. The maximum strain induced by

[5] Section content published: X., Hu, G. Yan et al. Journal of the American Ceramic Society (2019), 102: 1953-1960.

voltage is ~0.10%, related to the maximum change in lattice constant, indicating that the lattice parameter is very stable under different voltages.

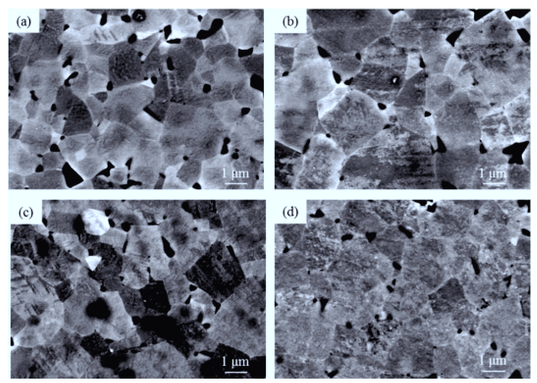

Figure 4.32 SEM images of the samples, (a) LLTO-0.2V, (b) LLTO-3.2V, (c) LLTO-4.0V and (d) LLTO-4.5V.

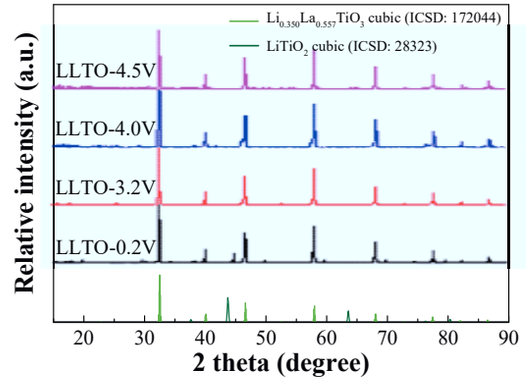

Figure 4.33 XRD patterns of samples with different balance voltage (V vs. Li/Li^+).

Table 4.9 Lattice parameters of samples.

Sample	a^* (Å)
LLTO-0.2V	3.8712 ± 0.0004
LLTO-3.2V	3.8730 ± 0.0001

LLTO-4.0V	3.8704 ± 0.0002
LLTO-4.5V	3.8690 ± 0.0004

The Li-ion conductivities are measured with AC impedance spectroscopy at room temperature (RT). All samples show similar Nyquist plots, as shown in Fig. 4.34. The Nyquist plots consist of a semicircle in the left and a straight line in the right. The intersection of the straight line and the horizontal axis indicates the total (bulk and grain-boundary) resistance (R_{total}). The left intersection of the semicircle and the horizontal axis reflects the bulk resistance (R_b).

The grain-boundary resistance (R_{gb}) is equal to R_{total} - R_b. The bulk and grain boundary conductivities of LLTO-3.2V are 1.65×10^{-3} S·cm^{-1} and 1.01×10^{-4} S·cm^{-1}, respectively. The total conductivity is 9.55×10^{-5} S·cm^{-1}, which is mainly determined by the grain boundaries. Meanwhile, the total conductivity of LLTO-0.2V after discharging, LLTO-4.0V and LLTO-4.5V after charging is 4.86×10^{-5} S·cm^{-1}, 4.32×10^{-5} S·cm^{-1}, and 2.54×10^{-5} S·cm^{-1}, respectively. The Li-ions diffuse via vacancy mechanism and the ion conductivity depends on the V^A concentration and it is reported that perovskites with 8% vacancies within the A-sites have the highest ion conductivity [254]. Here the V^A concentration of LLTO-3.2V is high enough for Li-ions to diffusion.

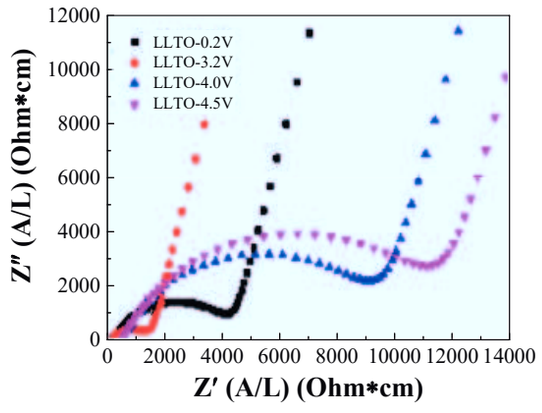

Figure 4.34 Nyquist plots of samples with different balance voltage.

4.4.2 Mechanical properties

Elastic modulus, hardness and fracture toughness are derived via the indentation method. Results are presented in Fig. 4.35. Both *E* and *H* gradually decreased as the depth increases. The fluctuation of the *E* and *H* at low loads can be related to the small volume tested at these loads and effects of inhomogeneity, in particular individual pores [255]. As the load is increased gradually to 500 mN, the elastic and plastic zone increased, where the former is around ten times larger than the plastic zone, yielding average properties that are representative of the bulk. As the load-carrying zone increases, the effect of grain boundaries and especially also voids on the mechanical properties increases, which appear to decrease the apparent properties of the specimens. The *E* and *H* at 20 mN are considered to be representative of the material in the dense state.

The mechanical properties including *E* and *H* at 20 mN as well as K_{IC} at 1 N of LLTO samples at different voltages are displayed in Fig. 4.36. It can be seen that the *E* and *H* of the as-sintered sample LLTO-3.2V is the lowest of 153 GPa and 14.6 GPa, respectively. The deviation of the *E* of LLTO-3.2V is around 12 GPa which is less than 10% of the value indicating that the result is reliable. Overall, as the voltage increases further, the *E* and *H* of the samples increase, as shown in the Fig. 4.38. However, the values for *E* and *H* of LLTO-0.2V are in the level between those of LLTO-3.2V and LLTO-4.5V. For the K_{IC} of all samples yield values around 1 $MPa{\cdot}m^{1/2}$, nevertheless the values exhibit a slight but completely contrary trend to that of the *E* and *H* results. The results indicate that the mechanical properties are sensitive to the Li quantity [15, 17, 170].

It has been found that, as the charge/discharge voltages vary, the mechanical properties of the LLTO material also change. With respect to the lattice parameter and ion conductivity in total, the as sintered material LLTO-3.2V has the highest value, meanwhile the value of the materials decrease as the voltages increase. Since both the conductivity and fracture toughness are proportional to the lattice parameter, the elastic modulus and hardness are inverse proportional to the lattice parameter and hence behave opposite to conductivity and fracture toughness. However, the different behavior of the LLTO-0.2V compared to the other three can be attributed to the reduction of Ti^{4+} to Ti^{3+} and phase decomposition. It indicates that during the design and

optimization of the battery materials or cells the lowest value of the mechanical properties regarding to the voltage variation should be taken into consideration and this also contributes a side of support for monitoring the safety and status of the battery.

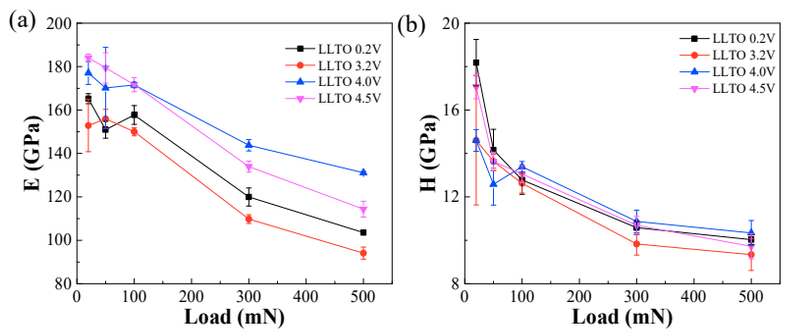

Figure 4.35 Elastic modulus in (a), and hardness in (b) of the samples as a function of load.

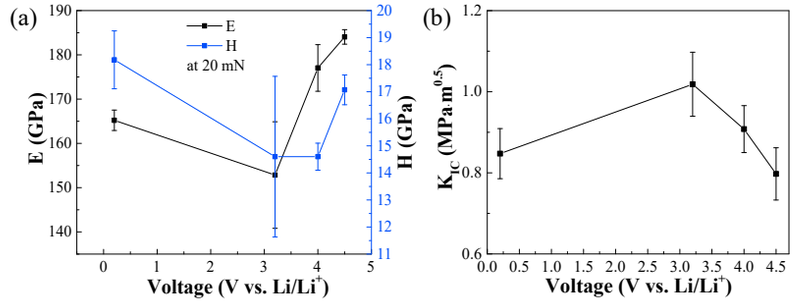

Figure 4.36 Mechanical properties of samples with different balance voltage (V vs. Li/Li^+), (a) elastic modulus (E) and (b) hardness (H) at 20 mN, (c) fracture toughness (K_{IC}).

The fracture surfaces are characterized with SEM (Fig. 4.37). The fracture surfaces of all samples exhibit exclusively a transgranular mode, and have a similar morphology. As the strength of the grain boundaries is relatively high, the crack propagates along the cleavage of the grains. All specimens have dense structures, which is consistent with the relative density.

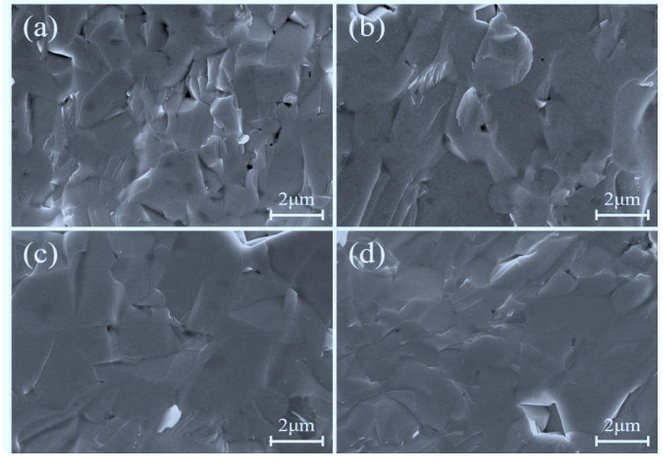

Figure 4.37 SEM images of fracture surfaces, (a) LLTO-0.2V, (b) LLTO-3.2V, (c) LLTO-4.0V, (d) LLTO-4.5V.

4.4.3 Summary

Perovskite electrolyte $Li_{0.350}La_{0.557}TiO_3$ disks were synthesized by the high temperature solid reaction. The voltage of samples (vs. Li/Li^+) is controlled by charging (or discharging) process. LLTO-3.2V, LLTO-4.0V, and LLTO-4.5V exhibited a pure cubic structure, whereas impurity $LiTiO_2$ is observed for LLTO-0.2V. The total ion conductivity of LLTO-3.2 V is 9.55×10^{-5} Scm^{-1}, which was mainly determined by the grain boundary. The E, H and K_{IC} of LLTO at different voltages were tested and the same trend was shown, i.e., since both the conductivity and fracture toughness were proportional to the lattice parameter, the elastic modulus and hardness were inverse proportional to the lattice parameter and hence behave opposite to conductivity and fracture toughness. The E and H of the as-sintered sample LLTO-3.2V are the lowest with 153 GPa and 14.6 GPa, respectively. For the K_{IC} of all samples yield values around 1 $MPa{\cdot}m^{1/2}$, which exhibits a slightly contrary trend to that of the E and H results. This work provides a basis for further simulation and optimization of battery materials and cells in real application.

4.5 Comparison of LATP, LATP:Si, LLZO and LLTO solid electrolytes

In the current work, NASICON type, garnet type and perovskite type ceramic materials, which might be used for solid lithium battery components, were characterized regarding mechanical properties, with associated investigations on microstructure and limited works on electronic properties. For the NASICON type material LATP both temperature and grain orientation effects on the mechanical properties of hot pressing samples were studied separately, whereas the fracture reliability of the tape casting (which is more likely to be the industrial manufacturing process) LATP version mixed with SiO_2 was studied via ball-on-3-ball test. Since LLZO studies exist already in literature the garnet type ceramic LLZO was tested here mainly with ring-on-ring test to predict the lifetime in practical application, complementary indentation testing was carried out. Furthermore, since the solid electrolyte materials experience cycling voltage variation, the perovskite type material LLTO, developed and optimized towards application by an external partner, was selected to research the charge state effect on the mechanical properties derived via indentation testing. A comparison of the properties of these solid electrolyte materials can be seen in Table 4.10.

Table 4.10 Comparison of the selected solid electrolytes' properties.

		σ_t (S/cm)	E_{IT} (GPa)	H_{IT} (GPa)	K_{IC} (MPa·m$^{1/2}$)
LATP	LATP 950 °C	8.69×10^{-5}	118 ± 5	9.3 ± 0.3	-*
	LATP 1000 °C	1.01×10^{-4}	120 ± 6	9.6 ± 0.7	-
	LATP 1050 °C	1.47×10^{-4}	121 ± 7	9.6 ± 0.4	1.4 ± 0.2
	LATP 1100 °C	1.83×10^{-4}	127 ± 10	9.8 ± 0.8	1.6 ± 0.2
LATP:Si	920 °C	2.0×10^{-4}	109 ± 5	8.7 ± 0.4	1.1 ± 0.3
LLZO	1200 °C	8.0×10^{-4}	117 ± 4	9.4 ± 0.5	~1
LLTO	LLTO-0.2V	4.86×10^{-5}	165 ± 2	18.2 ± 1.1	0.8 ± 0.1
	LLTO-3.2V	9.55×10^{-5}	153 ± 12	14.6 ± 3.0	1.0 ± 0.1
	LLTO-4.0V	4.32×10^{-5}	177 ± 5	14.6 ± 0.5	0.9 ± 0.1
	LLTO-4.5V	2.54×10^{-5}	184 ± 2	17.1 ± 0.6	0.8 ± 0.1

*: "-" means the property was not investigated or could not be measured.

Considering that these materials are to be applied as a Li-ion conductor in the lithium battery cell, the ionic conductivity of the materials has to be assessed. It can be seen from the table that the conductivities of these materials are in a similar range and agrees well with literature values as listed in Table 2.2. Compared to conductivity of LiPON and LISICON materials (~ 10^{-6} S/cm) [81, 85-87] the conductivity of the selected materials in this work is evidently higher, which indicates the LATP, LLZO and LLTO are promising solid electrolyte candidates.

As mentioned in section 2.4, elastic modulus, hardness and fracture toughness of LATP are reported to be 81 – 115 GPa, ~7.1 GPa and 1.1 MPa·$m^{1/2}$, respectively [12, 185], and that of the LLZO material are 71-163 GPa, 6.8 - 11.8 GPa and 0.6-1.3 MPa·$m^{1/2}$, respectively [13, 14, 176, 179, 246]. For LLTO reported values are 186 – 200 GPa, 8.4 - 9.7 GPa and 1-1.2 MPa·$m^{1/2}$, respectively [15, 17]. The elastic modulus, hardness and fracture toughness of LATP sintered at different temperatures, LATP:Si, LLZO and LLTO in varied charging state via indentation method all obtained with load control mode are shown in the Table 4.10. It can be seen that the E, H and K_{IC} of the selected materials are in good agreement with the reported results.

The elastic moduli of LATP and LLZO are in a similar range of around 120 GPa, whereas the elastic modulus of LLTO is significantly higher being up to 180 GPa. Similarly, the hardness of LATP and LLZO is both around 9.5 GPa, while the hardness of LLTO material is in the range of 14.6 to 18.2 GPa depending on the charging state. The LLTO material is mainly in cubic crystal structure, whereas the LATP material is in rhombohedral structure and LLZO is in both cubic and tetragonal structure, which results in the higher elastic modulus and hardness of LLTO than that of LATP and LLZO materials. The fracture toughness of LATP samples is higher than that of LLZO and LLTO materials (~ 1 MPa·$m^{1/2}$), whereas the K_{IC} LATP sintered at lower temperature can't be measured due to the indentation-induced crushing. The LATP mixed with SiO_2 was manufactured to investigate the fracture reliability compared to that of pure LATP [12]. As reported in the literature [12], the characteristic fracture stress σ_0 and Weibull modulus m of pure LATP is in the range of 30 to 130 MPa and 5 – 12, respectively. Thus, the addition of SiO_2 is beneficial for improving the fracture reliability of the LATP material. As can be seen in Table 4.10, the elastic modulus and hardness of the hot pressed LATP materials sintered at 950 °C at 30 mN are 118 ± 5 GPa and 9.3 ± 0.3 GPa, respectively. Taking the deviation into consideration,

it can be concluded that the *E* and *H* of LATP:Si sintered at 920 °C are similar like that of LATP 950 °C, which demonstrated that the SiO_2 additive has no distinct effect on the elastic modulus and hardness.

Regarding planar micro-batteries, where the thickness of the electrolyte can be a few microns (with a total unit cell thickness of < 20 μm) [9], the preferred orientations of the electrolyte ought to be selected to achieve better separation and support for the electrodes. LATP material has a rhombohedral crystal structure which potentially behaves anisotropic properties [126, 164]. Thus, the anisotropy of the mechanical properties of LATP sintered at 1100 °C which possessed the highest ionic conductivity was investigated, via indentation method with depth control mode of 300 nm. As shown in Fig. 4.11 the elastic modulus and hardness of LATP 1100 °C is highest at basal plane of 150 ± 3 GPa and 10.0 ± 0.2 GPa, respectively, whereas that of LATP 1100 °C the lowest at prismatic plane of 107 ± 4 GPa and 5.5 ± 0.3 GPa, respectively. Based on the nanoindentation mapping test the average elastic modulus and hardness is calculated as 131 ± 4 GPa and 8.3 ± 0.3 GPa, respectively. This implies the mechanical properties at 30 mN, as shown in Table 10, are close to the average properties, which manifests that it is reasonable that the elastic modulus and hardness of LATP at 30 mN is in between the values of elastic modulus and hardness of LATP basal plane and prismatic plane. The experimental variation tendency of LATP 1100 °C agrees well with the models' prediction. It can be found that the results from load control mode locate in the range of that from depth control mode, which implies that in order to obtain the intrinsic mechanical properties via indentation method low load needs to be applied. The LLTO material is in cubic phase and LLZO material is in mixed cubic and tetragonal phases, which implies the anisotropy effect is not strong on these two materials, nevertheless, their anisotropic mechanical properties might be investigated in future work.

As the fracture strength of pure LATP has been reported by Jackman et al. [12], the tape casting LATP:Si was tested via B3B method to investigate the fracture reliability to see if the mechanical properties can be improved with the SiO_2 binder. In addition, the fracture reliability of LLZO was studied in this work via ROR test since the mechanical properties like elastic modulus, hardness and fracture toughness of LLZO has already been reported [13, 14].

With respect to the LLZO material the elastic modulus via ROR test is calculated as 67 ± 9 GPa, which is significantly lower than the one obtained via indentation, indicating a strong effect of pores and pores distribution in case of ROR testing. Due to the B3B test method limitation the bending elastic modulus of LATP:Si can't be calculated. The Weibull modulus and characteristic fracture strength of LATP:Si and LLZO material are 12.8 and 168 ± 8 MPa, 6.4 and 55 ± 1 MPa, respectively.

The Weibull theory predicts a size effect on strength, i.e. the strength decreased with increasing effective volume. The effective volume of LATP:Si can be calculated via online software [201] as 0.265 mm^3, while the effective volume of LLZO was calculated to be 7.5 mm^3 [139]. As shown in Fig. 4.20 and Fig. 4.31, that the pore inside the sample appearing as the crack origin is similar for both LATP:Si and LLZO materials. Using equation 4.1 the referred fracture strength of LATP:Si and LLZO with 1 mm^3 volume is 151 MPa and 75 MPa, respectively, which indicates potential advantages of the LATP:Si material. It can be seen that the Weibull moduli of LATP:Si and LLZO are in a similar range as for other ceramic materials, i.e. 5 to 20 [249]. The Weibull statistics of LATP:Si and LLZO here can be used as a reference for further LATP and LLZO materials design and as a comparison in probabilistic maximum stress calculations for simulations of components.

Overall, comparing the mechanical results of the materials in this work, it can be found that the LLTO possesses a higher elastic modulus and hardness than the LATP and LLZO material which can be ascribed to the crystal structure difference, whereas the LLTO and LLZO materials possess similar fracture toughness and LATP possesses higher fracture toughness. Regarding to the hot-pressed LATP materials with higher sintering temperature at 1100 °C, the material shows both higher ionic conductivity and mechanical properties. In addition, the orientation effect on the LATP 1100 °C is investigated revealing that both elastic modulus and hardness are higher at basal plane than that at prismatic plane. Results of fracture reliability of tape casting LATP:Si and LLZO materials based on the statistical analysis indicate that the LATP:Si material is more tolerable to fracture behavior than the LLZO material of which the Weibull statistics can be used as reference for future material improvement. Furthermore, the charging state effect on the LLTO material is studied demonstrating that the uptake and release of Li-ion in LLTO

electrolyte can result in the ionic conductivity and mechanical properties variation, which is related to the change in lattice parameter.

5. Conclusions and Outlook

The investigation of the mechanical behavior of solid electrolyte materials is necessary to assisting materials selection and engineering optimization for stabilization of renewable lithium ion batteries. For this purpose, three types of solid electrolytes, NASICON type $Li_{1+x}Al_xTi_{2-x}(PO_4)_3$, garnet type $Li_7La_3Zr_2O_{12}$, perovskite type $Li_{0.33}La_{0.57}TiO_3$, were chosen due to the promising electro-chemical properties. To widen the understanding of the mechanical properties of LATP materials, the hot-pressed LATP materials sintered at various temperatures in the range of 950 °C to 1100 °C were selected to investigate sintering temperature effects. Meanwhile the LATP sintered at 1100 °C, which revealed higher mechanical properties then the other LATP samples, was selected to study the grain orientation effect related to the rhombohedral crystal structure. Since the fracture strength of pure LATP has been reported by Jackman et al. [12], the tape casting LATP:Si was selected here to investigate the fracture reliability and to see if the mechanical properties can be improved with the SiO_2 binder. Since the mechanical properties like elastic modulus, hardness and fracture toughness of LLZO have already been reported [13, 14], the LLZO was chosen here only to investigate the fracture reliability and gain lifetime prediction data. The voltage state effect on the mechanical behavior of LLTO material was also reported in this work due to the intensive promotion and increasing attention regarding the mechanical properties of this material [15-17].

- Sintering temperature effect on mechanical properties of $Li_{1.3}Al_{0.3}Ti_{1.7}(PO_4)_3$ material

With the aim of understanding the temperature effect on the mechanical properties of the $Li_{1.3}Al_{0.3}Ti_{1.7}(PO_4)_3$ material, LATPs sintered at different temperatures (950, 1000, 1050, 1100 °C) were characterized in this work. The grain sizes of the four samples were similar, whereas the amount of secondary phase and density increased as sintering temperature rose. LATP sintered at 1100 °C showed the highest conductivity, 1.83×10^{-4} S/cm, compared to the others. The elastic moduli of the LATP samples were 118 ± 5, 120 ± 6, 121 ± 7 and 127 ± 10 GPa, respectively. The hardness values of LATPs sintered at different temperatures were 9.3 ± 0.3, 9.6 ± 0.7, 9.6 ± 0.4 and 9.8 ± 0.8 GPa, respectively. The higher elastic modulus at low load of LATP sintered at higher temperature was related to the increase of the lattice parameter *c**. The

decreasing of the elastic modulus and hardness with the increasing of load was related mainly to an increase in porosity. The fracture toughness, K_{IC}, of LATP sintered at 1050 and 1100 °C were characterized to be 1.4 ± 0.2 and 1.6 ± 0.2 MPa·m$^{1/2}$, respectively. The value for the LATP sintered at a higher temperature was slightly higher probably again due to the lattice parameter. Obviously to confirm the effect of the porosity on the mechanical measurements assessment of the global properties via use of higher indentation loads or optional impulse excitation or bending tests would be an asset. However, main aim should be to obtain materials in the densest possible state, rendering values obtained at low loads rather important.

- Orientation effect on mechanical properties of $Li_{1.3}Al_{0.3}Ti_{1.7}(PO_4)_3$ material

The anisotropy of the mechanical properties of the solid electrolyte material LATP was investigated in this work via indentation mapping test in a depth control mode at room temperature with associated EBSD characterization. The LATP ceramic electrolyte with a rhombohedral crystal structure was studied and the imprints after indentation were analyzed. For this aim the LATP sintered at 1100 °C, which possessed the highest ionic conductivity, was selected. The experimental elastic moduli and hardness values as a function of rotation angle from basal plane to prismatic plane were assessed and compared with those predicted by the Vlassak-Nix and easy-slip model, respectively, which were used to calculate a theoretical modulus and hardness ratio, respectively. Noticeable anisotropic mechanical properties of LATP material were observed. The experimental elastic modulus and hardness of LATP 1100 °C showed a similar trend, i.e. that the rotation angle $\varphi 2$ between two prismatic $(10\bar{1}0)$ type planes had no detectable influence, whereas when the rotation angle Φ from basal plane to prismatic plane increased, E and H value decrease conspicuously. The comparison of experimental results and theoretical calculation was discussed only in terms of the rotation angle Φ, since the angle Φ appears to be the dominant factor on the mechanical properties of LATP 1100 °C. The experimental indentation modulus fitted well with the prediction of the Vlassak-Nix model, yet the model showed an around 10% higher extremum (118 - 177 GPa) than the experimental results (114 - 160 GPa). The experimental hardness was normalized to compare with the hardness ratio from the easy-slip model and the trend of both results was comparable. Besides, more experimental data points could be gained in future work, especially results around $\Phi = 0°$.

- Fracture reliability of $Li_{1.5}Al_{0.5}Ti_{1.5}P_3O_{12}$:$SiO_2$ material

To assess the fracture reliability of LATP materials, the $Li_{1.5}Al_{0.5}Ti_{1.5}P_3O_{12}$ mixed with SiO_2 was sintered achieving a high density, which allowed reliable investigating of the macroscopic mechanical properties. The elastic modulus and hardness at 30 mN were 109 ± 5 GPa and 8.7 ± 0.4 GPa. Besides, the fracture toughness of LATP:Si 3 N and 5 N were calculated of 1.1 ± 0.3 and 1.2 ± 0.3 MPa·$m^{1/2}$, respectively. The fracture strength， 168 MPa, and Weibull modulus, 13, of LATP:Si had been investigated, which can provide the basis for future macroscopic modeling of LATP components in solid state batteries. The mechanical measurements of LATP:Si demonstrate that an improvement of the mechanical properties can be achieved by densifying the structure and reducing the grain size.

- Fracture reliability of $Li_7La_3Zr_2O_{12}$ material and lifetime prediction

The mechanical properties and further lifetime of $Li_7La_3Zr_2O_{12}$ material are to be understood for simulation and optimization of batteries adopted LLZO applied in demanding working conditions. The LLZO (2 mol% Al doping and 40 mol% Ta) possessing pure garnet phase was investigated by indentation and ROR tests regarding its mechanical properties. The subcritical crack growth sensitivity at room temperature was assessed using ROR tests for different loading rates. The indentation elastic modulus and hardness at 30 mN were 117 ± 4 GPa and 9.4 ± 0.5 GPa, respectively, and the fracture toughness was around 1 MPa·$m^{1/2}$. As might be expected, the local indentation obtained elastic modulus is higher than the global one from ROR test, which can be attributed to a stronger effect of pores and pores distribution. The crack propagation path was both intergranular and transgranular. Fracture stresses show a large scatter reflected in a Weibull modulus of 6, however, the material was not susceptive to SCG effects. An estimate of a critical defect size based on fracture toughness and strength yields a value of ~ 180 µm being in agreement with the fractographic observation. The stress for a tolerable failure probability is derived; yielding for example that the stress should not exceed 21 MPa for 3 years lifetime to guarantee a failure probability of 1%.

- Voltage effect on mechanical properties of $Li_{0.350}La_{0.557}TiO_3$ material

Perovskite electrolyte $Li_{0.350}La_{0.557}TiO_3$ disks were synthesized by the high temperature solid reaction. The voltage of samples (vs. Li/Li^+) is controlled by charging (or discharging) process. LLTO-3.2V, LLTO-4.0V, and LLTO-4.5V exhibited a pure cubic structure, whereas impurity $LiTiO_2$ is observed for LLTO-0.2V. The total ion conductivity of LLTO-3.2 V is 9.55×10^{-5} Scm^{-1}, which was mainly determined by the grain boundary. The *E*, *H* and K_{IC} of LLTO at different voltages were tested and the same trend was shown, i.e., since both the conductivity and fracture toughness were proportional to the lattice parameter, the elastic modulus and hardness were inverse proportional to the lattice parameter and hence behave opposite to conductivity and fracture toughness. The *E* and *H* of the as-sintered sample LLTO-3.2V are the lowest of 153 GPa and 14.6 GPa, respectively. For the K_{IC} of all samples values around 1 $MPa{\cdot}m^{1/2}$ were obtained, exhibiting a slightly contrary trend to that of the *E* and *H* results. These results provide a basis for further simulation and optimization of LLTO in real battery cells application.

Overall, comparing the mechanical results of the materials in this work, it can be concluded that the LLTO possesses a higher elastic modulus and hardness than the LATP and LLZO material, which can be ascribed to the crystal structure difference, whereas the LLTO and LLZO materials possess similar fracture toughness and LATP has higher fracture toughness. The hot-pressed LATP materials with higher sintering temperature of 1100 °C show both higher ionic conductivity and mechanical properties. In addition, the orientation effect on the LATP 1100 °C is investigated revealing that both elastic modulus and hardness are higher at basal plane than that at prismatic plane. Results of fracture reliability of tape casting LATP:Si and LLZO materials based on the statistical analysis indicate that the LATP:Si material is more tolerable to fracture behavior than the LLZO material of which the Weibull statistics can be used as reference for future material improvement. Furthermore, the charging state effect on the LLTO material is studied demonstrating that the uptake and release of Li-ion in LLTO electrolyte can result in the ionic conductivity and mechanical properties variation which is related to the change in lattice parameter. This work deepens comprehension of the mechanical properties of the solid

electrolytes which broadens the application of the materials and provides the data base for further materials development and battery cell advancement.

- Outlook

Collectively, this work provides selected basic mechanical property information of the chosen materials; however, still further investigations are advised addressing the electrolyte materials' mechanical properties which would aid potential application. Sintering effects and materials optimization can be aim of future mechanical characterization in support of materials development. New, promising materials should always be considered in future studies, where also electrodes and their interaction and interface with electrolyte materials in particular after cyclic operation appear to be important aspects.

In order to understand and predict grain orientation effects on mechanical properties of rhombohedral electrolyte material the models should be improved, especially the "easy-slip" model, which would be in particular benefit for the application of the electrolytes in micro-batteries. Combining the improved models, potential anisotropy effects on the electrolyte materials like LLZO, LLTO and other materials might be studied in combination with experimental testing. Furthermore, for practical application, it's favorable to investigate the subcritical crack growth effect as well as the lifetime prediction of the LATP and LLTO.

The micro-pillar splitting method, which receives increasing attention [13, 144, 256, 257], can be used to derive the fracture toughness for not only LATP, LLZO, LLTO on the level of single grains, but also other electrolyte materials. Furthermore, the electrochemical effect on the mechanical properties of electrolyte (the stress and strain variation due to the charge/discharge process) needs to be investigated to deeply understand the failure mechanism of the electrolytes and to help improving the battery monitoring system. Moreover, in practical applications, the battery might be working in conditions below and above room temperature, thus the mechanical properties of electrolytes at different operation relevant temperatures should be of concern.

References

[1] G. Krajačić, N. Duić, Z. Zmijarević, B.V. Mathiesen, A.A. Vučinić, M. da Graça Carvalho, Planning for a 100% independent energy system based on smart energy storage for integration of renewables and CO_2 emissions reduction, Applied thermal engineering, 31 (2011) 2073-2083.
[2] X.-B. Cheng, R. Zhang, C.-Z. Zhao, Q. Zhang, Toward safe lithium metal anode in rechargeable batteries: a review, Chemical reviews, 117 (2017) 10403-10473.
[3] M. Skyllas-Kazacos, M.H. Chakrabarti, S.A. Hajimolana, F.S. Mjalli, M. Saleem, Progress in Flow Battery Research and Development, J. Electrochem. Soc., 158 (2011) R55-R79.
[4] D.L. Wood, J. Li, C. Daniel, Prospects for reducing the processing cost of lithium ion batteries, J. Power Sources, 275 (2015) 234-242.
[5] J.F. Oudenhoven, L. Baggetto, P.H. Notten, All-solid-state lithium-ion microbatteries: a review of various three-dimensional concepts, Advanced Energy Materials, 1 (2011) 10-33.
[6] V. Kharton, F. Marques, A. Atkinson, Transport properties of solid oxide electrolyte ceramics: a brief review, Solid State Ionics, 174 (2004) 135-149.
[7] S. Teng, J. Tan, A. Tiwari, Recent developments in garnet based solid state electrolytes for thin film batteries, Curr. Opin. Solid State Mater. Sci., 18 (2014) 29-38.
[8] A. Barré, B. Deguilhem, S. Grolleau, M. Gérard, F. Suard, D. Riu, A review on lithium-ion battery ageing mechanisms and estimations for automotive applications, J Power Sources, 241 (2013) 680-689.
[9] Y. Wang, B. Liu, Q. Li, S. Cartmell, S. Ferrara, Z.D. Deng, J. Xiao, Lithium and lithium ion batteries for applications in microelectronic devices: A review, J Power Sources, 286 (2015) 330-345.
[10] J. Cannarella, C.B. Arnold, Stress evolution and capacity fade in constrained lithium-ion pouch cells, J Power Sources, 245 (2014) 745-751.
[11] S.-W. Eom, M.-K. Kim, I.-J. Kim, S.-I. Moon, Y.-K. Sun, H.-S. Kim, Life prediction and reliability assessment of lithium secondary batteries, J Power Sources, 174 (2007) 954-958.
[12] S.D. Jackman, R.A. Cutler, Effect of microcracking on ionic conductivity in LATP, J Power Sources, 218 (2012) 65-72.
[13] A.-N. Wang, J.F. Nonemacher, G. Yan, M. Finsterbusch, J. Malzbender, M. Krüger, Mechanical properties of the solid electrolyte Al-substituted $Li_7La_3Zr_2O_{12}$ (LLZO) by utilizing micro-pillar indentation splitting test, J Eur Ceram Soc, (2018).
[14] J.F. Nonemacher, C. Hüter, H. Zheng, J. Malzbender, M. Krüger, R. Spatschek, M. Finsterbusch, Microstructure and properties investigation of garnet structured $Li_7La_3Zr_2O_{12}$ as electrolyte for all-solid-state batteries, Solid State Ionics, 321 (2018) 126-134.
[15] Y.-H. Cho, J. Wolfenstine, E. Rangasamy, H. Kim, H. Choe, J. Sakamoto, Mechanical properties of the solid Li-ion conducting electrolyte: $Li_{0.33}La_{0.57}TiO_3$, Journal of Materials Science, 47 (2012) 5970-5977.
[16] Y. Kong, Y. Li, J. Li, C. Hu, X. Wang, J. Lu, Li ion conduction of perovskite $Li_{0.375}Sr_{0.4375}Ti_{0.25}Ta_{0.75}O_3$ and related compounds, Ceram Int, 44 (2018) 3947-3950.
[17] K.G. Schell, F. Lemke, E.C. Bucharsky, A. Hintennach, M. Hoffmann, Microstructure and mechanical properties of $Li_{0.33}La_{0.567}TiO_3$, Journal of Materials Science, 52 (2017) 2232-2240.
[18] L. Grande, E. Paillard, J. Hassoun, J.B. Park, Y.J. Lee, Y.K. Sun, S. Passerini, B. Scrosati, The lithium/air battery: still an emerging system or a practical reality?, Adv Mater, 27 (2015) 784-800.

[19] S.S. Zhang, Liquid electrolyte lithium/sulfur battery: fundamental chemistry, problems, and solutions, J Power Sources, 231 (2013) 153-162.
[20] Y. Li, F. El Gabaly, T.R. Ferguson, R.B. Smith, N.C. Bartelt, J.D. Sugar, K.R. Fenton, D.A. Cogswell, A.D. Kilcoyne, T. Tyliszczak, Current-induced transition from particle-by-particle to concurrent intercalation in phase-separating battery electrodes, Nat Mater, 13 (2014) 1149.
[21] T.B. Reddy, Linden's handbook of batteries, Mcgraw-hill New York2011.
[22] A. Volta, XVII. On the electricity excited by the mere contact of conducting substances of different kinds. In a letter from Mr. Alexander Volta, FRS Professor of Natural Philosophy in the University of Pavia, to the Rt. Hon. Sir Joseph Banks, Bart. KBPR S, Philosophical transactions of the Royal Society of London, (1800) 403-431.
[23] Y. Wu, Lithium-ion batteries: Fundamentals and Applications, CRC Press2015.
[24] P. Kurzweil, Gaston Planté and his invention of the lead–acid battery—The genesis of the first practical rechargeable battery, J Power Sources, 195 (2010) 4424-4434.
[25] T.A. Edison, Reversible galvanic battery, Google Patents. 678,722 [P], 1901.
[26] E.W. Jungner, Positive electrode for accumulators with constant electrolyte, Google Patents. 692,298 [P], 1902.
[27] T. Sakai, A. Yuasa, H. Ishikawa, H. Miyamura, N. Kuriyama, Nickel-metal hydride battery using microencapsulated alloys, Journal of the Less common Metals, 172 (1991) 1194-1204.
[28] B. Scrosati, History of lithium batteries, J Solid State Electr, 15 (2011) 1623-1630.
[29] J. Sudworth, A. Tiley, Sodium Sulphur Battery, Springer Science & Business Media1985.
[30] J. Sudworth, The sodium/nickel chloride (ZEBRA) battery, J Power Sources, 100 (2001) 149-163.
[31] M.M. Thackeray, C. Wolverton, E.D. Isaacs, Electrical energy storage for transportation—approaching the limits of, and going beyond, lithium-ion batteries, Energy & Environmental Science, 5 (2012) 7854-7863.
[32] K. Xu, S. Zhang, T.R. Jow, W. Xu, C.A. Angell, LiBOB as salt for lithium-ion batteries: a possible solution for high temperature operation, Electrochemical and Solid-State Letters, 5 (2002) A26-A29.
[33] V.G. Kumar, N. Munichandraiah, A. Shukla, Electrode impedance parameters and internal resistance of a sealed LiC/$Li_{1-x}CoO_2$ lithium-ion rechargeable battery, Journal of applied electrochemistry, 27 (1997) 43-49.
[34] R. Gummow, A. De Kock, M. Thackeray, Improved capacity retention in rechargeable 4 V lithium/lithium-manganese oxide (spinel) cells, Solid State Ionics, 69 (1994) 59-67.
[35] A.K. Padhi, K.S. Nanjundaswamy, J.B. Goodenough, Phospho-olivines as positive-electrode materials for rechargeable lithium batteries, J Electrochem Soc, 144 (1997) 1188-1194.
[36] N. Yabuuchi, T. Ohzuku, Novel lithium insertion material of $LiCo_{1/3}Ni_{1/3}Mn_{1/3}O_2$ for advanced lithium-ion batteries, J Power Sources, 119 (2003) 171-174.
[37] S. Ferrari, E. Quartarone, P. Mustarelli, A. Magistris, M. Fagnoni, S. Protti, C. Gerbaldi, A. Spinella, Lithium ion conducting PVdF-HFP composite gel electrolytes based on N-methoxyethyl-N-methylpyrrolidinium bis(trifluoromethanesulfonyl)-imide ionic liquid, J Power Sources, 195 (2010) 559-566.
[38] J. Chen, Recent progress in advanced materials for lithium ion batteries, Materials, 6 (2013) 156-183.
[39] M.S. Whittingham, Lithium batteries and cathode materials, Chemical reviews, 104 (2004) 4271-4302.

[40] S.B. Peterson, J. Apt, J. Whitacre, Lithium-ion battery cell degradation resulting from realistic vehicle and vehicle-to-grid utilization, J Power Sources, 195 (2010) 2385-2392.
[41] H. Okamoto, S. Hikazudani, C. Inazumi, T. Takeuchi, M. Tabuchi, K. Tatsumi, Upper voltage and temperature dependencies for an all-solid-state In/LiCoO(2) cell using sulfide glass electrolyte, Electrochem Solid St, 11 (2008) A97-A100.
[42] M.R. Palacin, A. de Guibert, Why do batteries fail?, Science, 351 (2016) 574-+.
[43] T. Jansen, D. Blass, S. Hartwig, K. Dilger, Processing of Advanced Battery Materials—Laser Cutting of Pure Lithium Metal Foils, Batteries, 4 (2018) 37.
[44] Y. Kato, S. Hori, T. Saito, K. Suzuki, M. Hirayama, A. Mitsui, M. Yonemura, H. Iba, R. Kanno, High-power all-solid-state batteries using sulfide superionic conductors, Nature Energy, 1 (2016) 16030.
[45] C.A. Vincent, Lithium batteries: a 50-year perspective, 1959–2009, Solid State Ionics, 134 (2000) 159-167.
[46] K.A. Cook-Chennault, N. Thambi, A.M. Sastry, Powering MEMS portable devices—a review of non-regenerative and regenerative power supply systems with special emphasis on piezoelectric energy harvesting systems, Smart materials and structures, 17 (2008) 043001.
[47] J. Xu, B.H. Liu, D.Y. Hu, State of Charge Dependent Mechanical Integrity Behavior of 18650 Lithium-ion Batteries, Sci Rep-Uk, 6 (2016).
[48] P. Poizot, S. Laruelle, S. Grugeon, L. Dupont, J. Tarascon, Nano-sized transition-metal oxides as negative-electrode materials for lithium-ion batteries, Nature, 407 (2000) 496.
[49] N. Anurova, V. Blatov, G. Ilyushin, O. Blatova, A. Ivanov-Schitz, L. Dem'yanets, Migration maps of Li+ cations in oxygen-containing compounds, Solid State Ionics, 179 (2008) 2248-2254.
[50] J.W. Fergus, Ceramic and polymeric solid electrolytes for lithium-ion batteries, J Power Sources, 195 (2010) 4554-4569.
[51] J. Song, Y. Wang, C.C.J.J.o.p.s. Wan, Review of gel-type polymer electrolytes for lithium-ion batteries, 77 (1999) 183-197.
[52] S.S.J.J.o.P.S. Zhang, A review on electrolyte additives for lithium-ion batteries, 162 (2006) 1379-1394.
[53] J.M. Tarascon, A.S. Gozdz, C. Schmutz, F. Shokoohi, P.C. Warren, Performance of Bellcore's plastic rechargeable Li-ion batteries, Solid State Ionics, 86-88 (1996) 49-54.
[54] Z. Ren, Y.Y. Liu, K.N. Sun, X.L. Zhou, N.Q. Zhang, A microporous gel electrolyte based on poly(vinylidene fluoride-co-hexafluoropropylene)/fully cyanoethylated cellulose derivative blend for lithium-ion battery, Electrochim Acta, 54 (2009) 1888-1892.
[55] P. Raghavan, X.H. Zhao, J.K. Kim, J. Manuel, G.S. Chauhan, J.H. Ahn, C. Nah, Ionic conductivity and electrochemical properties of nanocomposite polymer electrolytes based on electrospun poly(vinylidene fluoride-co-hexafluoropropylene) with nano-sized ceramic fillers, Electrochim Acta, 54 (2008) 228-234.
[56] Z. Ren, K.N. Sun, Y.Y. Liu, X.L. Zhou, N.Q. Zhang, X.D. Zhu, Polymer electrolytes based on poly(vinylidene fluoride-co-hexafluoropropylene) with crosslinked poly(ethylene glycol) for lithium batteries, Solid State Ionics, 180 (2009) 693-697.
[57] H.P. Zhang, P. Zhang, G.C. Li, Y.P. Wu, D.L. Sun, A porous poly(vinylidene fluoride) gel electrolyte for lithium ion batteries prepared by using salicylic acid as a foaming agent, J Power Sources, 189 (2009) 594-598.
[58] R.Y. Miao, B.W. Liu, Z.Z. Zhu, Y. Liu, J.L. Li, X.D. Wang, Q.F. Li, PVDF-HFP-based porous polymer electrolyte membranes for lithium-ion batteries, J Power Sources, 184 (2008) 420-426.

[59] C. Sirisopanaporn, A. Fernicola, B. Scrosati, New, ionic liquid-based membranes for lithium battery application, J Power Sources, 186 (2009) 490-495.
[60] N. Shukla, A.K. Thakur, Role of salt concentration on conductivity optimization and structural phase separation in a solid polymer electrolyte based on PMMA-LiClO4, Ionics, 15 (2009) 357-367.
[61] M.S. Su'ait, A. Ahmad, M.Y.A. Rahman, Ionic conductivity studies of 49% poly(methyl methacrylate)-grafted natural rubber-based solid polymer electrolytes, Ionics, 15 (2009) 497-500.
[62] Hekselman, M. Kalita, A. Plewa-Marczewska, G.Z. Zukowska, E. Sasim, W. Wieczorek, M. Siekierski, Effect of calix[6]pyrrole anion receptor addition on properties of PEO-based solid polymer electrolytes doped with LiTf and LiTfSI salts, Electrochim Acta, 55 (2010) 1298-1307.
[63] C.B. Zhu, H. Cheng, Y. Yang, Electrochemical characterization of two types of PEO-based polymer electrolytes with room-temperature ionic liquids, J Electrochem Soc, 155 (2008) A569-A575.
[64] K.K. Kumar, M. Ravi, Y. Pavani, S. Bhavani, A. Sharma, V.N. Rao, Investigations on the effect of complexation of NaF salt with polymer blend (PEO/PVP) electrolytes on ionic conductivity and optical energy band gaps, Physica B: Condensed Matter, 406 (2011) 1706-1712.
[65] T. Uno, S. Kawaguchi, M. Kubo, T. Itoh, Ionic conductivity and thermal property of solid hybrid polymer electrolyte composed of oligo (ethylene oxide) unit and butyrolactone unit, J Power Sources, 178 (2008) 716-722.
[66] Z. Bakenov, M. Nakayama, M. Wakihara, I. Taniguchi, Lithium AlPO4 composite polymer battery with nanostructured LiMn2O4 cathode, J Solid State Electr, 12 (2008) 295-302.
[67] T. Niitani, M. Amaike, H. Nakano, K. Dokko, K. Kanamura, Star-Shaped Polymer Electrolyte with Microphase Separation Structure for All-Solid-State Lithium Batteries, J Electrochem Soc, 156 (2009) A577-A583.
[68] Z. Jiang, B. Carroll, K.M. Abraham, Studies of some poly(vinylidene fluoride) electrolytes, Electrochim Acta, 42 (1997) 2667-2677.
[69] Y.H. Liang, W.B. Cheng-Chien, C.Y. Chen, Comb-like copolymer-based gel polymer electrolytes for lithium ion conductors, J Power Sources, 176 (2008) 340-346.
[70] L.Z. Fan, X.L. Wang, F. Long, X. Wang, Enhanced ionic conductivities in composite polymer electrolytes by using succinonitrile as a plasticizer, Solid State Ionics, 179 (2008) 1772-1775.
[71] H. Pitawala, M. Dissanayake, V. Seneviratne, B.-E. Mellander, I. Albinson, Effect of plasticizers (EC or PC) on the ionic conductivity and thermal properties of the $(PEO)_9LiTf$: Al_2O_3 nanocomposite polymer electrolyte system, J Solid State Electr, 12 (2008) 783-789.
[72] A. Hayashi, K. Noi, A. Sakuda, M. Tatsumisago, Superionic glass-ceramic electrolytes for room-temperature rechargeable sodium batteries, Nat Commun, 3 (2012) 856.
[73] V. Thangadurai, W. Weppner, Recent progress in solid oxide and lithium ion conducting electrolytes research, Ionics, 12 (2006) 81-92.
[74] V. Thangadurai, W. Weppner, Solid state lithium ion conductors: Design considerations by thermodynamic approach, Ionics, 8 (2002) 281-292.
[75] P. Knauth, Inorganic solid Li ion conductors: An overview, Solid State Ionics, 180 (2009) 911-916.
[76] A. Ivanov-Shitz, Computer simulation of superionic conductors: II. Cationic conductors. Review, Crystallography Reports, 52 (2007) 302-315.

[77] J. Oudenhoven, R. Vullers, R. Van Schaijk, A review of the present situation and future developments of micro-batteries for wireless autonomous sensor systems, Int J Energ Res, 36 (2012) 1139-1150.
[78] Y. Xiayin, H. Bingxin, Y. Jingyun, P. Gang, H. Zhen, G. Chao, L. Deng, X. Xiaoxiong, All-solid-state lithium batteries with inorganic solid electrolytes: Review of fundamental science, Chinese Physics B, 25 (2016) 018802.
[79] N. Dudney, Glass and ceramic electrolytes for lithium and lithium-ion batteries, Lithium Batteries, Springer2009, pp. 624-642.
[80] J. Tong, D. Clark, M. Hoban, R. O'Hayre, Cost-effective solid-state reactive sintering method for high conductivity proton conducting yttrium-doped barium zirconium ceramics, Solid State Ionics, 181 (2010) 496-503.
[81] X. Yu, J. Bates, G. Jellison, F. Hart, A stable thin-film lithium electrolyte: lithium phosphorus oxynitride, J Electrochem Soc, 144 (1997) 524-532.
[82] T. Minami, A. Hayashi, M. Tatsumisago, Recent progress of glass and glass-ceramics as solid electrolytes for lithium secondary batteries, Solid State Ionics, 177 (2006) 2715-2720.
[83] K. Minami, A. Hayashi, S. Ujiie, M. Tatsumisago, Structure and properties of Li_2S–P_2S_5–P_2S_3 glass and glass–ceramic electrolytes, J Power Sources, 189 (2009) 651-654.
[84] M. Tatsumisago, F. Mizuno, A. Hayashi, All-solid-state lithium secondary batteries using sulfide-based glass–ceramic electrolytes, J Power Sources, 159 (2006) 193-199.
[85] R. Kanno, M. Maruyama, Lithium ionic conductor thio-LISICON - The Li_2S-GeS_2-P_2S_5 system, J Electrochem Soc, 148 (2001) A742-A746.
[86] R. Kanno, T. Hata, Y. Kawamoto, M. Irie, Synthesis of a new lithium ionic conductor, thio-LISICON-lithium germanium sulfide system, Solid State Ionics, 130 (2000) 97-104.
[87] Z.Q. Liu, F.Q. Huang, J.H. Yang, B.F. Wang, J.K. Sun, New lithium ion conductor, thio-LISICON lithium zirconium sulfide system, Solid State Ionics, 179 (2008) 1714-1716.
[88] J. Goodenough, H.-P. Hong, J. Kafalas, Fast Na^+-ion transport in skeleton structures, Materials Research Bulletin, 11 (1976) 203-220.
[89] H. Aono, E. Sugimoto, Y. Sadaoka, N. Imanaka, G.-y. Adachi, Ionic conductivity and sinterability of lithium titanium phosphate system, Solid State Ionics, 40 (1990) 38-42.
[90] X. Xu, Z. Wen, X. Yang, L. Chen, Dense nanostructured solid electrolyte with high Li-ion conductivity by spark plasma sintering technique, Materials Research Bulletin, 43 (2008) 2334-2341.
[91] A.M. Cruz, E.B. Ferreira, A.C.M. Rodrigues, Controlled crystallization and ionic conductivity of a nanostructured $LiAlGePO_4$ glass–ceramic, Journal of Non-Crystalline Solids, 355 (2009) 2295-2301.
[92] H. Kasper, Series of rare earth garnets $Ln^{3+\,3}M_2Li^{+3}O_{12}$ (M= Te, W), Inorg Chem, 8 (1969) 1000-1002.
[93] V. Thangadurai, W. Weppner, $Li_6ALa_2Nb_2O_{12}$ (A= Ca, Sr, Ba): A New Class of Fast Lithium Ion Conductors with Garnet-Like Structure, J Am Ceram Soc, 88 (2005) 411-418.
[94] V. Thangadurai, J. Schwenzel, W. Weppner, Tailoring ceramics for specific applications: a case study of the development of all-solid-state lithium batteries, Ionics, 11 (2005) 11-23.
[95] R. Murugan, V. Thangadurai, W. Weppner, Fast lithium ion conduction in garnet-type $Li_7La_3Zr_2O_{12}$, Angewandte Chemie International Edition, 46 (2007) 7778-7781.
[96] X. Yao, B. Huang, J. Yin, G. Peng, Z. Huang, C. Gao, D. Liu, X. Xu, All-solid-state lithium batteries with inorganic solid electrolytes: Review of fundamental science, Chinese Phys B, 25 (2015) 018802.

[97] C.A. Geiger, E. Alekseev, B. Lazic, M. Fisch, T. Armbruster, R. Langner, M. Fechtelkord, N. Kim, T. Pettke, W. Weppner, Crystal chemistry and stability of "$Li_7La_3Zr_2O_{12}$" garnet: a fast lithium-ion conductor, Inorg Chem, 50 (2010) 1089-1097.
[98] R. Murugan, S. Ramakumar, N. Janani, High conductive yttrium doped $Li_7La_3Zr_2O_{12}$ cubic lithium garnet, Electrochemistry Communications, 13 (2011) 1373-1375.
[99] M. Catti, M. Sommariva, R.M. Ibberson, Tetragonal superstructure and thermal history of $Li_{0.3}La_{0.567}TiO_3$ (LLTO) solid electrolyte by neutron diffraction, Journal of Materials Chemistry, 17 (2007) 1300-1307.
[100] M. Catti, Local structure of the $Li_{1/8}La_{5/8}TiO_3$ (LLTO) ionic conductor by theoretical simulations, Journal of Physics: Conference Series, IOP Publishing, 2008, pp. 012008.
[101] Y. Inaguma, C. Liquan, M. Itoh, T. Nakamura, T. Uchida, H. Ikuta, M. Wakihara, High ionic conductivity in lithium lanthanum titanate, Solid State Commun, 86 (1993) 689-693.
[102] O. Bohnke, The fast lithium-ion conducting oxides $Li_{3x}La_{2/3-x}TiO_3$ from fundamentals to application, Solid State Ionics, 179 (2008) 9-15.
[103] W. Lee, J.W. Han, Y. Chen, Z. Cai, B. Yildiz, Cation size mismatch and charge interactions drive dopant segregation at the surfaces of manganite perovskites, J Am Chem Soc, 135 (2013) 7909-7925.
[104] Y. Kimura, T. Kushi, S.i. Hashimoto, K. Amezawa, T. Kawada, Influences of temperature and oxygen partial pressure on mechanical properties of $La_{0.6}Sr_{0.4}Co_{1-y}Fe_yO_{3-\delta}$, J Am Ceram Soc, 95 (2012) 2608-2613.
[105] A. Kumar, D. Leonard, S. Jesse, F. Ciucci, E.A. Eliseev, A.N. Morozovska, M.D. Biegalski, H.M. Christen, A. Tselev, E. Mutoro, Spatially resolved mapping of oxygen reduction/evolution reaction on solid-oxide fuel cell cathodes with sub-10 nm resolution, Acs Nano, 7 (2013) 3808-3814.
[106] N. Balke, S. Jesse, A. Morozovska, E. Eliseev, D. Chung, Y. Kim, L. Adamczyk, R. Garcia, N. Dudney, S. Kalinin, Nanoscale mapping of ion diffusion in a lithium-ion battery cathode, Nature Nanotechnology, 5 (2010) 749.
[107] S. Bishop, D. Marrocchelli, C. Chatzichristodoulou, N.H. Perry, M.B. Mogensen, H. Tuller, E. Wachsman, Chemical expansion: implications for electrochemical energy storage and conversion devices, Annual Review of Materials Research, 44 (2014) 205-239.
[108] W.H. Woodford, W.C. Carter, Y.-M. Chiang, Design criteria for electrochemical shock resistant battery electrodes, Energy & Environmental Science, 5 (2012) 8014-8024.
[109] T. Ohzuku, M. Kitagawa, T. Hirai, Electrochemistry of Manganese Dioxide in Lithium Nonaqueous Cell III. X-Ray Diffractional Study on the Reduction of Spinel-Related Manganese Dioxide, J Electrochem Soc, 137 (1990) 769-775.
[110] W. Zhang, D. Schröder, T. Arlt, I. Manke, R. Koerver, R. Pinedo, D.A. Weber, J. Sann, W.G. Zeier, J. Janek, (Electro) chemical expansion during cycling: monitoring the pressure changes in operating solid-state lithium batteries, J Mater Chem A, 5 (2017) 9929-9936.
[111] G. Bucci, Y.-M. Chiang, W.C. Carter, Formulation of the coupled electrochemical–mechanical boundary-value problem, with applications to transport of multiple charged species, Acta Mater, 104 (2016) 33-51.
[112] G. Bucci, T. Swamy, Y.-M. Chiang, W.C. Carter, Modeling of internal mechanical failure of all-solid-state batteries during electrochemical cycling, and implications for battery design, J Mater Chem A, 5 (2017) 19422-19430.
[113] X.-W. Zhang, Y. Li, S.A. Khan, P.S. Fedkiw, Inhibition of lithium dendrites by fumed silica-based composite electrolytes, J Electrochem Soc, 151 (2004) A1257-A1263.

[114] C.-L. Tsai, V. Roddatis, C.V. Chandran, Q. Ma, S. Uhlenbruck, M. Bram, P. Heitjans, O. Guillon, $Li_7La_3Zr_2O_{12}$ interface modification for Li dendrite prevention, Acs Appl Mater Inter, 8 (2016) 10617-10626.
[115] F. Orsini, A. Du Pasquier, B. Beaudoin, J. Tarascon, M. Trentin, N. Langenhuizen, E. De Beer, P. Notten, In situ scanning electron microscopy (SEM) observation of interfaces within plastic lithium batteries, J Power Sources, 76 (1998) 19-29.
[116] C. Monroe, J. Newman, Dendrite growth in lithium/polymer systems a propagation model for liquid electrolytes under galvanostatic conditions, J Electrochem Soc, 150 (2003) A1377-A1384.
[117] C. Monroe, J. Newman, The impact of elastic deformation on deposition kinetics at lithium/polymer interfaces, J Electrochem Soc, 152 (2005) A396-A404.
[118] R. Raj, J. Wolfenstine, Current limit diagrams for dendrite formation in solid-state electrolytes for Li-ion batteries, J Power Sources, 343 (2017) 119-126.
[119] G. Anstis, P. Chantikul, B.R. Lawn, D. Marshall, A critical evaluation of indentation techniques for measuring fracture toughness: I, direct crack measurements, J Am Ceram Soc, 64 (1981) 533-538.
[120] K. Kerman, A. Luntz, V. Viswanathan, Y.-M. Chiang, Z. Chen, practical challenges hindering the development of solid state Li ion batteries, J Electrochem Soc, 164 (2017) A1731-A1744.
[121] L. Porz, T. Swamy, B.W. Sheldon, D. Rettenwander, T. Frömling, H.L. Thaman, S. Berendts, R. Uecker, W.C. Carter, Y.M. Chiang, Mechanism of lithium metal penetration through inorganic solid electrolytes, Advanced Energy Materials, 7 (2017).
[122] X. Xiao, P. Liu, M.W. Verbrugge, H. Haftbaradaran, H. Gao, Improved cycling stability of silicon thin film electrodes through patterning for high energy density lithium batteries, Journal of Power Sources, 196 (2011) 1409-1416.
[123] H. Wu, G. Chan, J.W. Choi, I. Ryu, Y. Yao, M.T. McDowell, S.W. Lee, A. Jackson, Y. Yang, L. Hu, Stable cycling of double-walled silicon nanotube battery anodes through solid–electrolyte interphase control, Nature nanotechnology, 7 (2012) 310.
[124] K. Zhao, M. Pharr, J.J. Vlassak, Z. Suo, Fracture of electrodes in lithium-ion batteries caused by fast charging, J Appl Phys, 108 (2010) 073517.
[125] H. Neuber, Theory of stress concentration for shear-strained prismatical bodies with arbitrary nonlinear stress-strain law, Journal of applied mechanics, 28 (1961) 544-550.
[126] M.E. Stevenson, M. Kaji, R.C. Bradt, Microhardness anisotropy and the indentation size effect on the basal plane of single crystal hematite, J Eur Ceram Soc, 22 (2002) 1137-1148.
[127] V. Srikar, S.M. Spearing, A critical review of microscale mechanical testing methods used in the design of microelectromechanical systems, Experimental mechanics, 43 (2003) 238-247.
[128] W.C. Oliver, G.M. Pharr, An Improved Technique for Determining Hardness and Elastic-Modulus Using Load and Displacement Sensing Indentation Experiments, J Mater Res, 7 (1992) 1564-1583.
[129] I.M. Meththananda, S. Parker, M.P. Patel, M. Braden, The relationship between Shore hardness of elastomeric dental materials and Young's modulus, Dental materials, 25 (2009) 956-959.
[130] G. Pharr, Measurement of mechanical properties by ultra-low load indentation, Materials Science and Engineering: A, 253 (1998) 151-159.
[131] G. Pharr, W. Oliver, Measurement of thin film mechanical properties using nanoindentation, Mrs Bull, 17 (1992) 28-33.

[132] J. Wei, G. Pećanac, J. Malzbender, Review of mechanical characterization methods for ceramics used in energy technologies, Ceram Int, 40 (2014) 15371-15380.
[133] M.L. Palmeri, K.R. Nightingale, Acoustic radiation force-based elasticity imaging methods, Interface focus, 1 (2011) 553-564.
[134] R.G. Parr, R.G. Pearson, Absolute hardness: companion parameter to absolute electronegativity, J Am Chem Soc, 105 (1983) 7512-7516.
[135] N.X. Randall, Direct measurement of residual contact area and volume during the nanoindentation of coated materials as an alternative method of calculating hardness, Philosophical Magazine A, 82 (2002) 1883-1892.
[136] Z. Peng, J. Gong, H. Miao, On the description of indentation size effect in hardness testing for ceramics: Analysis of the nanoindentation data, Journal of the European Ceramic Society, 24 (2004) 2193-2201.
[137] X.-K. Zhu, J.A. Joyce, Review of fracture toughness (G, K, J, CTOD, CTOA) testing and standardization, Engineering Fracture Mechanics, 85 (2012) 1-46.
[138] D.J. Green, An introduction to the mechanical properties of ceramics, Cambridge university press1998.
[139] C.H. Wang, Introduction to fracture mechanics, DSTO Aeronautical and Maritime Research Laboratory Melbourne, Australia1996.
[140] W.E. Schiesser, G.W. Griffiths, A compendium of partial differential equation models: method of lines analysis with Matlab, Cambridge University Press2009.
[141] D. Uhlmann, H.K. Bowen, W. Kingery, Introduction to Ceramics, New York: John Wiley & Sons Inc, 1976.
[142] D. Taylor, P. Cornetti, N. Pugno, The fracture mechanics of finite crack extension, Engineering Fracture Mechanics, 72 (2005) 1021-1038.
[143] J.P. Best, J. Zechner, J.M. Wheeler, R. Schoeppner, M. Morstein, J. Michler, Small-scale fracture toughness of ceramic thin films: the effects of specimen geometry, ion beam notching and high temperature on chromium nitride toughness evaluation, Philos Mag, 96 (2016) 3552-3569.
[144] R. Maass, S. Van Petegem, J. Zimmermann, C. Borca, H. Van Swygenhoven, On the initial microstructure of metallic micropillars, Scripta Mater, 59 (2008) 471-474.
[145] D. Ćorić, L. Ćurković, M. Majić Renjo, Statistical analysis of vickers indentation fracture toughness of Y-TZP ceramics, Transactions of FAMENA, 41 (2017) 1-16.
[146] B.R. Lawn, E. Fuller, Equilibrium penny-like cracks in indentation fracture, Journal of Materials Science, 10 (1975) 2016-2024.
[147] A.G. EVans, E.A. Charles, Fracture toughness determinations by indentation, J Am Ceram Soc, 59 (1976) 371-372.
[148] K. Niihara, R. Morena, D.P.H. Hasselman, Evaluation ofKIc of brittle solids by the indentation method with low crack-to-indent ratios, Journal of Materials Science Letters, 1 (1982) 13-16.
[149] B.R. Lawn, A. Evans, D. Marshall, Elastic/plastic indentation damage in ceramics: the median/radial crack system, J Am Ceram Soc, 63 (1980) 574-581.
[150] K. Tanaka, Elastic/plastic indentation hardness and indentation fracture toughness: the inclusion core model, Journal of Materials Science, 22 (1987) 1501-1508.
[151] A. Evans, T.R. Wilshaw, Quasi-static solid particle damage in brittle solids—I. Observations analysis and implications, Acta Metallurgica, 24 (1976) 939-956.

[152] K. Niihara, A fracture mechanics analysis of indentation-induced Palmqvist crack in ceramics, J. Mater. Sci. Lett., 2 (1983) 221-223.
[153] K. Niihara, R. Morena, D. Hasselman, Evaluation ofK Ic of brittle solids by the indentation method with low crack-to-indent ratios, Journal of Materials Science Letters, 1 (1982) 13-16.
[154] M. Gruber, I. Kraleva, P. Supancic, J. Bielen, D. Kiener, R. Bermejo, Strength distribution and fracture analyses of $LiNbO_3$ and $LiTaO_3$ single crystals under biaxial loading, J Eur Ceram Soc, 37 (2017) 4397-4406.
[155] S.R. Choi, J.A. Salem, F.A. Holland, Estimation of slow crack growth parameters for constant stress-rate test data of advanced ceramics and glass by the individual data and arithmetic mean methods, (1997).
[156] H. Rinne, The Weibull distribution: a handbook, Chapman and Hall/CRC2008.
[157] Y. Zhang, M. Inoue, N. Uchida, K. Uematsu, Characterization of processing pores and their relevance to the strength in alumina ceramics, J Mater Res, 14 (1999) 3370-3374.
[158] E. DIN, 843-5: 2007-03:„Hochleistungskeramik-Mechanische Eigenschaften monolithischer Keramik bei Raumtemperatur-Teil 5: Statistische Auswertung “, Deutsche Fassung EN, (2006) 843-845.
[159] M. Barsoum, M. Barsoum, Fundamentals of ceramics, CRC press2002.
[160] N. Nagabhushana, T. Nithyanantham, S. Bandopadhyay, J. Zhang, Subcritical Crack Growth Behavior of A Perovskite-Type Oxygen Transport Ceramic Membrane, International Journal of Applied Ceramic Technology, 8 (2011) 390-397.
[161] A. Sakuda, A. Hayashi, Y. Takigawa, K. Higashi, M. Tatsumisago, Evaluation of elastic modulus of Li_2S-P_2S_5 glassy solid electrolyte by ultrasonic sound velocity measurement and compression test, Journal of the Ceramic Society of Japan, 121 (2013) 946-949.
[162] G. Fehringer, S. Janes, M. Wildersohn, R. Clasen, Proton—conducting ceramics as electrode/electrolyte—materials for SOFCs: Preparation, mechanical and thermal-mechanical properties of thermal sprayed coatings, material combination and stacks, J Eur Ceram Soc, 24 (2004) 705-715.
[163] J. Snow, A. Heuer, Slip systems in Al_2O_3, J Am Ceram Soc, 56 (1973) 153-157.
[164] J.J. Vlassak, W. Nix, Measuring the elastic properties of anisotropic materials by means of indentation experiments, Journal of the Mechanics and Physics of Solids, 42 (1994) 1223-1245.
[165] S.I. Ranganathan, M. Ostoja-Starzewski, Universal elastic anisotropy index, Phys Rev Lett, 101 (2008) 055504.
[166] Z. Deng, Z. Wang, I.-H. Chu, J. Luo, S.P. Ong, Elastic properties of alkali superionic conductor electrolytes from first principles calculations, J Electrochem Soc, 163 (2016) A67-A74.
[167] S.A. Uhland, R.K. Holman, S. Morissette, M.J. Cima, E.M. Sachs, Strength of green ceramics with low binder content, J Am Ceram Soc, 84 (2001) 2809-2818.
[168] W.-K. Shin, D.-W. Kim, High performance ceramic-coated separators prepared with lithium ion-containing SiO_2 particles for lithium-ion batteries, J Power Sources, 226 (2013) 54-60.
[169] G. Yan, S. Yu, J.F. Nonemacher, H. Tempel, H. Kungl, J. Malzbender, R.-A. Eichel, M. Krüger, Influence of sintering temperature on conductivity and mechanical behavior of the solid electrolyte LATP, Ceram Int, 45 (2019) 14697-14703.
[170] X. Hu, X. Cheng, S. Qin, G. Yan, J. Malzbender, W. Qiang, B. Huang, Mechanical and electrochemical properties of cubic and tetragonal $Li_xLa_{0.557}TiO_3$ perovskite oxide electrolytes, Ceram Int, 44 (2018) 1902-1908.

[171] K.-Y. Yang, I.-C. Leu, K.-Z. Fung, M.-H. Hon, M.-C. Hsu, Y.-J. Hsiao, M.-C. Wang, Mechanism of the interfacial reaction between cation-deficient La0.56Li0.33TiO3 and metallic lithium at room temperature, Journal of Materials Research, 23 (2008) 1813-1825.
[172] J.-L. Le, Z.P. Bažant, M.Z. Bazant, Subcritical crack growth law and its consequences for lifetime statistics and size effect of quasibrittle structures, Journal of Physics D: Applied Physics, 42 (2009) 214008.
[173] F.P. McGrogan, T. Swamy, S.R. Bishop, E. Eggleton, L. Porz, X. Chen, Y.M. Chiang, K.J. Van Vliet, Compliant Yet Brittle Mechanical Behavior of Li_2S–P_2S_5 Lithium-Ion-Conducting Solid Electrolyte, Advanced Energy Materials, 7 (2017) 1602011.
[174] Z. Wang, M. Wu, G. Liu, X. Lei, B. Xu, C. Ouyang, Elastic properties of new solid state electrolyte material $Li_{10}GeP_2S_{12}$: A study from first-principles calculations, Int. J. Electrochem. Sci, 9 (2014) 562-568.
[175] E.G. Herbert, W.E. Tenhaeff, N.J. Dudney, G.M. Pharr, Mechanical characterization of LiPON films using nanoindentation, Thin Solid Films, 520 (2011) 413-418.
[176] A. Sharafi, C.G. Haslam, R.D. Kerns, J. Wolfenstine, J. Sakamoto, Controlling and correlating the effect of grain size with the mechanical and electrochemical properties of $Li_7La_3Zr_2O_{12}$ solid-state electrolyte, J Mater Chem A, 5 (2017) 21491-21504.
[177] J.E. Ni, E.D. Case, J.S. Sakamoto, E. Rangasamy, J.B. Wolfenstine, Room temperature elastic moduli and Vickers hardness of hot-pressed LLZO cubic garnet, Journal of Materials Science, 47 (2012) 7978-7985.
[178] Y. Kim, H. Jo, J.L. Allen, H. Choe, J. Wolfenstine, J. Sakamoto, G. Pharr, The Effect of Relative Density on the Mechanical Properties of Hot-Pressed Cubic $Li_7La_3Zr_2O_{12}$, J. Am. Ceram. Soc., 99 (2016) 1367-1374.
[179] J. Wolfenstine, H. Jo, Y.-H. Cho, I.N. David, P. Askeland, E.D. Case, H. Kim, H. Choe, J. Sakamoto, A preliminary investigation of fracture toughness of $Li_7La_3Zr_2O_{12}$ and its comparison to other solid Li-ionconductors, Mater Lett, 96 (2013) 117-120.
[180] C. Cooper, A.C. Sutorik, J. Wright, E.A. Luoto, G. Gilde, J. Wolfenstine, Mechanical Properties of Hot Isostatically Pressed $Li_{0.35}La_{0.55}TiO_3$, Advanced Engineering Materials, 16 (2014) 755-759.
[181] Y. Kim, H. Jo, J.L. Allen, H. Choe, J. Wolfenstine, J. Sakamoto, The Effect of Relative Density on the Mechanical Properties of Hot-Pressed Cubic $Li_7La_3Zr_2O_{12}$, J Am Ceram Soc, 99 (2016) 1367-1374.
[182] S. Yu, R.D. Schmidt, R. Garcia-Mendez, E. Herbert, N.J. Dudney, J.B. Wolfenstine, J. Sakamoto, D.J. Siegel, Elastic Properties of the Solid Electrolyte $Li_7La_3Zr_2O_{12}$ (LLZO), Chem. Mater., 28 (2016) 197-206.
[183] J.J. Gilman, The plastic resistance of crystals, Australian Journal of Physics, 13 (1960) 327.
[184] W. CALLISTER Jr, Fundamentals of Materials Science and Engineering: An Integrated Approach. New York: John Wiley&Sons, Inc, 2005.
[185] S.D. Jackman, R.A. Cutler, Stability of NaSICON-type $Li_{1.3}Al_{0.3}Ti_{1.7}P_3O_{12}$ in aqueous solutions, J Power Sources, 230 (2013) 251-260.
[186] S. Yu, A. Mertens, X. Gao, D.C. Gunduz, R. Schierholz, S. Benning, F. Hausen, J. Mertens, H. Kungl, H. Tempel, Influence of microstructure and AlPO4 secondary-phase on the ionic conductivity of $Li_{1.3}Al_{0.3}Ti_{1.7}(PO_4)_3$ solid-state electrolyte, Functional Materials Letters, 9 (2016) 1650066.

[187] Q. Ma, Q. Xu, C.-L. Tsai, F. Tietz, O. Guillon, A Novel Sol–Gel Method for Large-Scale Production of Nanopowders: Preparation of Li1.5Al0.5Ti1.5(PO4)3 as an Example, Journal of the American Ceramic Society, 99 (2016) 410-414.
[188] W. Zhou, Z.L. Wang, Scanning microscopy for nanotechnology: techniques and applications, Springer science & business media2007.
[189] S. Nishikawa, S. Kikuchi, Diffraction of cathode rays by calcite, Nature, 122 (1928) 726.
[190] A.J. Schwartz, M. Kumar, B.L. Adams, D.P. Field, Electron backscatter diffraction in materials science, Springer2000.
[191] L. Reimer, Scanning electron microscopy: physics of image formation and microanalysis, Springer2013.
[192] R.T. DeHoff, F.N. Rhines, Quantitative microscopy, (1968).
[193] E. Broitman, Indentation hardness measurements at macro-, micro-, and nanoscale: a critical overview, Tribology Letters, 65 (2017) 23.
[194] B. Poon, D. Rittel, G. Ravichandran, An analysis of nanoindentation in linearly elastic solids, International Journal of Solids and Structures, 45 (2008) 6018-6033.
[195] F. Sergejev, M. Antonov, Comparative study on indentation fracture toughness measurements of cemented carbides, Proc. Estonian Acad. Sci. Eng, 12 (2006) 388-398.
[196] S. Vachhani, R. Doherty, S. Kalidindi, Effect of the continuous stiffness measurement on the mechanical properties extracted using spherical nanoindentation, Acta Mater, 61 (2013) 3744-3751.
[197] K. Siu, A. Ngan, The continuous stiffness measurement technique in nanoindentation intrinsically modifies the strength of the sample, Philos Mag, 93 (2013) 449-467.
[198] G. de With, H.H. Wagemans, Ball-on-ring test revisited, J Am Ceram Soc, 72 (1989) 1538-1541.
[199] R. Danzer, W. Harrer, P. Supancic, T. Lube, Z. Wang, A. Börger, The ball on three balls test—Strength and failure analysis of different materials, J Eur Ceram Soc, 27 (2007) 1481-1485.
[200] A. Börger, P. Supancic, R. Danzer, The ball on three balls test for strength testing of brittle discs: stress distribution in the disc, J Eur Ceram Soc, 22 (2002) 1425-1436.
[201] R. Bermejo, P. Supancic, I. Kraleva, R. Morrell, R. Danzer, Strength reliability of 3D low temperature co-fired multilayer ceramics under biaxial loading, J Eur Ceram Soc, 31 (2011) 745-753.
[202] A. Börger, P. Supancic, R. Danzer, The ball on three balls test for strength testing of brittle discs: Part II: analysis of possible errors in the strength determination, J Eur Ceram Soc, 24 (2004) 2917-2928.
[203] C. ASTM, 1239-07: Standard practice for reporting uniaxial strength data and estimating Weibull distribution parameters for advanced ceramics, West Conshohocken: ASTM International, (2007).
[204] G. Pećanac, S. Foghmoes, M. Lipińska-Chwałek, S. Baumann, T. Beck, J. Malzbender, Strength degradation and failure limits of dense and porous ceramic membrane materials, J Eur Ceram Soc, 33 (2013) 2689-2698.
[205] A. Standard, C1499-05,"Standard Test Method for Monotonic Equibiaxial Flexural Strength of Advanced Ceramics at Ambient Temperature", ASTM International, West Conshohocken, PA, (2005).
[206] J. Vlassak, M. Ciavarella, J. Barber, X. Wang, The indentation modulus of elastically anisotropic materials for indenters of arbitrary shape, Journal of the Mechanics and Physics of Solids, 51 (2003) 1701-1721.

[207] J. Wachtman Jr, W. Tefft, D. Lam Jr, R. Stinchfield, Elastic Constants of Synthetic Single-Crystal Corundum at Room Temperature, J Am Ceram Soc, 43 (1960) 334-334.
[208] T. Csanádi, M. Bl'anda, N.Q. Chinh, P. Hvizdoš, J. Dusza, Orientation-dependent hardness and nanoindentation-induced deformation mechanisms of WC crystals, Acta Mater, 83 (2015) 397-407.
[209] T. Csanádi, D. Németh, J. Dusza, Z. Lenčéš, P. Šajgalík, Nanoindentation induced deformation anisotropy in β-Si_3N_4 ceramic crystals, J Eur Ceram Soc, 36 (2016) 3059-3066.
[210] B. Lang, B. Ziebarth, C. Elsässer, Lithium ion conduction in $LiTi_2(PO_{4)3}$ and related compounds based on the NASICON structure: a first-principles study, Chem Mater, 27 (2015) 5040-5048.
[211] M. Kronberg, Plastic deformation of single crystals of sapphire: basal slip and twinning, Acta Metallurgica, 5 (1957) 507-524.
[212] R. Nowak, T. Sekino, S. Maruno, K. Niihara, Deformation of sapphire induced by a spherical indentation on the (1010) plane, Appl Phys Lett, 68 (1996) 1063-1065.
[213] J. Clayton, Modeling finite deformations in trigonal ceramic crystals with lattice defects, International Journal of Plasticity, 26 (2010) 1357-1386.
[214] H. Siemes, B. Klingenberg, E. Rybacki, M. Naumann, W. Schäfer, E. Jansen, K. Kunze, Glide systems of hematite single crystals in deformation experiments, Ore Geol Rev, 33 (2008) 255-279.
[215] M. Jabbari, R. Bulatova, A. Tok, C. Bahl, E. Mitsoulis, J.H. Hattel, Ceramic tape casting: a review of current methods and trends with emphasis on rheological behaviour and flow analysis, Materials Science and Engineering: B, 212 (2016) 39-61.
[216] B. Key, D.J. Schroeder, B.J. Ingram, J.T. Vaughey, Solution-based synthesis and characterization of lithium-ion conducting phosphate ceramics for lithium metal batteries, Chem Mater, 24 (2012) 287-293.
[217] R. Kali, A. Mukhopadhyay, Spark plasma sintered/synthesized dense and nanostructured materials for solid-state Li-ion batteries: Overview and perspective, J Power Sources, 247 (2014) 920-931.
[218] S. Soman, Y. Iwai, J. Kawamura, A. Kulkarni, Crystalline phase content and ionic conductivity correlation in LATP glass–ceramic, J Solid State Electr, 16 (2012) 1761-1766.
[219] S. Duluard, A. Paillassa, L. Puech, P. Vinatier, V. Turq, P. Rozier, P. Lenormand, P.-L. Taberna, P. Simon, F. Ansart, Lithium conducting solid electrolyte $Li_{1.3}Al_{0.3}Ti_{1.7}(PO_4)_3$ obtained via solution chemistry, J Eur Ceram Soc, 33 (2013) 1145-1153.
[220] R.O. Silva, J. Malzbender, F. Schulze-Küppers, S. Baumann, O. Guillon, Mechanical properties and lifetime predictions of dense $SrTi_{1-x}Fe_xO_{3-\delta}$ (x= 0.25, 0.35, 0.5), J Eur Ceram Soc, 37 (2017) 2629-2636.
[221] J. Magdeski, The porosity dependence of mechanical properties of sintered alumina, Journal of the University of Chemical Technology and Metallurgy, 45 (2010) 143-148.
[222] Y. Zou, J. Malzbender, Development and optimization of porosity measurement techniques, Ceram Int, 42 (2016) 2861-2870.
[223] Q. Peng, B. Yang, L. Liu, C. Song, B. Friedrich, Porous TiAl alloys fabricated by sintering of TiH_2 and Al powder mixtures, J Alloy Compd, 656 (2016) 530-538.
[224] R. Spriggs, Effect of Open and Closed Pores on Elastic Moduli of Polycrystalline Ahmina, J Am Ceram Soc, 45 (1962) 454-454.
[225] M. Liu, B. Shi, J. Guo, X. Cai, H. Song, Lattice constant dependence of elastic modulus for ultrafine grained mild steel, Scripta Mater, 49 (2003) 167-171.

[226] W. Son, H. Gao, T. Duong, A. Talapatra, M. Radovic, R. Arróyave, Effect of A mixing on elastic modulus, cleavage stress, and shear stress in the $Ti_3(Si_xAl_{1-x})C_2$ MAX phase, Phys Rev B, 95 (2017) 235131.
[227] V. Shpakov, J. Tse, V. Belosludov, R. Belosludov, Elastic moduli and instability in molecular crystals, Journal of Physics: Condensed Matter, 9 (1997) 5853.
[228] Y. Zhou, B. Liu, Theoretical investigation of mechanical and thermal properties of MPO_4 (M= Al, Ga), J Eur Ceram Soc, 33 (2013) 2817-2821.
[229] J. Wolfenstine, J. Allen, J. Read, J. Sakamoto, G. Gonalez-Doncel, Hot-pressed $Li_{0.33}La_{0.57}TiO_3$, J Power Sources, 195 (2010) 4124-4128.
[230] D. Labonte, A.-K. Lenz, M.L. Oyen, On the relationship between indentation hardness and modulus, and the damage resistance of biological materials, Acta biomaterialia, 57 (2017) 373-383.
[231] X.-Q. Chen, H. Niu, D. Li, Y. Li, Modeling hardness of polycrystalline materials and bulk metallic glasses, Intermetallics, 19 (2011) 1275-1281.
[232] R. Chaim, M. Hefetz, Effect of grain size on elastic modulus and hardness of nanocrystalline ZrO_2- 3 wt% Y_2O_3 ceramic, Journal of materials science, 39 (2004) 3057-3061.
[233] J.W. Anthony, Handbook of mineralogy: Arsenates, phosphates, vanadates. arsenates, phosphates, vanadates, Mineral Data Pub.2000.
[234] K. HIROTA, R.C. BRADT, THE MICROHARDNESS INDENTATION SIZE/LOAD EFFECT (ISE) IN SINGLE-CRYSTAL, BERLINITE, Advanced Materials' 93, I, Elsevier1994, pp. 441-444.
[235] G. Chin, J. Wernick, T. Geballe, S. Mahajan, S. Nakahara, Hardness and bounding in A 15 superconducting compounds, Appl Phys Lett, 33 (1978) 103-105.
[236] J.J. Gilman, Chemistry and physics of mechanical hardness, John Wiley & Sons2009.
[237] M.E. Launey, R.O. Ritchie, On the fracture toughness of advanced materials, Adv Mater, 21 (2009) 2103-2110.
[238] R. Rice, Grain size and porosity dependence of ceramic fracture energy and toughness at 22 C, Journal of materials science, 31 (1996) 1969-1983.
[239] J.-F. Yang, G.-J. Zhang, T. Ohji, Porosity and microstructure control of porous ceramics by partial hot pressing, J Mater Res, 16 (2001) 1916-1918.
[240] M. Pérez-Estébanez, J. Isasi-Marín, D. Többens, A. Rivera-Calzada, C. León, A systematic study of Nasicon-type $Li_{1+x}MxTi_{2-x}(PO_4)_3$ (M: Cr, Al, Fe) by neutron diffraction and impedance spectroscopy, Solid State Ionics, 266 (2014) 1-8.
[241] H. Aono, E. Sugimoto, Y. Sadaaka, N. Imanaka, G.J.J.o.t.E.S. Adachi, Ionic conductivity of the lithium titanium phosphate (Li/sub 1+ x/M/sub x/Ti/sub 2-x/(PO/sub 4/)/sub 3/, M= Al, Sc, Y, and La) systems, 136 (1989) 590.
[242] P.J. Withers, H. Bhadeshia, Residual stress. Part 2–Nature and origins, Materials science and technology, 17 (2001) 366-375.
[243] C. Boissiere, D. Grosso, S. Lepoutre, L. Nicole, A.B. Bruneau, C. Sanchez, Porosity and mechanical properties of mesoporous thin films assessed by environmental ellipsometric porosimetry, Langmuir, 21 (2005) 12362-12371.
[244] C. Yada, Y. Iriyama, T. Abe, K. Kikuchi, Z. Ogumi, A novel all-solid-state thin-film-type lithium-ion battery with in situ prepared positive and negative electrode materials, Electrochemistry Communications, 11 (2009) 413-416.

[245] D. Rettenwander, A. Welzl, S. Pristat, F. Tietz, S. Taibl, G. Redhammer, J. Fleig, A microcontact impedance study on NASICON-type $Li_{1+x}Al_xTi_{2-x}(PO_4)_3$ ($0 \leq x \leq 0.5$) single crystals, J Mater Chem A, 4 (2016) 1506-1513.
[246] J. Wolfenstine, J.L. Allen, J. Sakamoto, D.J. Siegel, H. Choe, Mechanical behavior of Li-ion-conducting crystalline oxide-based solid electrolytes: a brief review, Ionics, (2017) 1-6.
[247] G.R. Anstis, P. Chantikul, B.R. Lawn, D.B. Marshall, A Critical Evaluation of Indentation Techniques for Measuring Fracture Toughness: I, Direct Crack Measurements, J. Am. Ceram. Soc., 64 (1981) 533-538.
[248] C. Badini, P. Fino, A. Ortona, C. Amelio, High temperature oxidation of multilayered SiC processed by tape casting and sintering, J Eur Ceram Soc, 22 (2002) 2071-2079.
[249] C.B. Carter, M.G. Norton, Ceramic materials: science and engineering, Springer Science & Business Media2007.
[250] C.-L. Tsai, E. Dashjav, E.-M. Hammer, M. Finsterbusch, F. Tietz, S. Uhlenbruck, H.P. Buchkremer, High conductivity of mixed phase Al-substituted $Li_7La_3Zr_2O_{12}$, Journal of electroceramics, 35 (2015) 25-32.
[251] J. Gong, J. Wu, Z. Guan, Examination of the indentation size effect in low-load Vickers hardness testing of ceramics, J Eur Ceram Soc, 19 (1999) 2625-2631.
[252] Y.-M. Chiang, D.P. Birnie, W.D. Kingery, S. Newcomb, Physical ceramics: principles for ceramic science and engineering, Wiley New York1997.
[253] K. Jakus, D. Coyne, J. Ritter, Analysis of fatigue data for lifetime predictions for ceramic materials, Journal of Materials Science, 13 (1978) 2071-2080.
[254] S. García-Martín, M.A. Alario-Franco, H. Ehrenberg, J. Rodríguez-Carvajal, U. Amador, Crystal Structure and Microstructure of Some La2/3-xLi3xTiO3 Oxides: An Example of the Complementary Use of Electron Diffraction and Microscopy and Synchrotron X-ray Diffraction To Study Complex Materials, Journal of the American Chemical Society, 126 (2004) 3587-3596.
[255] B.R. Lawn, K. Jakus, A.C. Gonzalez, Sharp vs blunt crack hypotheses in the strength of glass: a critical study using indentation flaws, J Am Ceram Soc, 68 (1985) 25-34.
[256] F. Östlund, P.R. Howie, R. Ghisleni, S. Korte, K. Leifer, W.J. Clegg, J. Michler, Ductile–brittle transition in micropillar compression of GaAs at room temperature, Philos Mag, 91 (2011) 1190-1199.
[257] P.R. Howie, S. Korte, W.J. Clegg, Fracture modes in micropillar compression of brittle crystals, J Mater Res, 27 (2012) 141-151.

Acknowledgement

I would like to thank Prof. Dr. Lorenz Singheiser for providing me the great conditions and opportunities to work in the Institute of Energy and Climate Research, Microstructure and Properties of Materials (IEK-2), Forschungszentrum Jülich GmbH. Then I would like to express my appreciation to all the people helping the doctoral thesis accomplish. Especially express many thanks to Prof. Dr. Manja Krüger for the support on the thesis. I also appreciate the China Scholarship Council (CSC) of China for granting a studentship (201606400064).

The deep and sincere appreciation goes to Dr. Jürgen Malzbender for the constant encouragements, careful corrections, inspiring discussions and continuous contribution to the activities within the project during my whole PhD period. My honest gratitude is for Dr. Ying Zou, who kindly provides me the excellent support at the beginning of my career here.

Many thanks to all the colleagues and co-workers for introductions and consistent support of the experimental equipment: Dr. Egbert Wessel and Dr. Daniel Grüner for the comprehensive SEM and EBSD studies, Mr. Mirko Ziegner for the high-quality XRD measurement campaigns, Mr. Volker Gutzeit and Mr. Jörg Bartsch for the important support in metallographic treatment, Dr. D. Guenduez for the EDS investigation, Ms. Tatjana Osipova for the continuous vital support in ROR test, Prof. Dr. Raul Bermejo and Dr. Irina Kraleva for the support in B3B test and the fracture surface analysis, Dr. D. Guenduez for compositional analysis for LATP EDS studies.

Furthermore, I would like to thank all partners cooperated for the wonderful work, particularly for Prof. Dr. Bingxin Huang from USTB for providing the LLTO samples, Dr. Shicheng Yu from IEK-9 for supplying the LATP samples, Dr. Martin Finsterbusch and Dr. Hao Zheng from IEK-1 for offering the LLZO samples, Dr. Enkhtsetseg Dashjav from IEK-1 for furnishing the LATP:Si samples,.

I would also like to say many thanks to my group colleagues who played an important role in the scientific everyday life: Dr. Juliane Nonemacher, Dr. Jianping Wei, Dr. Rafael Oliveira Silva, Dr. Xiaoyan Yin, Sebastian von Helden, Vahid Ebrahimzade, Masood Fakouri Hasanabadi, Xiuru Fan, Shuo Fu, Fanlin Zeng, Wenyu Zhou, Xiaoqiang Li, Jürgen gross.

Above all, I would like to explain my profound gratitude to my family and my friends, especially Meiqi Niu, for their constant caring, support and encouragement.

List of Publications

Nonemacher, J. F., Arinicheva, Y., **Yan, G.**, Finsterbusch, M., Krüger, M., & Malzbender, J.. Fracture toughness of single grains and polycrystalline $Li_7La_3Zr_2O_{12}$ electrolyte material based on a pillar splitting method. Journal of the European Ceramic Society (2020), 40, 3057-3064.

Dashjav, E., Gellert, M., **Yan, G.**, Grüner, D., Kaiser, N., Spannenberger, S., ... & Malzbender, J. Microstructure, ionic conductivity and mechanical properties of tape-cast $Li_{1.5}Al_{0.5}Ti_{1.5}P_3O_{12}$ electrolyte sheets. Journal of the European Ceramic Society (2020), 40, 1975-1982.

Yan, G., Yu, S., Yang, W., Li, X., Tempel, H., Kungl, H., Eichel, R.A., Krüger, M. & Malzbender, J.. Anisotropy of the mechanical properties of $Li_{1.3}Al_{0.3}Ti_{1.7}(PO_4)_3$ solid electrolyte material. Journal of Power Sources (2019), 437, 226940.

Yan, G., Nonemacher, J. F., Zheng, H., Finsterbusch, M., Malzbender, J., & Krüger, M.. An investigation on strength distribution, subcritical crack growth and lifetime of the lithium-ion conductor $Li_7La_3Zr_2O_{12}$. Journal of Materials Science (2019), 54(7), 5671-5681.

Meng, D., **Yan, G.**, Yue, W., Lin, F., & Wang, C.. Effect of high temperature annealing on ultrahard polycrystalline diamond in air and vacuum conditions. International Journal of Refractory Metals and Hard Materials (2019), 78, 340-349.

Hu, X., **Yan, G.**, Cheng, X., Malzbender, J., Qiang, W., & Huang, B.. Electrochemical and mechanical stability of $Li_xLa_{0.557}TiO_{3-\delta}$ perovskite electrolyte at various voltages. Journal of the American Ceramic Society (2019), 102(4), 1953-1960. (Co-first author)

Yan, G., Yu, S., Nonemacher, J. F., Temple, H., Kungl, H., Malzbender, J. & Krüger, M.. Effect of the sintering temperature on conductivity and mechanical properties of the solid electrolyte LATP. Ceramics International (2019), 45, 14697-14703.

Hu, X., Cheng, X., Qin, S., **Yan, G.**, Malzbender, J., Qiang, W., & Huang, B.. Mechanical and electrochemical properties of cubic and tetragonal $Li_xLa_{0.557}TiO_3$ perovskite oxide electrolytes. Ceramics International (2018), 44(2), 1902-1908.

Meng, D., **Yan, G.**, Yue, W., Lin, F., & Wang, C.. Thermal damage mechanisms of Si-coated diamond powder based polycrystalline diamond. Journal of the European Ceramic Society (2018), 38(13), 4338-4345.

Wang, A. N., Nonemacher, J. F., **Yan, G.**, Finsterbusch, M., Malzbender, J., & Krüger, M.. Mechanical properties of the solid electrolyte Al-substituted $Li_7La_3Zr_2O_{12}$ (LLZO) by utilizing micro-pillar indentation splitting test. Journal of the European Ceramic Society (2018), 38(9), 3201-3209.

G. Yan, A. Wang, H. Zheng, J. F. Nonemacher, M. Finsterbusch, J. Malzbender, Mechanical properties of LLZO solid electrolytes for battery application (Poster). 15th Conference and Exhibition of the European Ceramic Society, Budapest, Hungary, 2017.

Abstract

All solid-state lithium-ion batteries (ASSLIBs) being based on solid state electrolytes are at present regarded as a promising alternative for conventional batteries on account of their higher ionic conductivity, energy density as well as higher chemical stability and safety. The solid electrolytes are expected to possess enhanced ionic conductivity and in addition a mechanical stability that warrants a safer separation of electrodes and is envisaged to permit them to withstand long-term cycling operation. However, in contrast to the widely investigated electro-chemical properties of solid electrolytes, the mechanical properties, which are important for long-term reliability, need to be studied deeper. Hence, the main aim of this work is the mechanical characterization of respective ceramic materials as candidates for solid electrolytes and the relationship to materials' microstructures. For this purpose three types of solid electrolytes, NASICON type $Li_{1+x}Al_xTi_{2-x}(PO_4)_3$ (LATP), garnet type $Li_7La_3Zr_2O_{12}$ (LLZO), perovskite type $Li_{0.350}La_{0.557}TiO_3$ (LLTO), were chosen due to their previously verified promising electro-chemical properties.

With the aim of understanding the mechanical properties of the LATP material, LATPs sintered at different temperatures (950 – 1100 °C) were characterized via indentation method in this work. The results revealed that LATP sintered at higher temperature possesses higher elastic modulus, hardness and fracture toughness. The anisotropy of the mechanical properties of the solid electrolyte material LATP sintered at 1100 °C was investigated in this work via indentation mapping test in a depth control mode at room temperature with associated EBSD characterization. The experimentally derived elastic modulus and hardness of LATP show similar trends, i.e. that the rotation angle between two prismatic type planes had no detectable influence, whereas when the rotation angle from basal plane to prismatic plane increased, elastic modulus and hardness value decrease conspicuously.

Furthermore, to assess the fracture reliability of electrolytes, $Li_{1.5}Al_{0.5}Ti_{1.5}P_3O_{12}$ mixed with SiO_2 (LATP:Si) and a LLZO material were selected to investigate the macroscopic mechanical properties, concentrating on fracture strength and Weibull modulus. The Weibull moduli of LATP:Si and LLZO are in a similar range as for other ceramic materials, whereas the fracture

strength of LATP:Si is higher than that of LLZO, which indicates potential advantages of the LATP:Si material. Due to materials availability the stress for a tolerable failure probability was only derived for the LLZO electrolyte; yielding for example that the stress should not exceed 21 MPa for 3 years lifetime to guarantee a failure probability of 1%.

As the electrolytes in all-solid-state lithium batteries are to be operated under cyclic voltage condition that are associated with chemical expansion effects, exemplified for LLTO, a material being close to application, voltage effects on mechanical properties were studied. Elastic modulus, hardness and fracture toughness of LLTO at different voltages were tested, revealing the same trend, i.e., both conductivity and fracture toughness were proportional to the lattice parameter, elastic modulus and hardness were inversely proportional to the lattice parameter and hence behave opposite to conductivity and fracture toughness.

Overall, the investigation of the effects of sintering temperature, grain orientation and charge state on the mechanical behavior of the electrolytes as well as the fracture reliability study aid an understanding of the mechanical properties of the materials and provide a data base for further improvement of design and processing of battery materials and cells.

Kurzfassung

Li-Ionen Gesamtfestkörperbatterien (ASSLIBs) basierend auf Festkörperelektrolyten werden derzeit als vielversprechende Alternative zu konventionellen Batterien angesehen, sowohl aufgrund ihrer höheren ionischen Leitfähigkeit und Energiedichte als auch ihrer höheren chemischen Stabilität und Sicherheit. Es wird erwartet dass die Festkörperelektrolyte eine erhöhte ionische Leitfähigkeit und zusätzlich mechanische Stabilität besitzen, die eine zuverlässige Trennung der Elektroden sicherstellen, und es voraussichtlich erlaubt Langzeit-zyklischem Betrieb zu widerstehen. Jedoch, im Gegensatz zu den weitreichend untersuchten elektrochemischen Eigenschaften bedürfen die mechanischen Eigenschaften, welche für die Langzeitzuverlässigkeit wichtig sind, noch vertiefter Studien. Daher ist das Hauptziel dieser Arbeit die mechanische Charakterisierung der entsprechenden keramischen Materialien als Kandidaten für Festkörperelektrolyte and den Zusammenhang zu den Material-Mikrostrukturen zu untersuchen. Mit diesem Ziel wurden drei Arten von Festkörperelektrolyten untersucht, NASICON Typ $Li_{1+x}Al_xTi_{2-x}(PO_4)_3$ (LATP), Granat Typ $Li_7La_3Zr_2O_{12}$ (LLZO), Perowskit Typ $Li_{0.350}La_{0.557}TiO_3$ (LLTO), diese wurden ausgewählt aufgrund der vorherig verifizierten vielversprechenden elektrochemischen Eigenschaften.

Mit dem Ziel die mechanischen Eigenschaften des LATP Materials zu verstehen wurden in dieser Arbeit LATPs, gesintert bei unterschiedlichen Temperaturen (950 – 1100 °C), mittels Härteeindrucksprüfung charakterisiert. Die Resultate zeigten dass LATPs gesintert bei höheren Temperaturen einen höheren elastische Modul, Härte und Risszähigkeit besitzen. Die Anisotropie der mechanischen Eigenschaften des bei 1100°C gesinterten Festköperelektrolyt-Materials wurden in dieser Arbeit mittels einer Härteeindrucks-Kartierung in einem tiefen-kontrollierten Modus bei Raumtemperatur untersucht, mit unterstützen der EBSD-Charakterisierung. Die experimentell hergeleiteten elastischen Moduli und Härtewerte zeigten ähnliche Tendenzen, d.h. dass der Rotationswinkel zwischen den zwei prismatischen Ebenen keinen messbaren Effekt hatte, wohingegen im Fall, dass der Rotationswinkel von der basalen Ebene zur prismatischen Ebene erhöht wurde, elastischer Modul und Härtewert sich auffällig verringerten.

Zusätzlich wurde, um die Versagenszuverlässigkeit der Elektrolyte zu beurteilen, $Li_{1.5}Al_{0.5}Ti_{1.5}P_3O_{12}$ gemischt mit SiO_2 (LATP:Si) und ein LLZO Material ausgesucht zur Analyse der makroskopischen mechanischen Eigenschaften, dabei konzentrierend auf Bruchfestigkeit und Weibull Modul. Die Weibull Moduli von LATP:Si und LLZO waren in einem ähnlichen Bereich wie die anderer keramischer Materialien, wohingegen die Bruchfestigkeit von LATP:Si höher war als die von LLZO, welches potentielle Vorteile des LATP:Si Materials impliziert. Aufgrund der Materialverfügbarkeit wurde die Spannung für eine tolerierbare Versagenswahrscheinlichkeit nur für den LLZO Elektrolyt hergeleitet, welches ergab dass zum Beispiel für eine Lebensdauer von 3 Jahren mit garantierter Versagenswahrscheinlichkeit von 1% die Spannung 21 MPa nicht übersteigen sollte.

Da Elektrolyte in Li-Festkörperbatterien unter zyklischen elektronischen Spannungsbedingungen betrieben werden, welches mit chemischen Dehnungseffekten assoziiert ist, wurden exemplarisch für LLTO, einem anwendungsnahen Material, Spannungseffekte auf die mechanischen Eigenschaften studiert. Elastischer Modul, Härte und Bruchzähigkeit von LLTO bei unterschiedlichen elektronischen Spannungen wurden getestet, welches ähnliche Tendenzen offenbarte, d.h. sowohl Leitfähigkeit als auch Risszähigkeit waren proportional zur Gitterkonstante, elastischer Modul und Härte waren umgekehrt proportional zur Gitterkonstante und verhielten sich damit gegensätzlich zu Leitfähigkeit und Risszähigkeit.

Die Untersuchungen des Effekts von Sintertemperatur, Kornausrichtung und Ladungszustand sowohl auf die mechanischen Eigenschaften der Elektrolyte als auch die Versagenszuverlässigkeit tragen zum Verständnis der mechanischen Eigenschaften der Materialien bei und stellen eine Datenbasis zur Verfügung zur weiteren Verbesserung von Design und Prozessierbarkeit von Batteriematerialien und Zellen.

Band / Volume 487
Leistungssteigerung metallgestützter Festelektrolyt-Brennstoffzellen (MSCs) durch gezielte Optimierungen des Anoden/Elektrolytverbunds
C. Bischof (2020), X, 176 pp
ISBN: 978-3-95806-455-3

Band / Volume 488
Aluminiumoxiddispersionsverstärkte Haftvermittlermaterialien in Wärmedämmschichtsystemen
C. Vorkötter (2020), VIII, 99, XXXIII pp
ISBN: 978-3-95806-457-7

Band / Volume 489
The Balmer lines emission of fast hydrogen atoms at the plasma-solid interface in a low density plasma: challenges and applications
S. O. Dickheuer (2020), 117 pp
ISBN: 978-3-95806-458-4

Band / Volume 490
Micromechanical Characterization of Ceramic Solid Electrolytes for Electrochemical Storage Devices
J. F. Nonemacher (2020), xv, 131 pp
ISBN: 978-3-95806-461-4

Band / Volume 491
Nanoscale investigation of high temperature oxidation mechanisms of high-Cr ferritic steels
A. Vayyala (2020), xix, 105 pp
ISBN: 978-3-95806-467-6

Band / Volume 492
Electrolyte development for a SOFC operating at low temperature
J. Zhang (2020), vi, 121 pp
ISBN: 978-3-95806-471-3

Band / Volume 493
Modeling and Simulation of Polymer Electrolyte Fuel Cells
S. Zhang (2020), 4, xii, 214 pp
ISBN: 978-3-95806-472-0

Band / Volume 494
Ab initio perspective on hydrogenated amorphous silicon for thin-film and heterojunction photovoltaics
P. Czaja (2020), 107 pp
ISBN: 978-3-95806-474-4

Band / Volume 495
Measurements of Atmospheric OH and HO_2 Radicals by Laser-Induced Fluorescence on the HALO Aircraft during the OMO-ASIA 2015 Campaign
C. Künstler (2020), 156 pp
ISBN: 978-3-95806-477-5

Band / Volume 496
Tomographic observations of gravity waves with the infrared limb imager GLORIA
I. Krisch (2020), vii, 187 pp
ISBN: 978-3-95806-481-2

Band / Volume 497
Aquisition of temporally and spatially highly resolved data sets of relevant trace substances for model development and model evaluation purposes using a mobile measuring laboratory
D. Klemp, R. Wegener, R. Dubus, U. Javed (2020), 110 pp
ISBN: 978-3-95806-465-2

Band / Volume 498
Charakterisierung des Werkstoffverhaltens während des Kosinterns einer neuartigen, inert gestützten Festoxidbrennstoffzelle
F. Grimm (2020), ix, 168 pp
ISBN: 978-3-95806-482-9

Band / Volume 499
WEGE FÜR DIE ENERGIEWENDE
Kosteneffiziente und klimagerechte Transformationsstrategien für das deutsche Energiesystem bis zum Jahr 2050
M. Robinius et al (2020), VIII, 141 pp
ISBN: 978-3-95806-483-6

Band / Volume 500
Mechanical Behavior of Solid Electrolyte Materials for Lithium-ion Batteries
G. Yan (2020), x, 139 pp
ISBN: 978-3-95806-484-3

Weitere ***Schriften des Verlags im Forschungszentrum Jülich*** unter
http://wwwzb1.fz-juelich.de/verlagextern1/index.asp

Energie & Umwelt / Energy & Environment
Band / Volume 500
ISBN 978-3-95806-484-3

Mitglied der Helmholtz-Gemeinschaft

JÜLICH
Forschungszentrum